



**One-dimensional III-nitrides: Towards ultrahigh efficiency,
ultrahigh stable artificial photosynthesis**

Journal:	<i>Journal of Materials Chemistry A</i>
Manuscript ID	TA-REV-12-2022-009967.R1
Article Type:	Review Article
Date Submitted by the Author:	04-Feb-2023
Complete List of Authors:	Dong, Wan Jae; University of Michigan Mi, Zetian; University of Michigan

One-dimensional III-nitrides: Towards ultrahigh efficiency, ultrahigh stability artificial photosynthesis

Wan Jae Dong* and Zetian Mi*

Department of Electrical Engineering and Computer Science, University of Michigan, Ann Arbor, 1301 Beal Avenue, Ann Arbor, MI 48109, USA.

*Corresponding author. E-mail: wanjaed@umich.edu, ztmi@umich.edu

Abstract

The depletion of carbon-based fuels and emerging environmental problems are driving the demand for green energy sources more than ever. Artificial photosynthesis demonstrated by catalytically active semiconductors can convert solar energy into storable energy sources such as hydrogen and carbon products by water splitting and carbon dioxide reduction reaction, respectively. Semiconductors with one-dimensional (1D) nanostructures have gained tremendous attention due to their large surface area and enhanced light absorption. However, the semiconductor nanostructures suffer from degradation caused by oxidation, corrosion, and undesirable change in morphology during the reaction in aqueous electrolytes. In this review, 1D nanostructure III-nitrides are introduced to offer a comprehensive overview of their synthesis methods, unique structural, electronic, optical, surface, and catalytic properties, as well as the efficiency, and stability for artificial photosynthesis. Band gap engineering and tandem stacking of 1D III-nitrides for broadband light absorption are highlighted. Then, recent findings on inherent catalytic activity and stability of 1D III-nitrides are presented. Furthermore, this paper summarizes the cocatalysts integrated on 1D III-nitrides to overcome the performance bottlenecks of water splitting and CO₂ reduction reactions. Finally, the challenges of 1D III-nitrides for practical application of photo(electro)chemical reactions and the prospective insights for future development are provided.

1. Introduction

A massive amount of energy is consumed to maintain daily human life and most of the energy depends on fossil fuels such as petroleum, coal, and natural gas. However, the depletion of fossil fuels thrives the cost of energy and emerging environmental issues, which are driving the demand for green energy technology. In this regard, hydrogen (H_2) fuel has attracted great attention as an alternative future energy source because high-purity H_2 gas can be produced from the earth-abundant water resource with zero greenhouse gas emissions.^{1, 2} Along with alternative H_2 fuels, carbon dioxide (CO_2) recycling, on the one hand, is being extensively studied as a future energy technology.^{3, 4} CO_2 , the main cause of global warming, can be converted into value-added chemicals through catalytic reactions. Inspired by photosynthesis, which transforms CO_2 and H_2O into hydrocarbons using solar energy in the natural carbon cycle, artificial photosynthetic devices have been developed to convert solar energy to H_2 fuel or carbon-based chemicals using CO_2 and H_2O .^{5, 6, 7, 8, 9} Up to now, efficient photosynthetic devices for H_2 production and CO_2 recycling have been demonstrated by the integration of semiconductors and cocatalysts. In this configuration, semiconductor materials absorb the light and excite photogenerated electrons and holes into conduction and valance bands, respectively. The photogenerated charge carriers then separate and migrate to the cocatalyst surface to participate in redox reactions. Therefore, artificial photosynthetic devices must overcome the technical challenges of limited light absorption, inefficient charge separation/transfer, and low catalytic activity before they can be put into practical use.

Over the past decades, the rapid development of nanotechnology has enabled the fabrication of nanostructured semiconductors in 1-dimensional (1D) morphology, including nanowire, nanorod, and nanofiber.¹⁰ These 1D semiconductors have shown distinct physical and chemical characteristics different from their planar counterparts. The large surface-to-volume ratio of 1D nanostructures promotes surface chemical reactions by providing many catalytic active sites.¹¹ New crystal orientations, which are difficult to obtain in planar structures, have been exposed to the surface and boosted the catalytic reactions.¹² The nanostructures have enhanced light absorption by suppressing the Fresnel reflection and by scattering the incident light.^{13, 14} In addition, charge carrier separation and transfer have become much easier since the diffusion lengths of charge carriers have been shortened from the microscale to the nanoscale.¹⁵ These advantages of 1D semiconductors have demonstrated much enhanced photoelectrochemical and photocatalytic performance compared to the planar structures.^{16, 17, 18} However, there are

still many remaining challenges such as inefficient light absorption, poor stability, and sluggish kinetics of surface chemical reactions. To mitigate these problems, 1D III-nitrides (*i.e.*, GaN, InN, and their alloys) have emerged as the next-generation artificial photosynthetic semiconductors.

III-nitrides have been designed and tailored for application in each particular photo(electro)chemical system. Ternary alloying (InGaN) of III-nitrides could allow fine-tuning of the band gap and lattice parameter to access ideal band edge positions and to realize epitaxial growth of high-quality crystals. The energy band gap of III-nitrides can be controlled across nearly the entire solar spectrum while straddling a broad range of redox potentials (Fig. 1a).^{19,20,21} Hence, charge carrier transport at the III-nitride/electrolyte interface is energetically feasible for water splitting and CO₂ reduction reactions. III-nitrides typically have a wurtzite crystal structure with a polar c-plane. Since the polarity of III-nitrides leads to the preferential growth of planar film along the c-axis, the catalytic activity of the polar c-plane has been commonly studied for artificial photosynthesis. However, 1D III-nitrides, having a small portion of the polar top surface and abundant nonpolar side surfaces, have enabled crystal facet engineering to improve the performance of photoelectrodes and photocatalysts. Each crystal orientation of III-nitrides has different surface electronic structure, surface potential, and catalytic activity. Thus, various optoelectronic and catalytic characteristics can be demonstrated by fabricating III-nitrides nanostructures. Moreover, surface band bending and electrical conductivity of 1D III-nitrides can be manipulated by n- or p-type doping for each particular artificial photosynthetic application.¹⁹ Optimized surface band bending has promoted the charge carrier separation in the semiconductors, which can suppress charge carrier recombination. Interestingly, their surfaces can be terminated with nitrogen atoms, or nitrogen-rich nanoclusters, to protect against photo-corrosion and oxidation, resulting in unprecedented long-term stability (Fig. 1b).²² Hence, 1D III-nitrides hold grand promise in promoting H₂ production by solar water splitting and CO₂ upgrading by solar-driven CO₂ reduction reaction.

In this review, the fabrication methods of 1D III-nitride nanostructures are first presented. Then, the recent progress in band engineering, doping, and heterostructure of 1D III-nitride semiconductors for artificial photosynthetic applications is described. The material design strategies for enhancing the catalytic reactions are classified into four parts of photoelectrochemical water splitting, photocatalytic water splitting, photoelectrochemical CO₂ reduction, and photocatalytic CO₂ conversion. In the end, the critical challenges and prospects

of 1D III-nitride materials for realizing practical artificial photosynthesis are discussed.

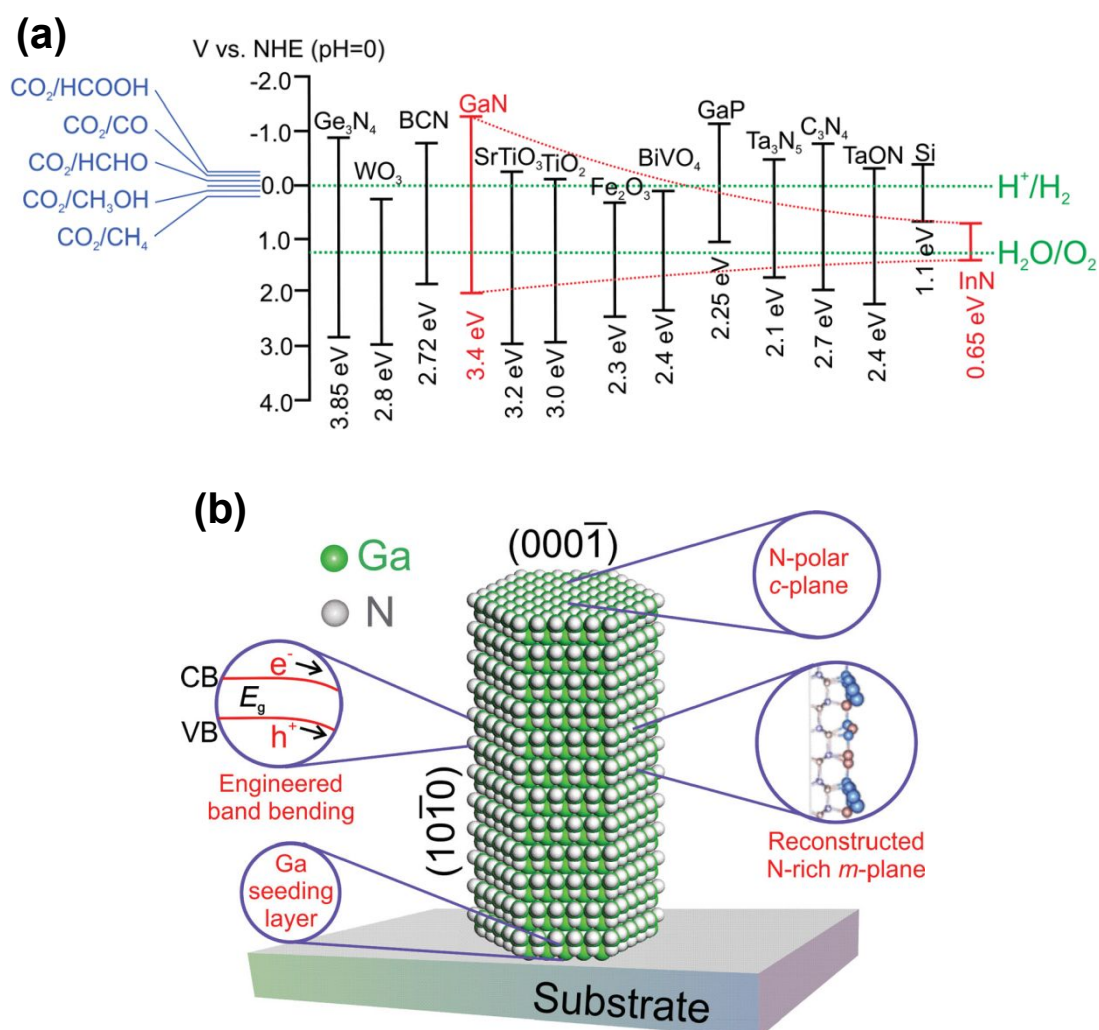


Fig. 1. (a) Schematic of the tunable $\text{In}_x\text{Ga}_{1-x}\text{N}$ band structure compared to other semiconductors, including the redox potentials of water splitting and CO_2 reduction. Reproduced with permission from Ref. 19. Copyright (2016) Royal Society of Chemistry. (b) Schematic of the atomic and electronic structure of the nitrogen-terminated GaN nanowire. Reproduced with permission from Ref. 22. Copyright (2016) John Wiley and Sons.

2. Fabrication of 1-dimensional III-nitrides

1-dimensional III-nitride nanostructures have been fabricated by bottom-up growth or top-down etching methods (Fig. 2). In more detail, the growth strategies of 1D III-nitrides can be classified into catalyst-assisted or catalyst-free growth. The top-down methods also can be

divided into dry or wet etching processes. In addition, a chemical synthetic method has demonstrated the growth of GaN nanowires using a solution-based synthesis of gallium oxide nanowires followed by nitridation under the NH_3 atmosphere.^{23, 24, 25, 26} However, GaN nanowires in powder form, obtained by chemical synthesis, have many crystal defects and charge carrier trapping sites within the band gap, so there is a limit to their application to photoelectrodes. Thus, in the following sections, bottom-up growth and top-down methods for the fabrication of high crystal quality 1D III-nitrides are mainly described.

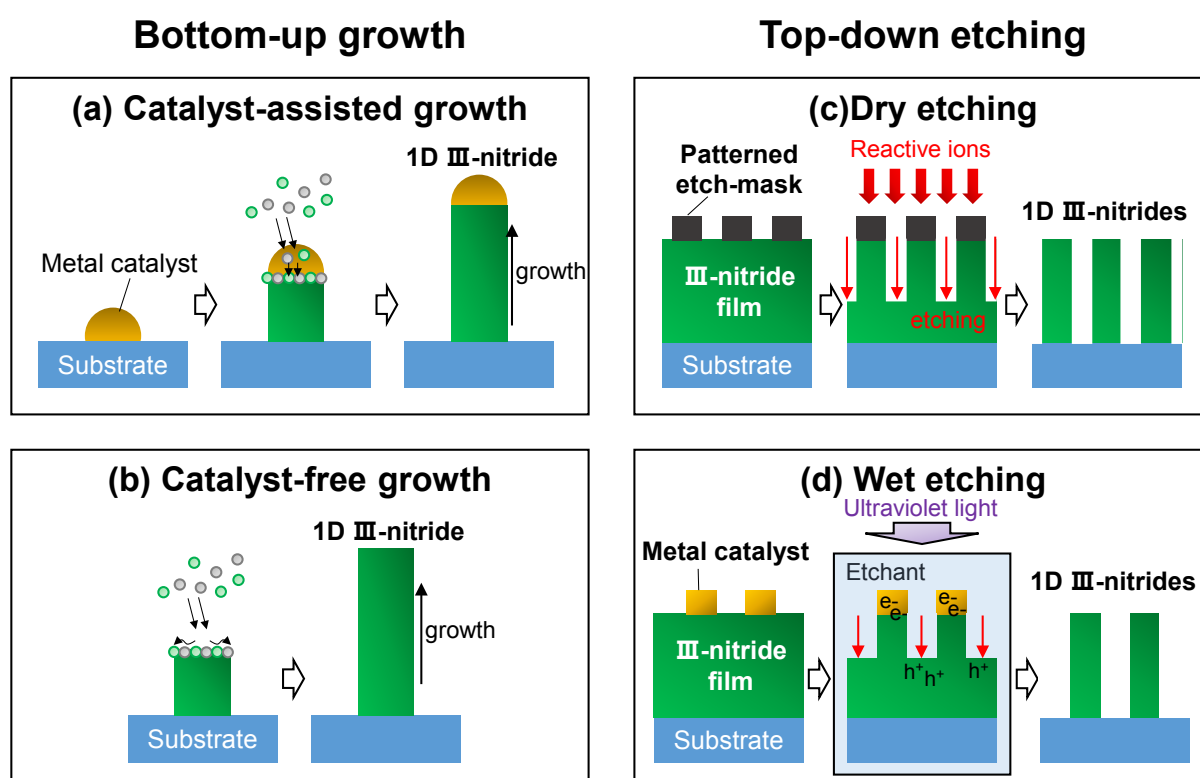


Fig. 2. Schematic illustrations of representative 1D III-nitride fabrication methods. Bottom-up growth can be classified into (a) catalyst-assisted growth and (b) catalyst-free growth. Top-down etching methods can be classified into (c) dry etching and (d) wet etching.

2.1. Bottom-up growth

To date, most of the high-performing 1D III-nitride nanostructure photoelectrodes or photocatalysts have been fabricated based on the bottom-up method because this process offers high crystal quality with less defects. Moreover, tuning of morphology, incorporation of dopants, and constructing heterogeneous structures can be realized by varying the growth

parameters including the temperature, ratio of source materials, growth duration, etc. Previously, a vapor-liquid-solid growth mechanism was proposed for growing the Si whiskers with Au catalysts.²⁷ At high temperature, sufficiently enough to form Si:Au liquid droplets, the Si vapor preferentially incorporates into liquid metal catalysts and nucleates at the interface between Si crystals and liquid droplets, thereby resulting in high-quality Si crystal growth along the axial direction. Eventually, the Au catalyst droplets remain at the top of Si whiskers. Because the liquid metal catalysts are preferential sites for the incorporation of vapor phase Si, the morphology and composition of Si whiskers are determined, to a large extent, by the metal catalyst. This metal catalyst-assisted vapor-liquid-solid growth technique has been extended to the growth of 1D III-nitride semiconductors (Fig. 2a). III-nitrides nanowires, grown by the metal-organic chemical vapor deposition (MOCVD) method, have been successfully fabricated with various catalysts such as Au,^{28, 29, 30} Ni,^{31, 32, 33} AuNi alloy,^{34, 35} Fe,³⁶ and Cu³⁷ on different substrates, including sapphire, silicon, GaAs, and GaP.³⁸ Although the foreign metal catalysts promote the growth of 1D nanostructures, the stacking faults and deep trapping states are unavoidable due to the difference in the crystal structure between the metals and III-nitrides. The defect states in photoelectrodes can degrade the photoelectrochemical performance by behaving as charge-trapping centers. In this regard, catalyst-free III-nitride nanowires have been extensively developed (Fig. 2b).^{38, 39, 40} Molecular beam epitaxy (MBE) method under nitrogen-rich conditions can result in III-nitride nanowires through a diffusion-driven mechanism without any metal catalyst.^{41, 42, 43, 44} During the growth, the supplied adatoms migrate along the lateral nonpolar planes of the nanowire and then primarily settle down on the top polar planes due to the lower chemical potential on the top surface, which consequently promotes the axial growth of nanowires.⁴⁵ The distinct feature, that the diameter of the nanowires is inversely proportional to their length, indicates that there is competition between lateral expansion or vertical elongation of the nanowires on surfaces with different polarities.^{46, 47} Furthermore, it was found that the growth of nanowires proceeds through two steps of two-dimensional nuclei formation and transformation into nanowires.⁴⁸ This growth model suggests that III-nitride nanowires essentially do not have an epitaxial relationship with the underlying substrates and can be grown on any type of substrate.^{49, 50, 51} In addition to the advantage of catalyst-free growth on arbitrary substrates, the MBE method of 1D III-nitride enables in-situ growth of heterostructure, effective n- or p-type doping, and tunable band gap energy. Therefore, 1D III-nitride semiconductors with appropriate band structure and surface atomic

arrangement can be prepared for the target catalytic reactions, including water splitting and CO₂ reduction reactions.

2.2. Top-down etching

Anisotropic etching of planar III-nitride film has demonstrated fabrication of 1D nanostructures. Among the top-down etching methods, dry etching (*i.e.*, reactive ion etching) of patterned GaN epilayers have been employed to fabricate the photoelectrodes for solar water splitting (Fig. 2c).^{52, 53, 54} The diameter, height, and aspect ratio of 1D nanostructures can be facilely controlled by tuning the pattern size and changing the reactive ion etching conditions. Because the etched 1D nanostructures have been patterned on high-quality III-nitride epilayers grown using mature planar film growth technology, the material properties such as doping concentration, band gap, and multi-band structure can be precisely manipulated.⁵⁵ However, the patterning of the etch-masks (*i.e.*, photolithography, nanosphere lithography, nanoparticle coating, etc.) must be performed before the dry etching process,^{56, 57} making fabrication difficult, complex, and costly. Moreover, the physical bombardment of highly reactive ions to III-nitride epilayers inevitably results in surface defects, which act as recombination sites for photogenerated charge carriers and degrade the photoelectrochemical performance. These defects tend to be recovered, to some extent, by thermal annealing at high temperatures for a long treatment time, but this process also is an obstacle to the formation of heterojunction using semiconductor or catalyst materials that cannot withstand high temperatures. The limitations of top-down etching are also evidenced by the severe efficiency cliff of micro-light-emitting diodes.^{21, 58}

Anisotropic wet etching methods can fabricate III-nitride nanostructures. For instance, metal-assisted chemical etching, which has been studied in the fabrication of vertically aligned Si nanowires, can apply to fabricate III-nitride nanostructures (Fig. 2d). Under light illumination, photogenerated electrons migrate to the pre-patterned metal catalyst, whereas photogenerated holes remain on the GaN surface.⁵⁹ Then, the photogenerated holes oxidize the exposed GaN epilayers, and the etchant rapidly removes the oxidized GaN, thereby resulting in nanowire morphology. Choosing different metal catalysts on GaN films can switch the cathodic and anodic reaction sites and accordingly change the surface morphology.⁶⁰ Electrochemical wet etching can also fabricate nanoporous III-nitride photoelectrodes based on a combination of an oxidation process and a dissolution process in an acidic etchant under

an anodic potential.^{61, 62, 63} However, it is very difficult to control the morphology of nanostructures by the wet-etching process. The repeated oxidation and dissolution of III-nitride materials causes uncontrollable crystal facets and unavoidable amorphous oxide formation, which inhibit catalytic reactions. More importantly, the nanostructures can only be fabricated at a specific condition. For example, electrochemical etching cannot operate on intrinsic or p-type GaN layers, limiting the application of artificial photosynthetic devices.

3. Photoelectrochemical water splitting

Photoelectrochemical water splitting can be classified into two half-reactions of H₂ evolution and O₂ evolution at photocathode and photoanode, respectively. Photoelectrochemical H₂ evolution reaction is driven by photogenerated electrons in semiconductors under applied cathodic potential. The light having energy larger than the band gap of semiconductors excites photogenerated electrons in the conduction band leaving photogenerated holes in the valance band. Then, photogenerated electrons in the conduction band migrate toward the surface (electrode/electrolyte interface) for the H₂ evolution reaction. Therefore, the conduction band edge position of the photocathode should be located above the reduction potential of water for the efficient H₂ evolution reaction. On the other hand, the photoelectrochemical O₂ evolution reaction occurs when the photogenerated holes in the valance band of semiconductors participate in the water oxidation reaction with help of anodic potential. Hence, the valance band edge position of the photoanode should be positioned below the oxidation potential of water. Because III-nitride materials such as GaN or InGaN can satisfy both requirements of conduction and valance band edge positions for water reduction and oxidization, respectively, their photoelectrochemical water splitting properties have been extensively studied. Especially, GaN and InGaN nanostructures (*i.e.*, nanorods,^{64, 65, 66} nanowires,^{67, 68, 69, 70, 71, 72, 73, 74, 75, 76} nanowalls⁷⁷) have attracted great attention because they outperform the planar structures in photoelectrochemical water splitting activity (Table 1 and 2). Thus, the recent strategies to enhance the photocurrent density and to reduce the overpotential of 1D nanostructured III-nitrides photoelectrode will be reviewed in the following sections.

Table 1. Recent III-nitrides photoanodes for photoelectrochemical water splitting

Photoanode	Cocatalyst	Potential	Electrolyte	Light intensity	Current density	Ref.
GaN nanorods/V-groove textured Si	-	1.14 V _{RHE}	0.5 M NaOH	100 mW/cm ² AM 1.5 S	801.62 μA/cm ²	66
InGaN NWs	Ir NPs	0.61 V _{RHE}	0.1 M PBS (pH~7)	500 mW/cm ² AM 1.5G	~2 mA/cm ²	67
GaN NWs	Au NPs	-0.4 V _{RHE}	1 M NaOH	100 mW/cm ²	~1 mA/cm ²	68
GaN NWs	-	0.6 V _{RHE}	0.5 M H ₂ SO ₄	100 mW/cm ²	2.2 mA/cm ²	72
ZnS/GaN NWs	Au NPs	0 V _{RHE}	1 M NaOH	100 mW/cm ²	1.15 mA/cm ²	73
InGaN NWs on oblique pyramid-textured Si	NiOOH	1.0 V _{RHE}	0.5 M Na ₂ SO ₄	100 mW/cm ²	~0.4 mA/cm ²	76
Si-doped InGaN NWs	-	1.597 V _{NHE}	0.1 M PBS (pH = 7)	N/A	1.42 mA/cm ²	78
Zn-doped InGaN nanorods	Au	1.23 V _{RHE}	0.5 M H ₂ SO ₄	100 mW/cm ²	1.65 mA/cm ²	79
InGaN NWs	IrO ₂	0.6 V _{RHE}	0.5 M H ₂ SO ₄	100 mW/cm ²	5.2 mA/cm ²	80
InGaN/GaN nanorods	-	1.35 V _{RHE}	0.01 M H ₂ SO ₄	100 mW/cm ² AM 1.5	0.3 mA/cm ²	81
InGaN/GaN NWs	-	1.0 V _{Ag/AgCl}	1 M HBr	100 mW/cm ² AM 1.5	~23 mA/cm ²	82
ZnS/GaN	-	0 V vs. Pt	1 M NaOH	500 mW/cm ²	2.8 mA/cm ²	83
C ₃ N ₄ /InGaN nanorods	-	1.23 V _{RHE}	0.5 M H ₂ SO ₄	100 mW/cm ²	13.9 mA/cm ²	84
W _x S _{1-x} /GaN NWs	-	0.6 V _{RHE}	0.5 M H ₂ SO ₄	100 mW/cm ²	20.38 mA/cm ²	85
InGaN nanorods/Mxene	-	1.23 V _{RHE}	0.5 M H ₂ SO ₄	100 mW/cm ²	7.27 mA/cm ²	86
n-InGaN/n ⁺ -GaN NWs/n ⁺ -p ⁺ -n Si	-	~0.6 V _{NHE}	1 M HBr	100 mW/cm ²	16.3 mA/cm ²	87

Table 2. Recent III-nitrides photocathodes for photoelectrochemical water splitting

Photocathode	Cocatalyst	Potential	Electrolyte	Light intensity	Current density	Ref.
p-GaN hexagonal microwell	2D-MoS ₂	0 V _{RHE}	0.5 M H ₂ SO ₄	100 mW/cm ²	2.15 mA/cm ²	88
n ⁺ -GaN NWs/n ⁺ -p Si	MoS ₂	0 V _{RHE}	0.5 M H ₂ SO ₄	100 mW/cm ²	~40 mA/cm ²	89
p-InGaN/TJ/n-GaN NWs/n ⁺ -p Si	Pt	0.26 V _{NHE}	1 M HBr	130 mW/cm ²	40.6 mA/cm ²	90
p-InGaN/TJ/n-InGaN NWs/n-Si	Pt	0 V vs. Pt	0.5 M H ₂ SO ₄	100 mW/cm ²	2.8 mA/cm ²	91
p-InGaN/TJ/n-GaN NWs/n-Si	Pt	0 V _{RHE}	0.5 M H ₂ SO ₄	100 mW/cm ² AM 1.5 G	12.3 mA/cm ²	92
p-InGaN/TJ/n-InGaN NWs/n ⁺ -p Si	Pt	0.4 V _{RHE}	0.5 M H ₂ SO ₄	100 mW/cm ² AM 1.5 G	~9 mA/cm ²	93
p-InGaN/TJ/n-InGaN NWs/n ⁺ -p Si	Pt	0 V vs. IrO _x	0.5 M H ₂ SO ₄	100 mW/cm ² AM 1.5 G	~8.4 mA/cm ²	94
GaN quasi-film/n ⁺ -p Si	Pt	0 V _{RHE}	0.5 M H ₂ SO ₄	100 mW/cm ² AM 1.5 G	~25 mA/cm ²	95
patterned GaN quasi-film/n ⁺ -p Si	Pt	0 V _{RHE}	0.5 M H ₂ SO ₄	100 mW/cm ² AM 1.5 G	~18 mA/cm ²	96
n ⁺ -GaN NWs/n ⁺ -p Si	Pt	0 V _{RHE}	0.5 M H ₂ SO ₄	100 mW/cm ² AM 1.5 G	~38 mA/cm ²	97
GaN nanostructure /GaInP ₂ /GaAs/Ge triple-junction	Pt	~1.2 V _{RHE}	0.1 M H ₂ SO ₄	100 mW/cm ² AM 1.5 G	~10.3 mA/cm ²	98
n ⁺ -GaN NWs/n ⁺ -p Si	Pt	-0.6 V _{RHE}	Seawater	900 mW/cm ² AM 1.5 G	~163 mA/cm ²	99

3.1. Doping and band engineering of 1D III-nitrides

Doping or alloying of III-nitrides can result in broadband light absorption, increased charge carrier concentration, and surface band bending. All these optoelectronic properties are closely related to the photoelectrochemical water splitting performance.¹⁰⁰ Previously, the influence of Si doping on the photoelectrochemical performance of n-type InGaN nanowires photoanodes has been investigated.⁷⁸ The Si dopant concentration was tuned by changing the Si effusion cell temperature (T_{Si}) during the MBE growth of vertically aligned InGaN nanowires on Si

substrate (Fig. 3a). Si-doped InGaN nanowires photoanode showed the maximum dopant concentration of $2.1 \times 10^{18} \text{ cm}^{-3}$ at $T_{\text{Si}} = 1120 \text{ }^\circ\text{C}$ (Fig. 3b). At this optimized n-type doping concentration, conduction band edge and valance band edge still straddle the water redox potentials, thereby leading to ~ 9 times higher photocurrent density compared to the undoped InGaN nanowires (Fig. 3c). More recently, Zn atom is employed as a dopant to control the electronic structure and to modify the crystal structure of InGaN nanowires.⁷⁹ The amount of Zn dopant was changed by Zn cell temperature during the MBE growth of InGaN nanowires. Zn doping shifted the valance band edge more positively compared to the undoped InGaN nanowires, which can lead to enhanced water oxidation kinetics (Fig. 3d). In addition, Zn doping reduced In composition and prevented the formation of deep energy levels originating from the In aggregation (Fig. 3e). The improved energy band structure and crystal quality of Zn-doped InGaN photoanode greatly improved the photocurrent density by ~ 3 times (Fig. 3f). The improved photoelectrochemical performance demonstrated by doping of transition metal opens greater possibilities for realization of III-nitrides as efficient water splitting photoelectrodes.

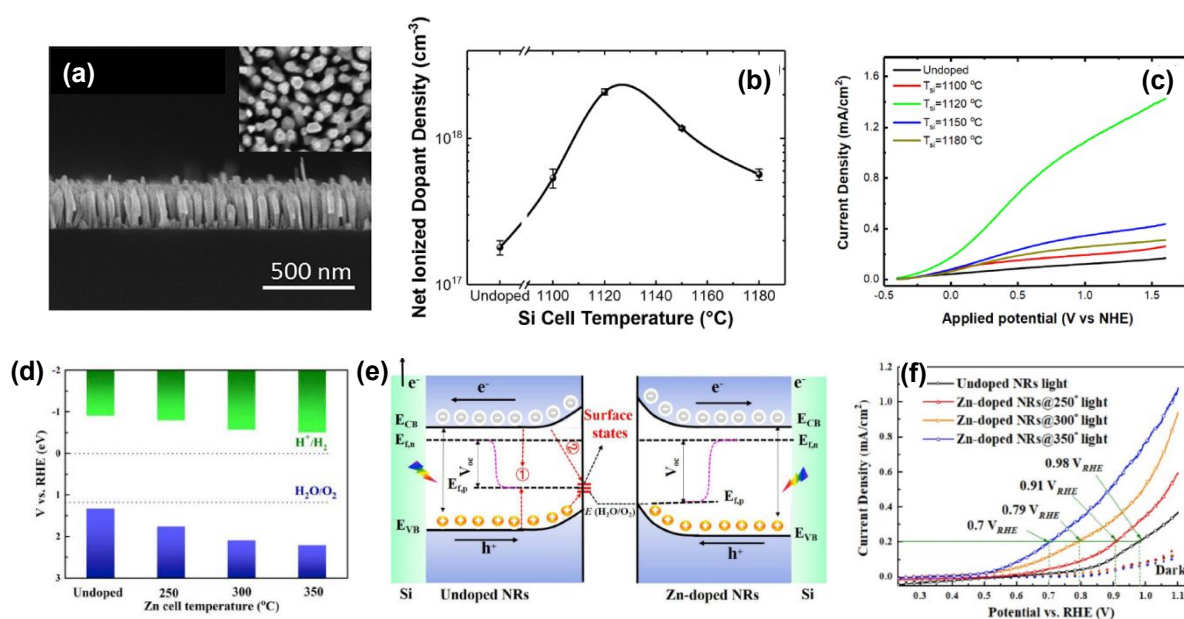


Fig. 3. (a) Cross-sectional view of the InGaN nanowire photoanode. (b) Net ionized dopant density of Si-doped InGaN nanowires with respect to Si cell temperature. (c) Linear sweep voltammetry (LSV) curves of Si-doped InGaN nanowire photoanodes. Reproduced from Ref. 78. Copyright (2018) AIP Publishing. (d) Valance band and conduction band potentials of Zn-

doped InGaN nanowires with respect to Zn cell temperature. (e) Band-bending diagram and charge carrier transport schematic of photoelectrochemical water oxidation for undoped and Zn-doped InGaN photoanodes. (f) LSV curves of Zn-doped InGaN nanowire photoanodes. Reproduced from Ref. 79. Copyright (2020) Elsevier.

Alloying of In element to GaN semiconductor can increase the charge carrier mobility and reduce the band gap energy to demonstrate broadband light absorption, thereby leading to an increase in photocurrent density for photoelectrochemical water splitting reaction.^{101, 102} Previously, In-rich InGaN nanowire photoanode having a small band gap of 1.7 eV was grown on n-type Si substrate by MBE method.⁸⁰ InGaN nanowires were vertically aligned on Si substrate with an approximate diameter of ~ 200 nm and height of ~ 700 nm (Fig. 4a). To enhance the O₂ evolution reaction, IrO₂ nanoparticle cocatalysts were loaded on InGaN nanowires by photodeposition process. Photoelectrochemical water oxidation performance of the InGaN nanowire photoanode was evaluated in an acidic electrolyte (0.5 M H₂SO₄) under air mass 1.5 global (AM 1.5G) simulated 1 sun light in a three-electrode configuration (Fig. 4b). The pristine InGaN nanowires showed a low photocurrent density and a large overpotential due to poor kinetics of water oxidation reaction (Fig. 4c). However, after the modification of InGaN with IrO₂ cocatalysts, the activity of the photoelectrode greatly improved. Due to the unique 1D nanowire structure, low energy band gap of 1.7 eV, and appropriate band edge positions to straddle the redox potentials of water splitting, together with effective coupling with IrO_x cocatalysts, the InGaN nanowires resulted in a low onset potential of 0.1 V_{RHE}, a high photocurrent density of 5.2 mA/cm² at 0.6 V_{RHE}, and a half-cell solar energy conversion efficiency up to 3.6%.

In addition to the reduced band gap of InGaN nanowires, dual-band GaN/InGaN core/shell nanowires have been developed as visible-light responsive photoelectrodes.^{103, 104, 105, 106} For instance, GaN/InGaN core/shell nanowire arrays were fabricated by sequential growth of n-type GaN nanorods followed by n-type InGaN coating using MOCVD method (Fig. 4d).⁸¹ It is observed that GaN nanowires, having an average diameter of 900 nm and height of 14 μ m, are covered by 20 nm-thick InGaN layer (Fig. 4e). Compared to GaN nanowires, GaN/InGaN nanowires photoanode showed 10-fold higher photocurrent density at the anodic potential of 1.35 V_{RHE} (Fig. 4f). The photocurrent density enhancement was mainly attributed to the

extended light absorption of the narrow band gap InGaN shells, which can utilize visible light and increase the number of photogenerated charge carriers. The InGaN segments can also be incorporated into 1D GaN nanowires along the axial direction by MBE growth (Fig. 4g).⁸² High angle annular dark field (HAADF) image of InGaN/GaN nanowires illustrated the atomic number contrast between GaN (darker) and InGaN (brighter) regions and the presence of 3 segments of ~70 nm long InGaN passivated by GaN layer (Fig. 4h). This dual-band photoanode was first tested with the use of 375 nm long-pass filter, which prevents the excitation of the GaN region. The photoanode revealed a photocurrent density of ~11 mA/cm² at 1 V_{Ag/AgCl}, indicating the excitation of charge carriers by InGaN segments under visible light. Notably, when AM 1.5G filter was used, the photocurrent density was greatly enhanced to ~23 mA/cm² at 1 V_{Ag/AgCl} because of concurrent excitation of charge carriers in both InGaN and GaN regions. From these results, it was found that the strategy of integrating ultraviolet-light-absorbing GaN and visible-light-responsive InGaN into 1D nanostructures can create a synergistic effect on photoelectrochemical water splitting.

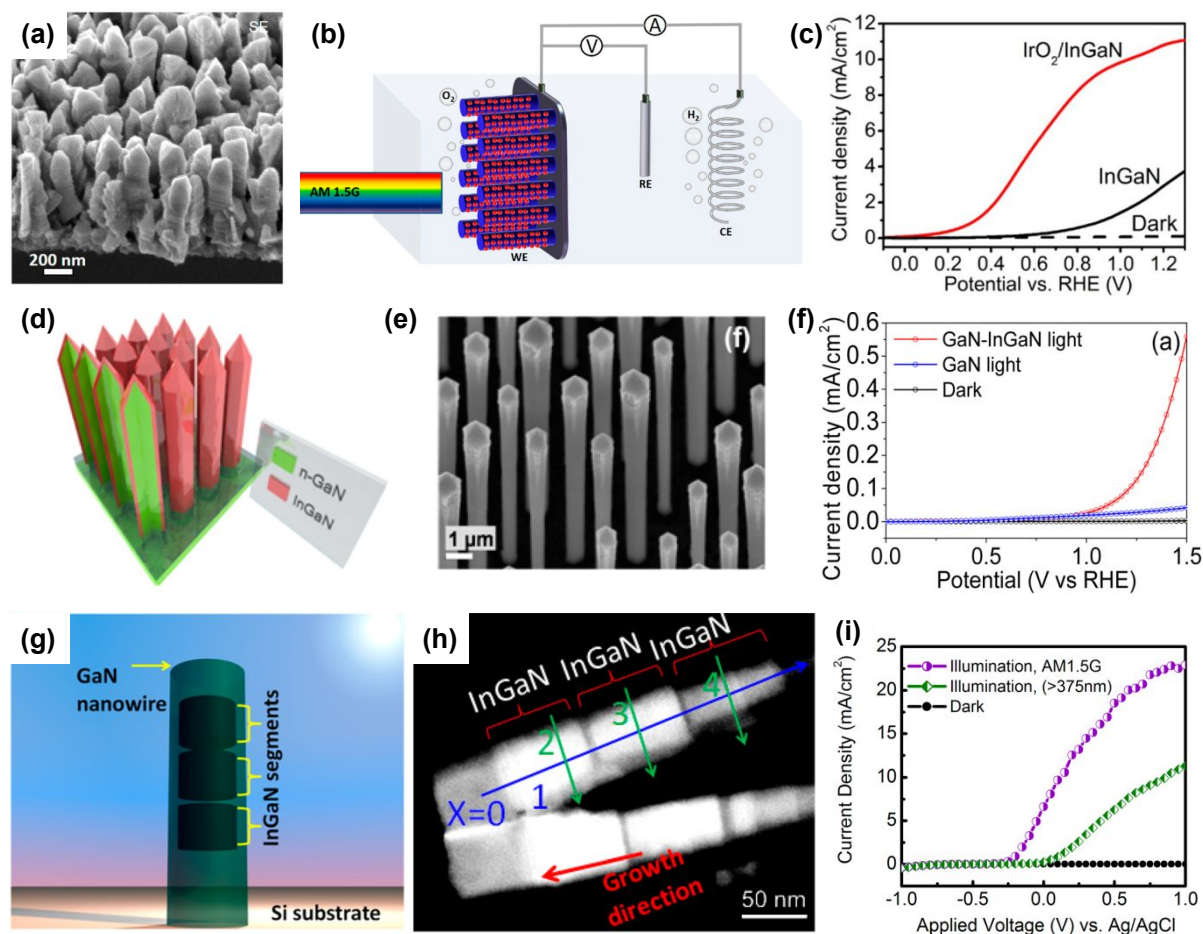


Fig. 4. (a) Scanning electron microscopy (SEM) image of the InGaN nanowire. (b) Schematic illustration of the three-electrode cell for photoelectrochemical water oxidation. InGaN nanowire photoanode, Pt wire, and Ag/AgCl were used as the working, counter, and reference electrodes, respectively. (c) LSV curves of InGaN and IrO_x/InGaN photoanodes in 0.5 M H₂SO₄ under light illumination. Reproduced from Ref. 80. Copyright (2018) American Chemical Society. (d) Schematic illustration and (e) SEM image of GaN/InGaN core/shell nanorod arrays. (f) Current density vs. potential plots of GaN/InGaN core/shell nanorods photoanode and GaN nanorods in 0.01 M H₂SO₄ solution under 1 sun illumination using AM 1.5G filter. Reproduced from Ref. 81. Copyright (2014) American Chemical Society. (g) Schematic illustration and (h) transmission electron microscopy (TEM) image of GaN nanowires with axially incorporated InGaN segments. (i) Anodic photocurrent density measured in 1 M HBr under simulated sunlight illumination with filters. Reproduced with permission from Ref. 82. Copyright (2013) American Chemical Society.

3.2. Heterostructure

Design of heterostructure by the combination of two or more semiconductor materials is a promising strategy for broadband light absorption, suppression of electron-hole recombination, and increased lifetime of photogenerated charge carriers. When two semiconductors with different work functions are in contact, the built-in electric field at the heterojunction interface can promote charge separation and increase the current density for photoelectrochemical water splitting. Thus, GaN and InGaN nanostructures combined with other semiconductors (ZnS,⁸³ MoS₂,⁸⁸ C₃N₄,⁸⁴ W_xS_{1-x},⁸⁵ MXene⁸⁶) have been exploited in photoelectrochemical water splitting. For example, photoanodes, consisting of GaN nanowires coated with tungsten sulfide (W_xS_{1-x}), were fabricated by MBE growth of GaN and solvothermal synthesis of W_xS_{1-x} (Fig. 5a).⁸⁵ The vertically grown GaN nanowires on Si wafer had an average length of ~443 nm and an average diameter of ~35 nm (Fig. 5b). The average thicknesses of the W_xS_{1-x} layer could be varied from 0.79 to 3.23 nm depending on the synthetic conditions (Fig. 5c). The photoelectrochemical water oxidation performance was measured in 0.5 M H₂SO₄ under 1 sun solar light. GaN-W_xS_{1-x} photoanode showed superior performance compared to the GaN without W_xS_{1-x}. The photocurrent density was as high as 20.38 mA/cm² at 0.6 V_{RHE} and the maximum applied-bias photon-to-current efficiency (ABPE) of 13.76% was achieved (Fig. 5d). This greatly improved performance attributed to the type-II band structure formed at GaN/W_xS_{1-x} interface (Fig. 5e). In this photoanode configuration, the photogenerated holes efficiently transfer to the valence band of W_xS_{1-x} for water oxidation reaction while the photogenerated electrons migrate to the conduction band of GaN nanowires, thereby leading to accelerated charge carrier separation and suppression of charge carrier recombination. In comparison to the deposition of semiconductors on 1D nitrides, a direct growth of InGaN nanowires on MXene can also construct a heterostructure for photoelectrochemical water splitting.⁸⁶ The MXene (Ti₃C₂T_x) film with a thickness of ~50 nm was spin-coated on an n-type Si substrate. Then, InGaN nanorods were vertically grown on it by MBE (Fig. 5f). MXene/InGaN nanorods photoanode revealed a very low onset potential and high photocurrent density of 7.27 mA/cm² at 1.23 V_{RHE}, which is over 10 times higher than InGaN/Si photoanode (0.71 mA/cm²) (Fig. 5g). The low onset potential and high photocurrent density are originated from the type-II band alignment at the InGaN/MXene interface where the photogenerated carrier can be efficiently separated, with electrons transfer from InGaN to MXene and holes transfer from MXene to InGaN for water oxidation (Fig. 5h). Overall, type-II heterostructures

at the III-nitrides and other semiconductor interfaces were found to enhance the photoelectrochemical water splitting performances by promoting the separation of photogenerated charge carriers.

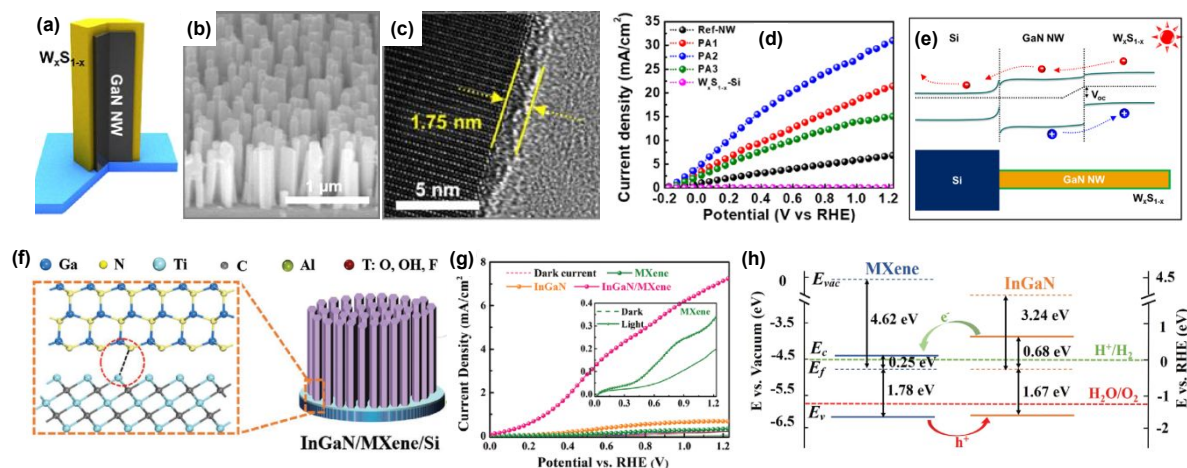


Fig. 5. (a) Schematic illustration, (b) SEM image, and (c) high-resolution TEM image of GaN nanowires covered with W_xS_{1-x} layer. (d) Current density-potential curves of the GaN nanowires and GaN nanowires- W_xS_{1-x} photoanodes in 0.5 M H_2SO_4 . (e) Energy band diagram of photoanode under light illumination. Reproduced with permission from Ref. 85. Copyright (2020) American Chemical Society. (f) Schematic illustration of InGaN/MXene nanorods. (g) LSV curves of InGaN, Mxene, and InGaN/Mxene photoanodes. (h) Proposed band diagram of InGaN/MXene heterojunction. Reproduced with permission from Ref. 86. Copyright (2020) John Wiley and Sons.

3.3. Tunnel Junction

Tunnel junction diodes, that connect the top cell with a large band gap and the bottom cell with a small band gap, have been extensively studied to address the current matching issues for dual or triple absorber solar cells and photoelectrodes in III-V systems.^{107, 108, 109, 110} Inspired by this strategy, there have developed III-nitride nanowire top cells grown on Si bottom cells for both photoanode and photocathode applications.^{90, 91, 92, 111} Recent theoretical study on InGaN/Si double-junction photocathodes indicated that the high photocurrent density up to ~ 18 mA/cm^2 can be demonstrated when $In_{0.46}Ga_{0.54}N$ top cell having a band gap of ~ 1.8 eV is integrated on Si bottom cell having a band gap of ~ 1.1 eV (Fig. 6a).⁹³ Hence, the p-type InGaN nanowires top cell was fabricated on a planar n^+-p Si bottom cell and the top and bottom light

absorbers are electronically connected through p^{++} -InGaN/ n^{++} -InGaN NW tunnel junction (Fig. 6b). In this structure, photogenerated electrons in the conduction band of Si bottom cell migrate to n^+ -InGaN segment, which then recombine with photogenerated holes in the valance band of p^{++} -InGaN segment in the tunnel junction (Fig. 6c). Meanwhile, the photogenerated electrons in the conduction band of top p -InGaN nanowires laterally diffuse to Pt nanoparticles cocatalysts due to downward surface band bending and finally participate in the H_2 evolution reaction.

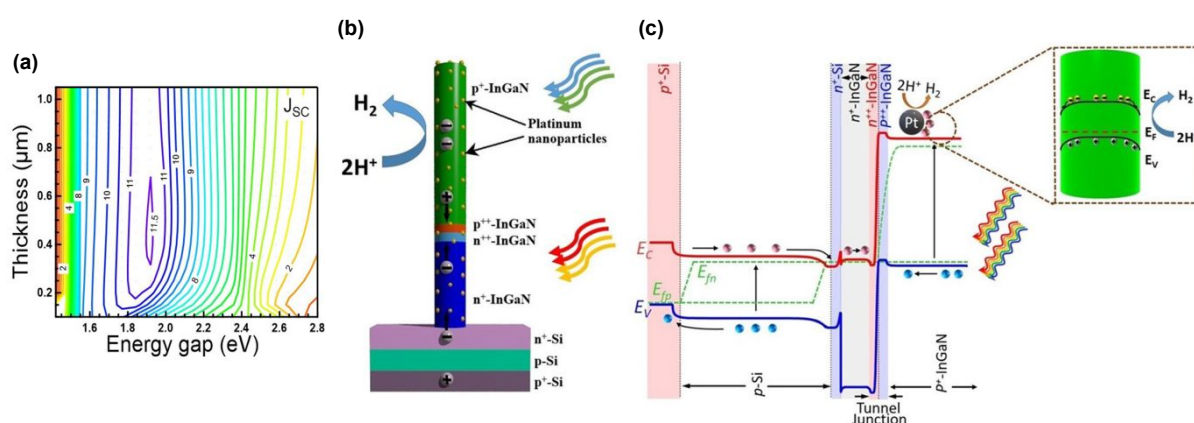


Fig. 6. (a) Theoretically calculated top p^+ -InGaN thickness and energy gap dependence of the short circuit current density of InGaN/Si double-junction photocathode. (b) Schematic of Pt decorated p^+ -InGaN/tunnel junction/ n^+ -InGaN nanowire on n^+ -p Si wafer. (c) Energy band diagram under light illumination, showing charge carrier generation in bottom Si and top p^+ -InGaN nanowire and electron migration to lateral surface of p^+ -InGaN for proton reduction reaction. Reproduced with permission from Ref. 93. Copyright (2021) AIP Publishing.

Even though the ideal band gap energy of InGaN top cell on Si bottom cell is ~ 1.8 eV, it is extremely challenging to grow the InGaN nanowires with high In composition ($\sim 46\%$) because of unavoidable defect formation and phase separation. Therefore, InGaN nanowires top cell having a band gap of 2.2 eV was integrated on n^+ -p Si bottom cell through a nearly defect-free n^+ -InGaN/ p^+ -InGaN NW tunnel junction for the photoelectrochemical H_2 evolution reaction (Figs. 7a and 7b).⁹⁴ Different from previous tunnel junction formed in Si bottom cell,⁸⁷ the tunnel junction was grown epitaxially in the InGaN nanowires (Figs. 7c-e). Since there is significantly reduced lattice mismatch, the high crystal-quality tunnel junction can be formed with much fewer defects and dislocations. Moreover, thin Al_2O_3 layer (1-2 nm) and Pt

nanoparticle cocatalysts were deposited on the InGaN nanowires to passivate the surface defects and to prevent corrosion of photocathodes, thereby leading to an enhanced water splitting performance and stability (Fig. 7f). To elucidate the photoelectrochemical water splitting activity, InGaN/Si double-junction photocathode (Sample B) was compared with n^+ -InGaN/Si single-junction photocathode without the tunnel junction (Sample A) (Fig. 7g). Single-junction InGaN/Si showed the onset potential of ~ 0.5 V_{RHE} whereas double-junction InGaN/Si remarkably increased the onset potential to ~ 2.3 V_{RHE}. The saturation photocurrent density for the double-junction cell was ~ 9 mA/cm² which is smaller than the single junction cell (~ 30 mA/cm²) because the photocurrent density of the double junction cell was limited by the top p^+ -InGaN nanowires (with a band gap of ~ 2.2 eV) whereas the Si-based single-junction photocathode has a theoretical maximum photocurrent density of ~ 44 mA/cm². In addition, InGaN/Si double junction photocathode exhibited an onset potential of ~ 0.7 V vs IrO_x counter electrode in 2-electrode configuration with a record-high solar-to-hydrogen (STH) efficiency of $\sim 10.3\%$ under AM 1.5G 1 sun illumination (Fig. 7h). This double junction photocathode provided sufficient built-in potential under solar light, leading to overall solar water splitting without additional electrical bias. Addressing the current matching issues of top and bottom cells through tunnel junction structure will further improve the photocurrent density while producing a built-in potential sufficient for overall water splitting.

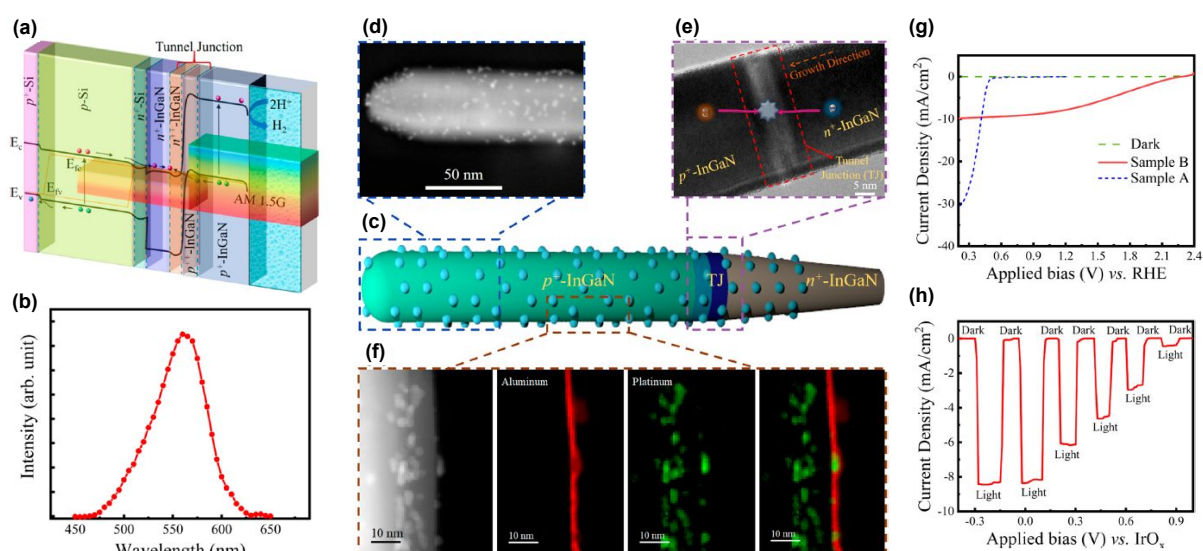


Fig. 7. (a) Band-diagram of the p^+ -InGaN/tunnel junction/ n^+ -p Si photocathode.⁹⁴ (b) Photoluminescence spectrum of p^+ -InGaN nanowires. (c) Schematic of single nanowire with

Pt cocatalysts and Al₂O₃ layer. (d) High angle annular dark field (HAADF) image of top p⁺-InGaN segment. (e) Bright-field image of tunnel junction region. The photogenerated holes from p⁺-InGaN top cell and electrons from bottom n⁺-InGaN recombine in the tunnel junction. (f) HAADF and elemental mapping showing Pt and Al₂O₃ on the nanowire sidewall. (g) Three-electrode linear scan voltammetry curves of InGaN/Si single-junction (Sample A) and double-junction (Sample B) photocathodes. (h) Two-electrode chopped photocurrent density curve of InGaN/Si double-junction in 0.5 M H₂SO₄ under AM 1.5G 1 sun illumination. Reproduced with permission from Ref. 94. Copyright (2020) American Chemical Society.

3.4. Crystal Orientation

Due to distinct atomic arrangements on the different crystal facets of semiconductor materials, anisotropic physical and chemical properties have been demonstrated. Electrical conductivity, surface adsorption of molecules, band edge position, and direction of charge carrier diffusion in the photoelectrodes are highly dependent on the crystal orientation. In addition, each crystal facet has different intrinsic reactivity dependent on the pH and applied potential. Hence, understanding crystal facet effects on photoelectrochemical water splitting activity and stability is an essential issue. Previously, specific crystal facets have been exposed to the surface of the various photoelectrodes of TiO₂,¹¹² Fe₂O₃,^{113, 114} WO₃,^{115, 116, 117} BiVO₄,^{118, 119} Cu₂O,^{120, 121} Sb₂Se₃,^{122, 123} and Ta₃N₅^{124, 125} by selective nucleation, growth, or etching process. The fine control of crystal orientations has exhibited improvement in activity and stability for both photoelectrochemical H₂ evolution and O₂ evolution reactions. Although various works have demonstrated efficient water splitting by optimization of the crystal structures of semiconductor materials, the effect of crystal facets of III-nitrides on the water splitting performance has been largely unknown. Recently, GaN quasi-films grown on n⁺-p Si photocathodes showed a gradual self-improvement of H₂ evolution activity during the initial several hours of chronoamperometry (CA) measurement in 0.5 M H₂SO₄ under 1 sun illumination at a cathodic bias of -0.6 V_{RHE} (Fig. 8a).⁹⁵ The linear sweep voltammetry (LSV) curves exhibited the positive shift of onset potential from -0.46 to -0.08 V_{RHE} after 10 h of CA test. Owing to the self-improving characteristic of GaN quasi-film, the loading amount of noble metal Pt cocatalyst can be greatly reduced. On the pristine GaN/Si photocathode, 20 min Pt deposition was required to achieve the onset potential of ~0.3 V_{RHE} meanwhile this onset potential can be demonstrated with 5 min Pt deposition on self-improved GaN/Si

photoelectrode (Fig. 8b), indicating that ~ 4 times reduced amount of Pt cocatalysts. To elucidate the reason for the self-improvement, photoconductive atomic force microscopy measurements have been carried out (Fig. 8c). Notably, pristine GaN and self-improved GaN showed similar surface morphology but a substantial difference in photocurrent profile. The photocurrent in self-improved GaN mainly flows through the side walls of the GaN grains, whereas the top surface barely contributes to the photocurrent (Fig. 8d). From the surface composition analysis of self-improved GaN through cross-sectional scanning transmission electron microscopy (STEM) measurement, 1 nm-thin layer with Ga, N, and O was observed at the side wall and relatively thick layer with Ga and O was formed on the top surface (Fig. 8e). Theoretical calculations suggested that partial substitution of nitrogen by oxygen during the reaction can stabilize GaON phase on the outermost layer of the nonpolar side wall whereas GaO phase is more preferred on the polar top surface (Fig. 8f). These different atomic compositions, originated from the crystal facets and polarity of GaN, shifted the H_2 evolution activity. The free energy of adsorption of hydrogen is smaller on GaON compared to pristine GaN non-polar side wall, thereby resulting in thermodynamically favorable production of H_2 .

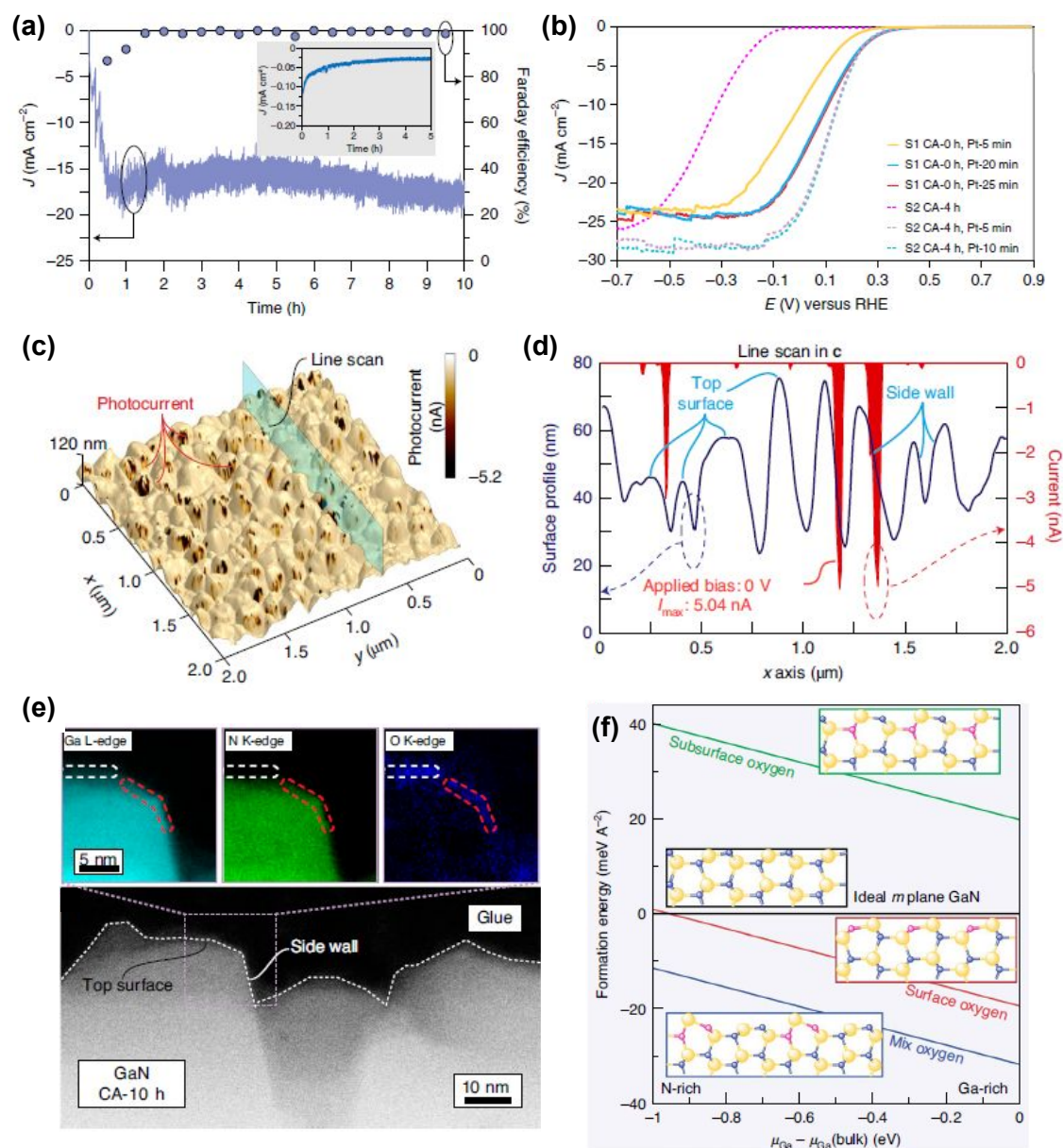


Fig. 8. (a) Current density and faradaic efficiency (FE) measurement of GaN quasi-film/ n^+ -p Si photocathodes for 10 h under 1 sun illumination at $-0.6 V_{RHE}$. Inset: Si control electrode. (b) LSV curves of pristine (CA-0 h) and 4 h-tested (CA-4h) GaN/Si photocathodes with different Pt deposition duration. (c) Topography of self-improved GaN quasi-film (CA-10 h) and (d) corresponding surface profile and photocurrent extracted from the line scan. (e) STEM image of CA-10 h surface with elemental mappings of Ga L-edge, N K-edge and O K-edge. (g) Calculated formation energy of nonpolar m -plane GaN surface with different oxygen configurations within the anion- and cation-rich limits. Reproduced with permission from Ref. 95. Copyright (2021) Springer Nature Limited.

Inspired by the previous investigation, a detailed study on the effect of crystal facet and surface polarity of wurtzite III-nitride on photoelectrochemical activities was carried out. To identify the impact of crystal orientations with different polarities, GaN nanostructures were fabricated by both top-down and bottom-up methods, which allow the exposure of certain facets (polar top surface or nonpolar side wall) to the electrolyte (Fig. 9a).⁹⁶ First, the GaN quasi-film (Sample A) was grown on the n⁺-p Si wafer with preferential orientation along the c-plane direction (Fig. 9b). Then, patterning processes (photolithography and dry etching) were conducted to expose the nonpolar m-plane side walls (Sample B). Even though a high photocurrent density ($\sim 40 \text{ mA/cm}^2$) is expected from a Si-based photocathode under 1 sun solar light, Sample A showed negligible photocurrent density (Fig. 9c). In stark contrast, Sample B exhibited a much better onset potential of $\sim 0.45 \text{ V}_{\text{RHE}}$ and saturation photocurrent density of $\sim 18 \text{ mA/cm}^2$. Given that Sample A and Sample B are nearly identical except for the exposed nonpolar surfaces to the electrolyte, it is therefore found that the nonpolar surfaces of GaN are responsible for the H₂ evolution reaction. Furthermore, GaN nanowire arrays were grown on the n⁺-p Si wafer. Then, their surface exposure to the electrolyte was controlled by the deposition of an insulating parylene passivation layer, followed by an etch-back process to reveal the top portions of the GaN nanowires. The as-grown GaN nanowire/Si photocathode with Pt cocatalysts exhibited an onset potential of $0.45 \text{ V}_{\text{RHE}}$ and a maximum photocurrent density of 28 mA/cm^2 (Fig. 9d). Then, there was no photoresponse when the insulating passivation layer was deposited. However, after an initial etch-back process, the exposure of active nonpolar sidewalls of GaN nanowires greatly improved the performance. To understand the fundamental difference in the activity between polar and nonpolar planes, the role of oxygen was studied by density functional theory calculation. For the nonpolar surface, the most stable configuration was found to be gallium oxynitride formed by partial replacement of nitrogen by oxygen (Fig. 9e). On the other hand, for the polar surface, the most stable configuration was an oxygen-rich condition, which induces strong surface polarization and upward band bending at the surfaces (Fig. 9f). This observation describes the reason for the facilitated electron transport at the nonpolar plane and limited transport at the polar one. It is therefore evident that selective exposure of desired crystal facets of III-nitride nanostructure can enhance charge carrier transport and photoelectrochemical water splitting activity.

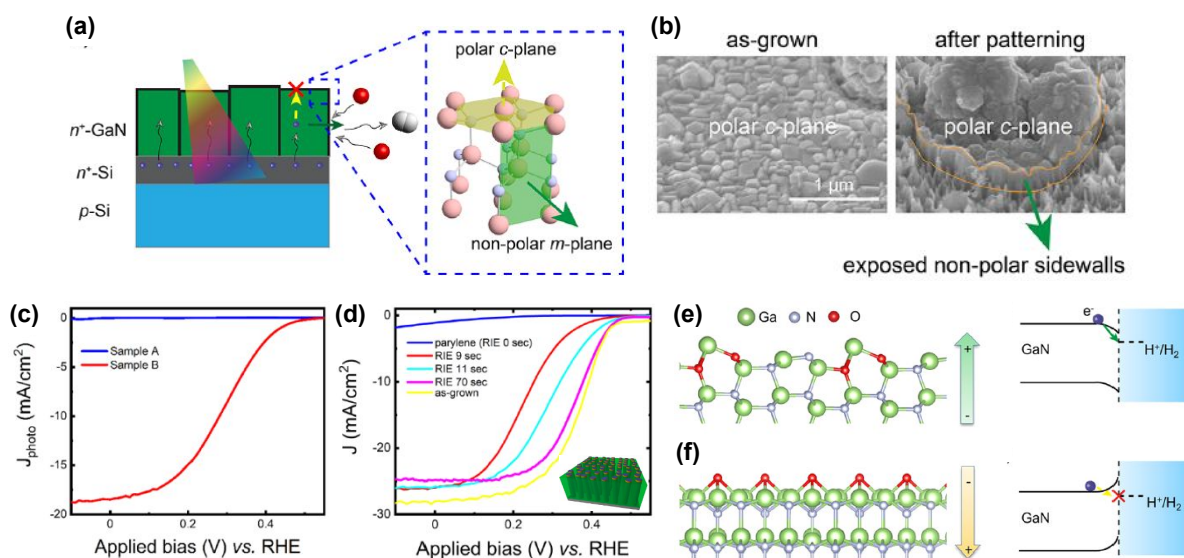


Fig. 9. (a) Schematic illustration of H₂ evolution reaction on polar c-plane and nonpolar m-plane of wurtzite structure GaN. Photoexcited electrons preferentially migrate to the GaN nonpolar surfaces and reduce protons to H₂. (b) SEM images of GaN quasi-film (Sample A) and that exposed the nonpolar sidewalls by patterning process (Sample B). (c) LSV curves of samples A and B in 0.5 M H₂SO₄ under AM 1.5G 1 sun illumination. (d) H₂ evolution reaction of parylene-coated GaN nanowires. Longer durations of etch back exposed greater amounts of GaN nanowire nonpolar sidewalls. Schematic of configurations for surface polarization and surface energy band diagrams of (e) nonpolar m-plane with oxygen partial substitution and (f) polar c-plane with oxygen adsorption. Reproduced with permission from Ref. 96. Copyright (2022) American Chemical Society.

3.5. Protective 1D nitrides for long-term stability

Many semiconductor photoelectrodes have been studied and developed for photoelectrochemical water splitting with a proper decoration of cocatalysts or modification of nanostructures.^{126, 127, 128, 129, 130} However, most photoelectrodes with relatively high photocurrent density, such as Si and III–V semiconductors, suffer from the corrosion reaction in aqueous electrolytes because these materials have a very narrow window of stability based on Pourbaix diagrams.¹³¹ To prevent cathodic or anodic corrosion during the water splitting reaction, the photocathode should have the material's self-reduction potential above the energy level of H₂O/H₂ and the photoanode should have the material's self-oxidation potential below the energy level of O₂/H₂O.¹³² Several metal oxides such as TiO₂¹³³ and Al₂O₃¹³⁴ satisfy these

thermodynamic requirements, and thus, have been used as protective layers for photoelectrodes. However, the charge carriers in metal oxides are known to have poor mobilities and short diffusion lengths. Moreover, unsuitable band alignment at the metal oxide/semiconductor interface is a major obstacle to realizing efficient photoelectrodes. To mitigate these limitations, N-terminated GaN nanowire arrays have been fabricated as multifunctional protection structures for the underlying n⁺-p Si photoelectrode (Figs. 10a and 10b).⁹⁷ GaN nanowires have several advantages of optical transparency, conduction band alignment between GaN and Si photocathode, and large surface area. GaN nanowires with large band gap (~3.4 eV) are transparent for visible and infrared light and allow Si photoelectrode to absorb broadband solar light. Also, the conduction band edges of n-type GaN nanowire and n⁺-Si are approximately aligned, so the photogenerated electrons can efficiently transfer from Si to GaN without significant electrical resistance (Fig. 10c). Moreover, the large surface area of GaN nanowires can be loaded with Pt cocatalysts and behave as active sites for the H₂ evolution reaction. As a result, Pt-decorated GaN/Si photocathodes showed a high saturated photocurrent density of ~38 mA/cm² with a promising onset potential of ~0.5 V_{RHE} in 0.5 M H₂SO₄ under 1 sun light illumination (Fig. 10d). More notably, the Pt-decorated GaN/Si photocathodes showed excellent stability up to 3000 hours with relatively stable photocurrent densities of 37-38 mA/cm² at 0 V_{RHE}.¹³⁵ Owing to the excellent physical and chemical stability of GaN nanowires,¹³⁶ GaN nanostructures also have been deposited on III-V GaInP₂/GaAs/Ge triple-junction photocathode as a protective scheme (Fig. 10e).⁹⁸ The GaN-protected triple-junction photocathode exhibited a saturated photocurrent density of 10.3 mA/cm², an onset potential of 2.2 V_{RHE}, and an ABPE of 12.6% (Fig. 10f). This photocathode can continuously work for 80 h without degradation (Fig. 10g), indicating the excellent stability, compatibility, and integrability of GaN nanostructures with high-performing semiconductors of Si and III-V photoelectrodes.

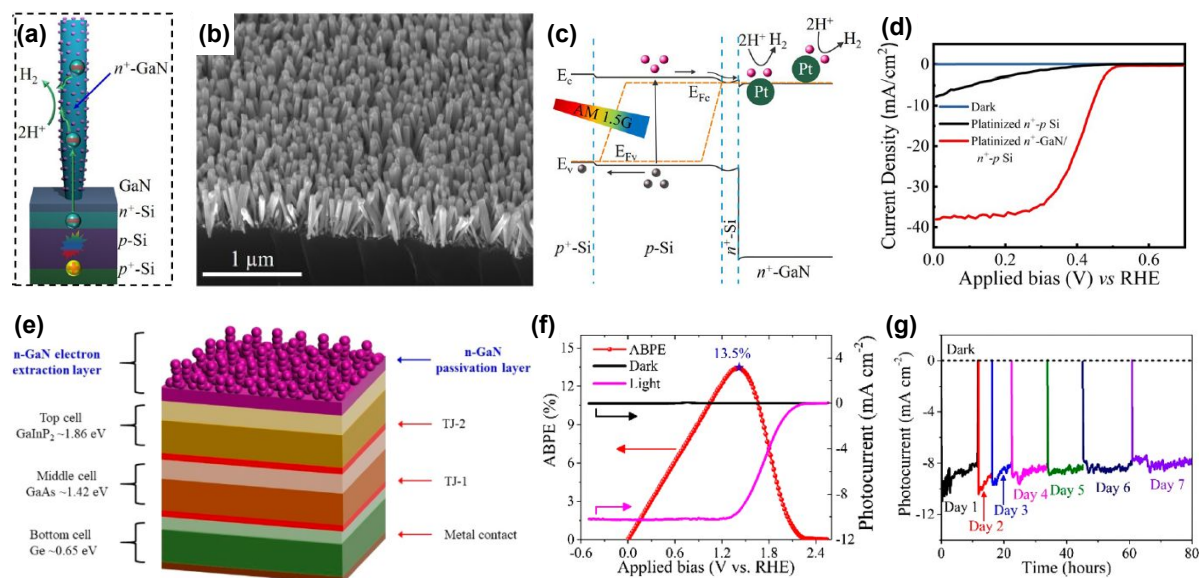


Fig. 10. (a) Schematic of GaN nanowire-protected n⁺-p Si photocathode with Pt cocatalysts. (b) SEM image of GaN/Si photocathode. (c) Schematic of the energy band diagram of Pt-decorated GaN/Si photocathode under light illumination. (d) LSV curves measured under AM 1.5G 1 sun illumination in 0.5 M H₂SO₄. Reproduced with permission from Ref. 97. Copyright (2018) American Chemical Society. (e) Schematic illustration of the GaInP₂/GaAs/Ge triple-junction photocathode protected by GaN nanostructures. (f) Photoelectrochemical H₂ evolution reaction performance and (g) long-term stability of GaN-protected triple-junction photoelectrode in 0.5 M H₂SO₄ under 1 sun light. Reproduced with permission from Ref. 98. Copyright (2019) American Chemical Society.

A green H₂ fuel can be produced by photoelectrolysis of seawater, which is the most abundant water source on earth. However, due to the sluggish water dissociation reaction, unfavorable precipitation of insoluble salts (*e.g.*, Mg(OH)₂ and Ca(OH)₂), and most importantly, poor stability of semiconductors in harsh reaction conditions, application of photoelectrode for seawater splitting has been limited. However, GaN nanowires, grown on n⁺-p Si photoelectrode, have enabled efficient and stable seawater H₂ evolution once Pt nanoclusters were decorated on the sidewalls of nanowires (Fig. 11a).⁹⁹ Compared to water dissociation on Pt, the heterolytic cleavage of the water molecule at a Pt-Ga site was facilitated due to the asymmetric atomic environment (Fig. 11b). The overall energy change of water splitting at the Pt/GaN interface is -0.81 eV, indicating spontaneous reaction without thermodynamic energy barrier. Owing to the benefits from the synergistic interaction between

GaN and Pt, an onset potential ($0.16 \text{ V}_{\text{RHE}}$) and a saturated photocurrent densities ($\sim 35 \text{ mA/cm}^2$) of Pt/GaN/Si outperformed the other control devices (Fig. 11c). Moreover, Pt/GaN/Si photocathode revealed a gradual increase in the saturated photocurrent densities, reaching $\sim 165 \text{ mA/cm}^2$ at -3.2 V under concentrated solar light (9 sun) illumination in 2-electrode configuration (Fig. 11d). Accordingly, the production rate of H_2 gradually increased from 359 (under 1 sun light) to $3351 \text{ }\mu\text{mol/cm}^2/\text{h}$ (under 9 sun light) while the faradaic efficiency was nearly 100% regardless of the light intensity (Fig. 11e). Therefore, GaN nanowire-protected Si photoelectrode is a promising platform for an efficient, stable, and energy-saving electrode for solar-assisted H_2 generation by seawater splitting.

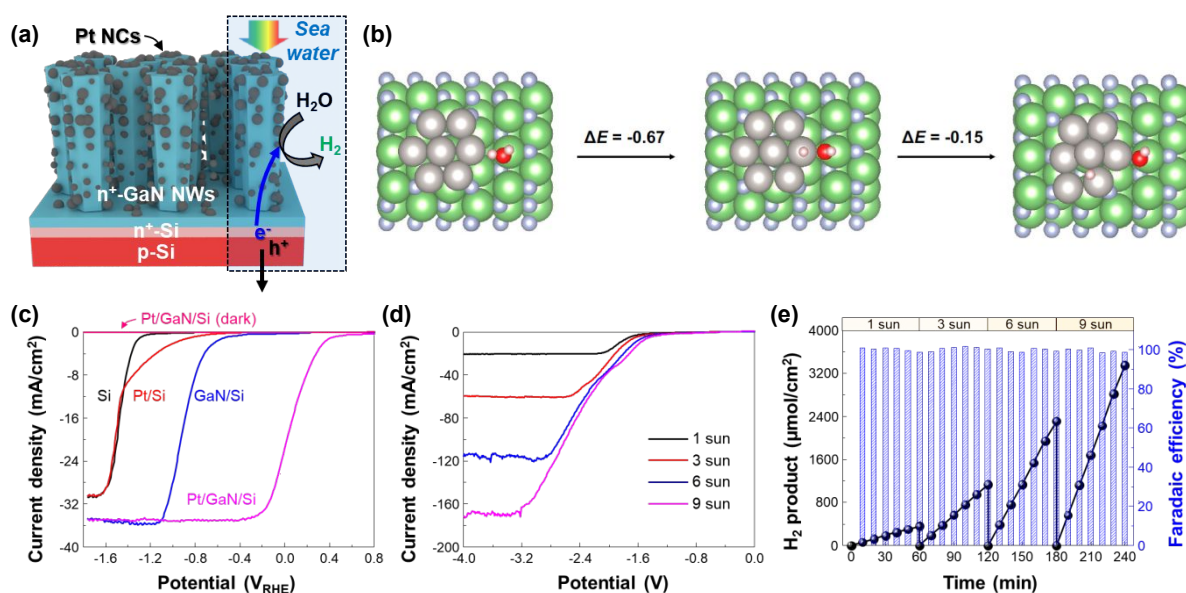


Fig. 11. (a) Schematic illustration of the Pt/GaN/Si photocathode for seawater H_2 evolution. (b) Optimized structures and calculated energy changes of water dissociation at Pt-Ga site and subsequent H spillover to Pt surface. All energy changes are in the unit of eV. The white, red, blue, green, and grey spheres represent H, O, N, Ga, and Pt atoms, respectively. (c) LSV curves of Si, Pt/Si, GaN/Si, and Pt/GaN/Si measured with 3-electrode configuration in 0.5 M NaCl solution under AM 1.5G 1 sun illumination or in dark. (d) LSV curves of Pt/GaN/Si measured with 2-electrode configurations in 0.5 M NaCl under different light intensities. (e) Amount of H_2 product and faradaic efficiency measured under light intensities of 1, 3, 6, and 9 suns at -3 V . Reproduced with permission from Ref. 99. Copyright (2023) Springer Nature Limited.

4. Photocatalytic water splitting

In contrast to the photoelectrochemical water splitting driven by solar light and electrical bias, photocatalytic water splitting, often referred to as type-I or type-II photoelectrochemical water splitting, is completely wireless overall water splitting operated only by solar light as energy input. Moreover, in photocatalytic water splitting, pH-neutral pure water, or seawater can be readily utilized, in contrast to strongly acidic or basic electrolytes commonly required for conventional photoelectrochemical water splitting. Therefore, photocatalytic water splitting is more amenable for scaled-up production of solar hydrogen with reduced cost and enhanced stability. When the incident light illuminates the photocatalysts in water, the photocatalysts absorb the photons with energy larger than the band gap by exciting electrons in the conduction band and holes in the valance band, respectively. Then, the photoexcited electrons and holes separate and transport to the surface active sites for the catalytic reactions. Because both water oxidation ($\text{H}_2\text{O} + 2\text{h}^+ \rightarrow 1/2\text{O}_2 + 2\text{H}^+$) and reduction reactions ($\text{H}_2\text{O} + 2\text{e}^- \rightarrow \text{H}_2 + \text{OH}^-$) occur at a photocatalyst, the semiconductor photocatalysts for overall water splitting should satisfy the requirements of band edge positions which must straddle the water reduction and oxidation potentials. Moreover, the catalytic activity for stabilizing reaction intermediates is necessary to kinetically and thermodynamically enhance the productivity and selectivity of H_2 and O_2 . Therefore, it is highly desirable to develop a photocatalyst material with a suitable band gap, band edge position, and surface active site for overall water splitting. Up to now, some metal oxides (*i.e.*, TiO_2 and SrTiO_3) have demonstrated overall solar water splitting since they satisfy the requirements of band edge positions.^{137, 138} However, those metal oxides possess relatively large band gaps due to the deeper-lying O 2p orbitals in the valance band edge. Consequently, they are photo-responsive only to ultraviolet light, which resulted in limited efficiency. In contrast, III-nitrides have a smaller band gap and less positive valance band edge positions mainly consisting of N 2p orbitals. Therefore, 1D III-nitrides, such as InGaN nanowires, have shown great promise in photocatalytic water splitting (Table 3). The efficiency-enhancement strategies such as band gap engineering, doping for surface band bending, and loading of cocatalysts are introduced in the following sections.

Table 3. III-nitride photocatalysts for photocatalytic overall water splitting.

Photocatalysts	Cocatalysts	Solution	Light source	Performance	Ref.
p-InGaN/GaN NWs	Rh/Cr ₂ O ₃	Artificial seawater	300 W Xe lamp	STH conversion efficiency = 1.9%	139
InGaN/GaN NWs	Rh/Cr ₂ O ₃ and Co ₃ O ₄	H ₂ O	300 W Xe lamp with AM 1.5G filter	STH conversion efficiency = 2.7%	140
InGaN/GaN core/shell NWs	Pt	220 ml H ₂ O with 50 ml CH ₃ OH	300 Xe lamp (1044 mW/cm ²)	H ₂ production rate = 253.3 μmol/g/h	141
InGaN/GaN NWs	Rh/Cr ₂ O ₃	H ₂ O	300 W Xe lamp	H ₂ production rate = ~92 mmol/g/h	142
quadruple-band InGaN NWs	Rh/Cr ₂ O ₃ and Co ₃ O ₄	H ₂ O	300 W Xe lamp with AM 1.5G filter	STH conversion efficiency = ~5.2%	143
Mg-doped GaN NWs	Rh/Cr ₂ O ₃	H ₂ O	300 W Xe lamp with > 375 nm filter	H ₂ + O ₂ production rate = ~570 mmol/g/h	144
p-GaN NWs	Rh/Cr ₂ O ₃	H ₂ O	300 W Xe lamp	H ₂ production rate = ~4 mol/g/h	145
p-GaN/InGaN NWs	Rh/Cr ₂ O ₃	H ₂ O	300 W Xe lamp with AM 1.5G filter	STH conversion efficiency = 1.8%	146
Mg-doped InGaN nanosheets	Rh/Cr ₂ O ₃	H ₂ O	300 W Xe lamp with AM 1.5G filter	STH conversion efficiency = 3.3%	147
GaN nanorods	Rh and CoO _x	H ₂ O	300 W Xe lamp	quantum efficiency = 6.9%	148
InGaN/GaN NWs	Rh/Cr ₂ O ₃ /Co ₃ O ₄	H ₂ O at 70 °C	300 W Xe lamp with AM 1.5G filter	STH conversion efficiency = 9.2%	149

4.1. Band gap engineering of 1D nitrides

Different from conventional photocatalysts in powder form, GaN nanowires, vertically grown on Si wafer, have a single-crystalline structure with a small number of defects, resulting in efficient charge carrier transport to the surface active sites for photocatalytic water splitting. Hence, GaN nanowires decorated with Rh/Cr₂O₃ core/shell nanoparticles have been fabricated wherein the GaN is responsible for the O₂ evolution reaction, the Rh core promotes the H₂

evolution reaction, and the Cr_2O_3 shell prevents the backward reaction (Fig. 12a).¹⁵⁰ From TEM characterization, it was found that GaN nanowires have a single crystalline structure and are uniformly coated by metallic Rh/ Cr_2O_3 core/shell nanoparticles (Fig. 12b). Photocatalytic water splitting has been successfully carried out on the 1D GaN nanowires with Rh/ Cr_2O_3 cocatalysts in pure water under light irradiation. During ~ 18 h of reaction, the stoichiometric ratio (2:1) of H_2 and O_2 gases was steadily generated (Fig. 12c).

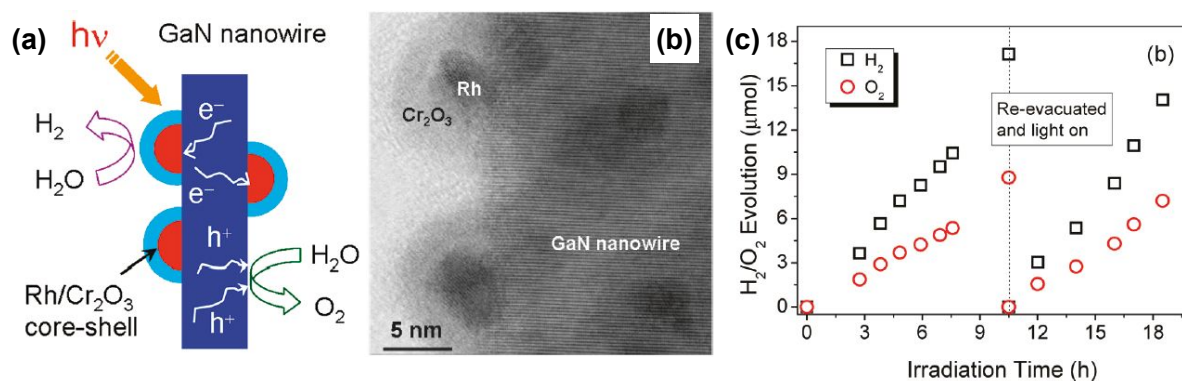


Fig. 12. (a) Schematic illustration of photocatalytic water splitting on GaN nanowire with Rh/ Cr_2O_3 core/shell nanoparticle cocatalysts. (b) High-resolution TEM image of Rh/ Cr_2O_3 cocatalysts on GaN nanowire. (c) H_2 and O_2 evolution under a 300 W full arc xenon lamp irradiation for a duration of 18 h. Reproduced with permission from Ref. 150. Copyright (2011) American Chemical Society.

Although a wafer-level photocatalytic water splitting has been demonstrated by GaN nanowires, a very small portion of solar light (mostly ultraviolet light) can be absorbed due to the large band gap (~ 3.4 eV). The band gap of $\text{In}_x\text{Ga}_{1-x}\text{N}$ can be ideally controlled from 3.4 eV to 0.65 eV, and thus, visible-to-near infrared solar spectrum can be used for photocatalytic overall water splitting. However, it is extremely challenging to grow the InGaN nanowires with narrow band gap due to phase-separation issues and increase in the number of detrimental defects. Moreover, the decrease in band gap energy of III-nitride semiconductors inevitably shifts the valence band edge potential to more negative and/or the conduction band edge positions to more positive direction, thereby resulting in the decrease in the redox ability. To mitigate these issues, multi-band InGaN/GaN nanowire photocatalysts have been developed for enhancing the STH efficiency.^{139, 140, 141} For example, sequential deposition of GaN (band gap = 3.4 eV),

InGaN quantum dots (2.22 eV), and InGaN well (2.96 eV) reduced the lattice mismatch at the hetero-interfaces and enabled the epitaxial growth of nanowire photocatalysts with multi-band structure (Figs. 13a-c).¹⁴² HAADF image of InGaN/GaN nanowire exhibited obvious atomic number contrast and the presence of 10 InGaN/GaN quantum dots located along the axial direction of the nanowire (Fig. 13d). InGaN/GaN nanowires with Rh/Cr₂O₃ cocatalysts showed overall pure water splitting under light illumination. High production rate of H₂ (~683 μmol) and O₂ (~373 μmol) was concurrently demonstrated during 18 h of reaction (Fig. 13e), indicating that the broader band light absorption induced the more photogenerated charge carriers and promoted the photocatalytic water splitting reactions compared to GaN nanowires. Furthermore, quadruple-band In_xGaN_{1-x} nanowires consisting of continuous In_{0.35}Ga_{0.65}N (2.10 eV), In_{0.27}Ga_{0.73}N (2.40 eV), In_{0.20}Ga_{0.80}N (2.60 eV), and GaN (3.40 eV) segments have been successfully grown on Si wafer by MBE (Fig. 13f).¹⁴³ The In_xGaN_{1-x} nanowires showed an inversely tapered morphology (Fig. 13g) and 4 distinct regions with different In content (Fig. 13h). Besides, a gradient doping of Mg along the lateral dimension of the nanowires induces an internal electric field, which facilitates the electron-hole separation (The effect of Mg doping in InGaN nanowires will be described in the following section 4.2). These advantageous optoelectronic properties of quadruple-band In_xGaN_{1-x} nanowires greatly enhanced the photocatalytic overall water splitting and achieved a high STH (Fig. 13i).

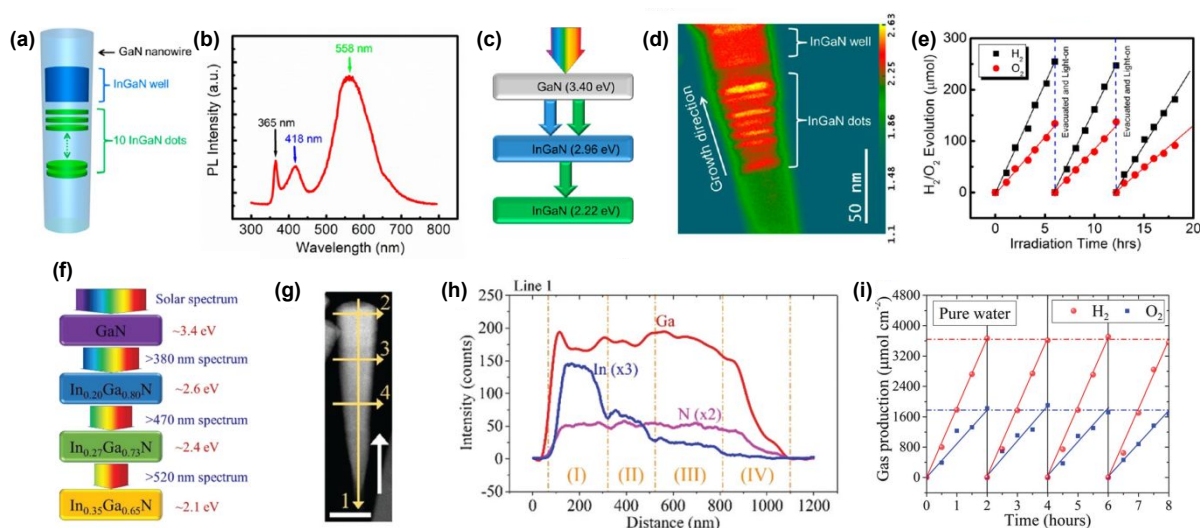


Fig. 13. (a) Schematic and (b) photoluminescence spectra of InGaN/GaN nanowires. (c) Band gap energy of each segment. (d) HAADF image in pseudocolor display of InGaN/GaN

nanowire, showing the atomic number contrast between InGaN (red) and GaN (green) segments. (e) Overall pure water splitting on Rh/Cr₂O₃ decorated InGaN/GaN nanowires under full arc (> 300 nm) 300 W xenon lamp irradiation. Reproduced with permission from Ref. 142. Copyright (2013) American Chemical Society. (f) Schematic light absorption sequence and (g) TEM image of quadruple-band InGaN nanowire with varied indium compositions. (h) Energy-dispersive X-ray spectroscopy line scanning showing the variation of Ga, In, and N elements along the axial direction. (i) Photocatalytic H₂ and O₂ gas evolution as a function of time. Reproduced with permission from Ref. 143. Copyright (2019) Royal Society of Chemistry.

4.2. Doping of 1D nitrides

Intrinsic III-nitrides can be changed to p-type semiconductors with Mg doping. Hence, the effect of Mg dopant in GaN nanowires on light response, charge carrier transport, and photocatalytic activity of overall water splitting has been investigated. To vary the amount of Mg dopant, Mg effusion cell temperature was changed from 190 to 315 °C during the MBE growth of GaN nanowires.¹⁴⁴ Low-temperature (20 K) photoluminescent spectra of pristine GaN showed a single peak at 3.435 eV, corresponding to donor-bound exciton. With a little amount of Mg doping (200 °C), GaN:Mg nanowires showed two additional peaks at 3.254 and 3.189 eV, which are attributed to the conduction band to Mg-related acceptor level (Fig. 14a). With further increase in the amount of Mg dopant (260 °C), a new broad photoluminescence peak at 2.95 eV appeared due to the donor-acceptor-pair transition between the N-vacancy deep donor states and shallow Mg acceptor states. With the intra-gap defect states which straddle the redox potential of water (Fig. 14b), GaN:Mg nanowires enable the broadband light absorption and enhance the performance of overall water splitting (Fig. 14c). However, it should be noted that further incorporation of Mg dopant in GaN nanowires (> 260 °C) drastically degrade the water splitting activity because of poor crystal quality and undesirable non-radiative recombination of photogenerated carriers. Hence, optimized doping of III-nitrides photocatalysts can broaden the light-responsive wavelength, and accordingly, increase the productivity of overall water splitting under solar light irradiation.

Moreover, some previous studies revealed that n-type and p-type doping of GaN surfaces results in the upward and downward band bending once water is adsorbed on the surface, respectively, which can promote the separation of photogenerated electron-hole pairs at the semiconductor/water interface.^{151, 152} Since GaN nanowires have weakly n-type nature with

Fermi level locates higher than the redox potential of water, the fine-tuning of the p-type dopant in GaN nanowires can reduce the downward band bending and provides an opportunity to realize the balanced surface band structure for efficient photocatalytic water splitting reactions.¹⁴⁵ The amount of p-type Mg dopant was in-situ controlled during the MBE growth of GaN nanowires by varying the Mg effusion cell temperature (T_{Mg}). Then, the near-surface band structure of GaN:Mg nanowire was investigated by measuring the Fermi level position (E_{F}) relative to the valence band maximum (E_{V}) by X-ray photoelectron spectroscopy (Fig. 14d). The $E_{\text{F}}-E_{\text{V}}$ was 2.63 eV for undoped GaN, indicating n-type semiconductor property. However, as T_{Mg} increased over 240 °C, the near-surface $E_{\text{F}}-E_{\text{V}}$ dramatically decreased due to the increased free hole concentration in GaN nanowires by p-type doping. To evaluate the effect of surface band bending on photocatalytic water splitting, H_2 and O_2 half reactions were measured in the presence of sacrificial reagents in the electrolytes. The H_2 production rate of p-type GaN nanowires was much higher than n-type GaN nanowires owing to downward band bending (Fig. 14e). On the other hand, the O_2 production rate of n-type GaN nanowires was significantly enhanced due to efficient hole transport by upward band bending (Fig. 14f). Hence, to demonstrate efficient overall water splitting, it is desirable to construct nearly flat band profile at the GaN/water interface. Consequently, the optimum incorporation of p-type Mg dopants in GaN nanowires decreased the downward band bending, which led to an improvement in STH efficiency by more than two orders of magnitude compared to n-type GaN nanowires (Fig. 14g). Moreover, it is also found that this p-type doping strategy is applicable to visible light-responsive InGaN nanowires.¹⁴⁶ The gradual decrease in near-surface $E_{\text{F}}-E_{\text{V}}$ (gradual change from n-type to p-type) was observed with the increasing amount of Mg dopant in InGaN nanowires. With optimized InGaN:Mg nanowires, a high yield of H_2 evolution (~ 0.8 mol/h/g) and STH efficiency (1.8%) were achieved with stoichiometric O_2 evolution under the visible light wavelength.

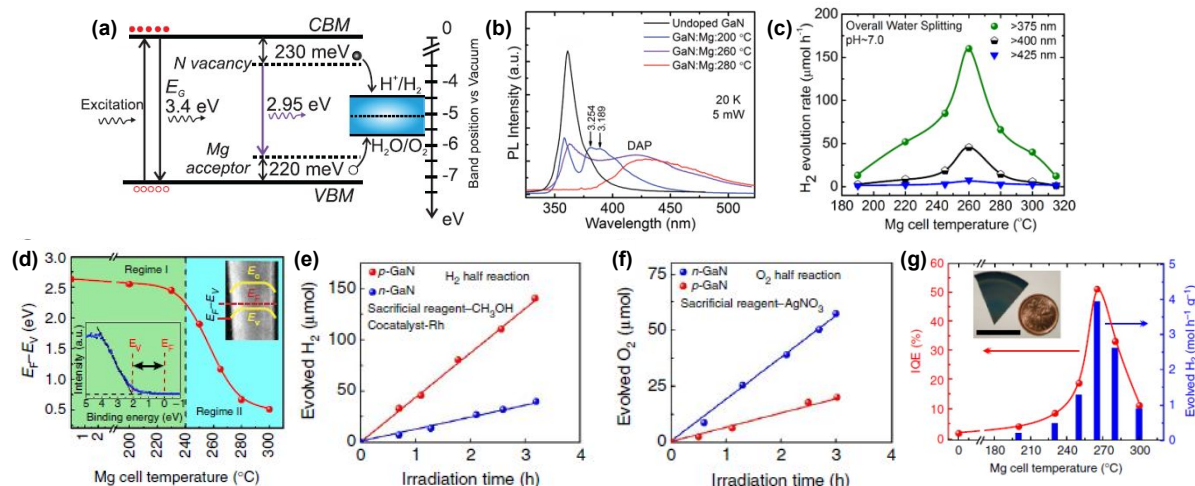


Fig. 14. (a) Schematic energy band diagram of Mg-doped GaN nanowires. (b) Low temperature photoluminescence spectra of GaN:Mg and undoped GaN nanowires. (c) H_2 evolution rate from photocatalytic water splitting from the GaN:Mg samples under 300W Xenon lamp. Reproduced with permission from Ref. 144. Copyright (2015) AIP Publishing. (d) Plot of $E_F - E_V$ for different GaN:Mg nanowires. Regime I and II indicate n-type and p-type surfaces, respectively. (e) H_2 and (f) O_2 evolution reactions from n- and p-type GaN nanowires in the presence of sacrificial reagents. (g) H_2 evolution rate and internal quantum efficiency for different GaN:Mg nanowires in overall pure water splitting. Reproduced with permission from Ref. 145. Copyright (2014) Nature Publishing Group, a division of Macmillan Publishers Limited.

In addition to surface band bending, a built-in potential in bulk regions of III-nitride is highly desired for efficient charge carrier separation. Previously, two-dimensional p-type InGaN nanosheets with gradient Mg doping have been developed as photocatalysts for overall water splitting (Fig. 15a).¹⁴⁷ During the growth, Mg dopants were impinged preferentially on one side, thereby leading to gradient doping of Mg along the lateral dimension of the nanosheets. This configuration induced a strong internal electric field that separates the electrons in the conduction band and holes in the valence band toward opposite surfaces with significantly suppressed non-radiative recombination (Fig. 15b). From the near-surface band structures of p-InGaN nanowires and nanosheets (Fig. 15c), the sharp change in $E_F - E_V$ (~ 300 mV) vs. scanning angle on p-InGaN nanosheets was observed. This confirmed that there is a strong internal electric field within the nanosheet due to the Mg dopant gradient from one side to the

other (Fig. 15d). In contrast, p-InGaN nanowires showed nearly constant E_F-E_V regardless of scanning angles because of the symmetric morphology of nanowires. As a result, p-InGaN nanosheets realized remarkable activity enhancement of photocatalytic water splitting reaction over p-InGaN nanowires and achieved impressive STH efficiency of $\sim 3.3\%$ (Fig. 15e).

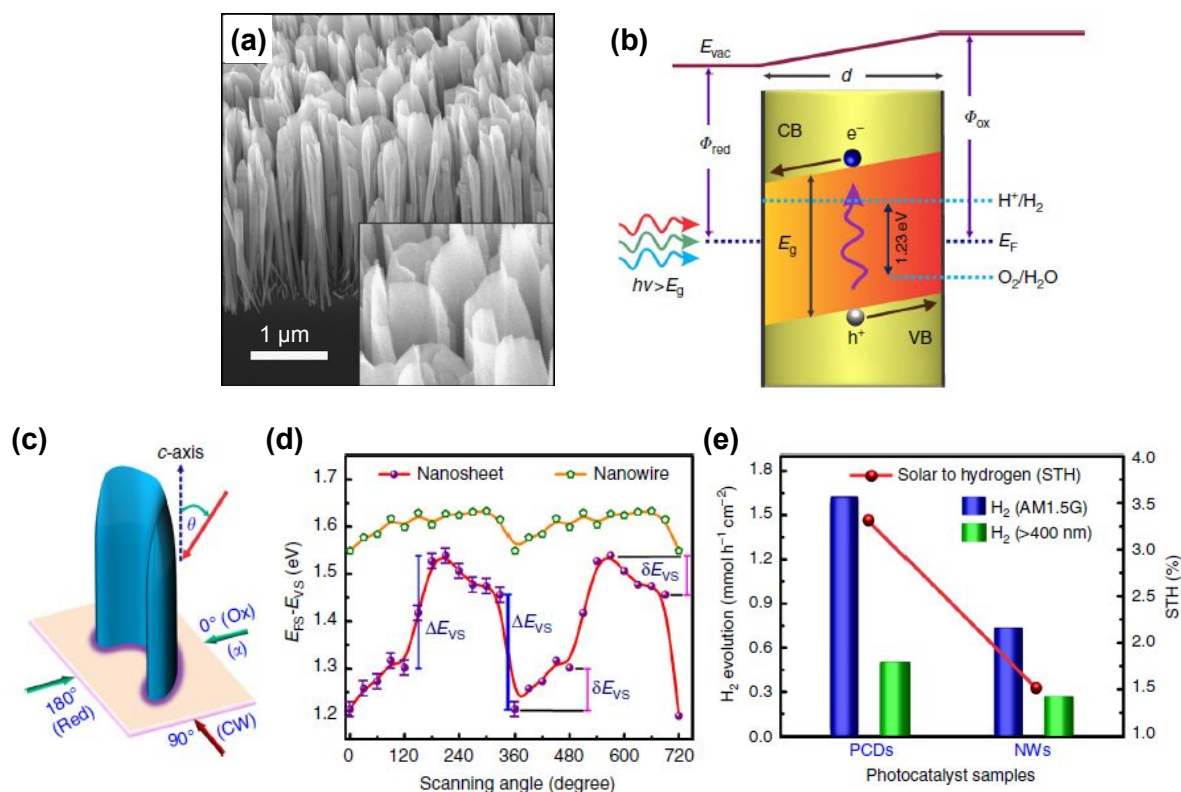


Fig. 15. (a) SEM image of Mg-doped p-InGaN nanosheets vertically grown on Si substrate. (b) Energy-band diagram of p-InGaN nanosheet with radial thickness “d” showing the built-in electric field (band-bending) that separates the electron and hole towards the opposite surfaces. (c) Schematic illustration of probing the surface valence band spectra using X-ray photoelectron spectroscopy. (d) $E_{FS}-E_{VS}$ for Mg-doped InGaN nanosheets and nanowire arrays as a function of radial scanning angle (α). (e) H_2 evolution rate in overall water splitting for photochemical diodes (nanosheets) and nanowires under different excitation conditions. All the photocatalysts were decorated with Rh/Cr₂O₃ cocatalysts. Reproduced with permission from Ref. 147. Copyright (2018) Springer Nature Limited.

4.3. Polarity of 1D nitrides

The ionic bonds in a unit cell of crystalline III-nitride semiconductors can induce electric

dipole moments, thereby resulting in positive charges on one surface and negative charges on the other side, which then produces a substantial electric field directing from the regions positively poled to those negatively poled. This electric field can redistribute the photogenerated charge carriers in III-nitrides and have a great influence on photocatalytic water splitting reactions. It has been well known that GaN is generally grown along the polar *c*-axis [0001] direction on the *c*-plane sapphire substrate, resulting in the exposure of the polar surface (Ga-polar or N-polar).¹⁵³ In order to expose the buried nonpolar plane (parallel to *c*-axis) to the surface, n-type GaN film was etched into nanorod arrays (Fig. 16a).¹⁴⁸ Thus, the GaN nanorod arrays have a top polar surface (Ga-polar) and a nonpolar side surface. Based on the surface band bending analysis, it was found that the upward band bending of the polar surface is more pronounced than the nonpolar surface, which leads to the spatial separation of photogenerated electrons to the nonpolar surface and holes to the polar surface, respectively (Fig. 16b). The charge separation characteristics of GaN nanorod arrays can be investigated through photochemical deposition method, in which reduced metals and oxidized metal oxides are coated on the electron-rich sites and hole-rich sites, respectively. After the photodeposition of Au, Rh, and Ag through the reduction of metal ions, metal nanoparticles were selectively coated on the nonpolar surface (side surface) (Figs. 16c and 16d). In stark contrast, MnO_x and CoO_x, deposited through oxidation reaction, were found on the polar surface (top surface) (Figs. 16e and 16f). Owing to the polarity-driven electron-hole separation to redox active sites, the GaN nanorod arrays exhibited much higher photocatalytic water splitting activity compared to GaN film (Fig. 16g). In addition, the selective deposition of CoO_x and Rh cocatalysts on the respective top and side surfaces greatly enhanced the overall water splitting (Fig. 16h).

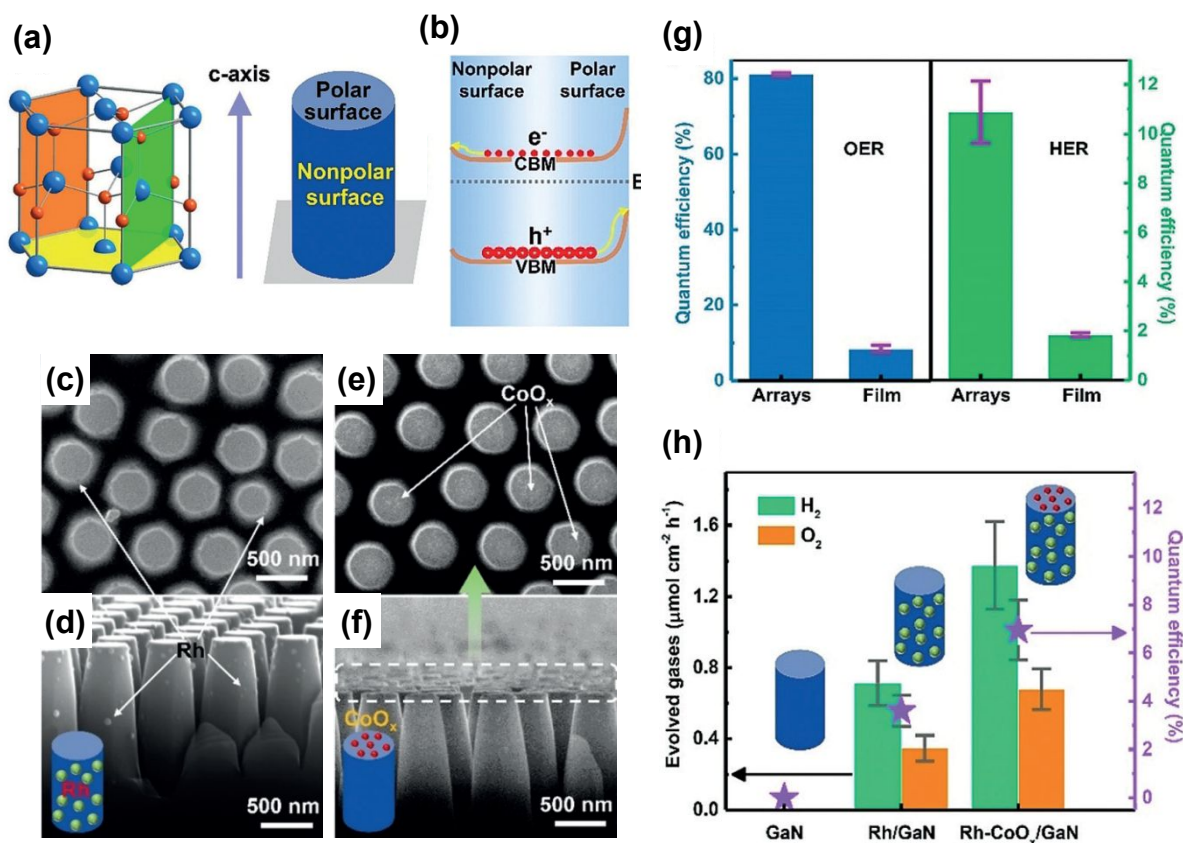


Fig. 16. (a) Schematic representation of polar c-plane (yellow), nonpolar a-plane (green), and m-plane (orange) of GaN crystal, as well as the surface polarity of the GaN nanorod arrays.¹⁴⁸ (b) Schematic representation of different band bending on the polar and nonpolar surfaces and the resulting spatial charge separation. (c) SEM images of the GaN nanorod arrays with (c,d) Rh and (e,f) CoO_x cocatalysts. (g) Photocatalytic O_2 and H_2 evolution reaction on the GaN nanorod arrays and film coated with Rh and CoO_x cocatalysts. (h) Photocatalytic overall water splitting on the GaN nanorod arrays without and with the cocatalysts Rh and CoO_x . Reproduced with permission from Ref. 148. Copyright (2020) John Wiley and Sons.

4.4. Temperature-dependent solar water splitting

During the photocatalytic overall water splitting, the forward reaction of H_2 and O_2 evolution ($2H_2O \rightarrow 2H_2 + O_2$) often competes with the backward reaction of H_2 - O_2 recombination ($2H_2O \leftarrow 2H_2 + O_2$). Even though some cocatalysts (*i.e.*, Rh/ Cr_2O_3 core/shell nanoparticles¹⁵⁰) loaded on InGaN/GaN nanowires have promoted the forward reaction, the catalytic activity of III-nitride photocatalyst at higher temperatures has remained unknown. Therefore, photocatalytic water splitting was conducted at different temperatures from 30 °C to 80 °C by illuminating the

concentrated simulated solar light (3800 mW/cm^2).¹⁴⁹ InGaN/GaN nanowires decorated with Rh/Cr₂O₃/Co₃O₄ cocatalysts exhibited a dramatic increase in STH efficiency with increasing temperature (Fig. 17a). The maximum STH efficiency of 8.8% was achieved at 70 °C. Theoretical calculation elucidated that most steps of water splitting reactions were exothermal except for the water desorption step in the H₂-O₂ recombination, meaning that the H₂-O₂ recombination is suppressed as the temperature increases. However, further increasing the temperature to 80 °C did not improve the STH efficiency because the enhanced diffusivity of H₂ and O₂ promoted the mass transfer in water and accelerated the H₂-O₂ recombination. The Rh/Cr₂O₃/Co₃O₄-InGaN/GaN photocatalyst showed a world-record STH efficiency of 9.2% and promising stability for 74 hours at the optimized temperature of 70 °C (Fig. 17b). Moreover, the photocatalysts, evaluated in tap water (Fig. 17c) and seawater, exhibited very high STH efficiency of 7.4% and 6.6%, respectively, showing high potential for practical use. In principle, it is possible to reduce material costs when more solar energy can be utilized in a given irradiated area. Hence, a 4 cm × 4 cm photocatalyst wafer was immersed in water and exposed to the concentrated natural solar light ($\sim 16,070 \text{ mW/cm}^2$). This outdoor test showed that the chamber could be self-heated and maintained at a high temperature ($75 \pm 3 \text{ °C}$). As a result, the highest reported STH efficiency of 6.2% was achieved under natural solar light (Fig. 17d). This work is the first demonstration that the III-nitride photocatalyst not only utilizes the ultraviolet-visible light for photoexcitation of charge carriers but also benefits from thermal energy generated by infrared light (Fig. 17e).

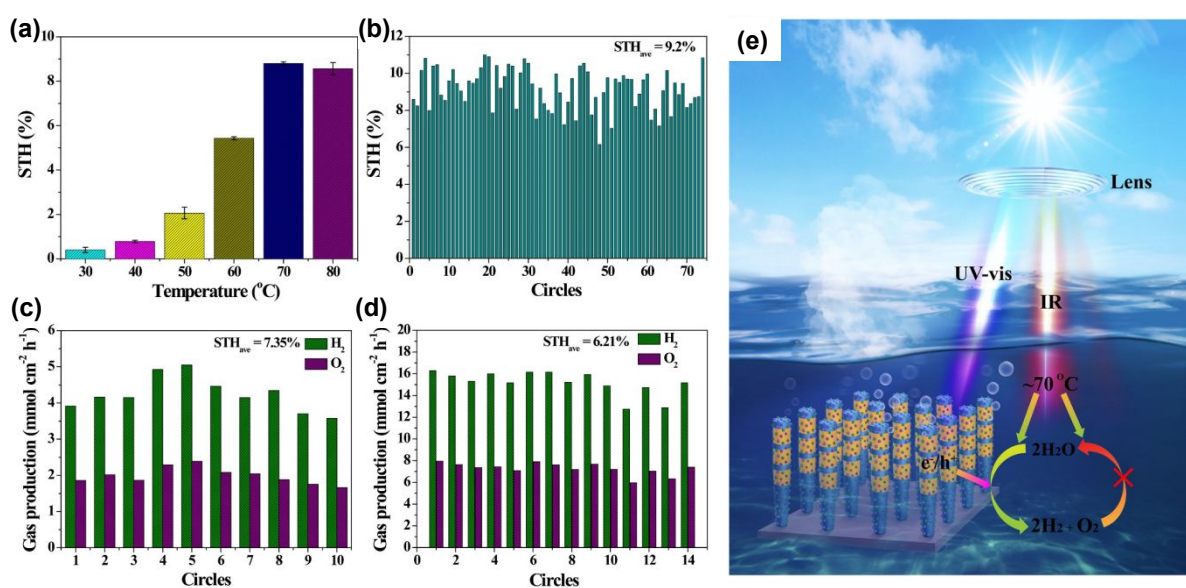


Fig. 17. (a) Temperature-dependent STH efficiency of Rh/Cr₂O₃/Co₃O₄-InGaN/GaN nanowires. A concentrated light of 3800 mW/cm² with AM 1.5 G filter was used. (b) Stability in the self-heated photocatalytic overall water splitting system. Each circle: 1 hour. (c) Measured STH in tap water under 3800 mW/cm². Each circle: 1 hour. (d) STH of 4 cm × 4 cm photocatalyst under concentrated natural solar light (~16,070 mW/cm²). Each circle: 10 min. (e) Synergetic effect mechanism of promoting forward H₂-O₂ evolution and inhibiting the reverse H₂-O₂ recombination in the photocatalytic overall water splitting. Reproduced with permission from Ref. 149. Copyright (2023) Springer Nature Limited.

5. Photoelectrochemical CO₂ reduction

Photosynthesis is widely known as the biochemical reaction which fixes CO₂ gas in the atmosphere into carbon-based species under solar light. This solar-driven biochemical process can be mimicked by semiconductors where the photogenerated charge carriers under solar light transport to the surface, interact with CO₂ molecules, and catalytically convert the activated CO₂ molecules into other carbon products through deoxygenation and/or hydrogenation processes. Compared to the electrocatalytic CO₂ reduction reaction, whose efficiency is determined by the catalytic activity of the electrocatalyst, light absorption, electron-hole separation, charge carrier transport, and band alignment must be additionally considered to design an artificial photosynthetic device. Although these challenging requirements have limited the number of semiconductors, careful selection of semiconductors and catalyst materials, and optimization of device structures have realized CO₂ reduction reaction.^{154, 155, 156, 157, 158, 159, 160, 161, 162, 163, 164, 165, 166, 167} Recently, 1D nanostructured semiconductor nanowires, nanorods, and nanofibers have surpassed the CO₂ reduction reactivity of planar structures due to enhanced light absorption, shortened charge carrier pathways, and exposure of active sites.^{168, 169, 170, 171, 172, 173, 174, 175} Especially, the emerging 1D nitrides have shown great promise for efficient and stable conversion of CO₂ gas into target products.

Photoelectrochemical CO₂ reduction reaction can convert the greenhouse CO₂ gas to value-added chemicals by simultaneously illuminating solar light and applying an electrical bias to semiconductor photocathodes. Despite the light absorption, charge carrier excitation, separation, and transport processes of photoelectrochemical CO₂ reduction reaction being very similar to photoelectrochemical hydrogen evolution reaction, the CO₂ reduction reaction is much more complex due to the many possible reaction pathways coming from different

reaction intermediates. Depending on the binding modes of intermediates on the surface of electrodes, the selectivity and productivity of target chemicals can be changed. For example, an intermediate produced by CO₂ accepting an electron and a proton could be *COOH with C attached to the surface or *OCHO with O attached to the electrode. The different intermediates play a vital role in determining the final products (*i.e.*, CO, HCOOH, CH₄, C₂H₄, C₂H₅OH, etc.). III-nitride semiconductors, however, do not possess good catalytic activity toward CO₂ reduction reaction likely due to unfavorable CO₂ adsorption in comparison to proton reduction reaction which can be operated with pristine GaN photocathode. This bottleneck has been addressed by adapting appropriate cocatalysts on III-nitride photocathodes for the selective production of target chemicals such as carbon monoxide (CO), formic acid (HCOOH), and methane (CH₄) (Table 4).

Table 4. III-nitride photocathodes for photoelectrochemical CO₂ reduction reaction.

Photocathodes	Cocatalysts	Applied potential	CO ₂ feedstock	Main products	Faradaic efficiency	Current density	Ref.
p-GaN film	Au	-1.8 V _{RHE}	Pure CO ₂	CO	CO: 83%	~2 μA/cm ²	176
GaN nanowires /n ⁺ -p Si	ZnO-Cu	0.17 V _{RHE}	Pure CO ₂	CO	CO: 70%	< 1 mA/cm ² (8 sun light)	177
GaN nanowires /n ⁺ -p Si	TiO ₂ -Pt	0.27 V _{RHE}	Pure CO ₂	CO, H ₂	CO: ~33%, H ₂ :~66%	~15 mA/cm ² (8 sun light)	178
GaN nanowires /n ⁺ -p Si	AuPt _{0.2}	0.17 V _{RHE}	Pure CO ₂	CO, H ₂	CO: ~33%, H ₂ :~66%	~9 mA/cm ²	179
GaN nanowires /n ⁺ -p Si	Au	0.17 V _{RHE}	Pure CO ₂	CO, H ₂	CO: ~55%, H ₂ :~45%	~3 mA/cm ²	180
GaN nanowires /n ⁺ -p Si	AgBr	-0.4 V _{RHE}	Pure CO ₂	CO	CO: 82%, H ₂ : 17%	13.8 mA/cm ²	181
GaN nanowires /n ⁺ -p Si	Sn	-0.53 V _{RHE}	Pure CO ₂	HCOOH	HCOOH: 76.9%	~11 mA/cm ²	182

GaN nanowires /n ⁺ -p Si	Bi	-0.6 V _{RHE}	Pure CO ₂	HCOOH	HCOOH: 95%	~10.3 mA/cm ²	183
GaN nanowires /n ⁺ -p Si	Cu	-1.5 V _{Ag/AgCl}	Pure CO ₂	CH ₄	CH ₄ : 18%	~30 mA/cm ²	184
GaN nanowires /n ⁺ -p Si	Cu-Fe	-1.2 V _{RHE}	Pure CO ₂	CH ₄	CH ₄ : 51%	38.3 mA/cm ²	185
GaN nanowires /n ⁺ -p Si	CuS	-1.0 V _{RHE}	CO ₂ with H ₂ S	HCOOH	HCOOH: 70.2%	7.07 mA/cm ²	186
GaN nanowires /n ⁺ -p Si	Au	0.17 V _{RHE}	CO ₂ with NO _x , SO _x , or O ₂	CO	CO: ~90%	~4 mA/cm ²	187

5.1. CO production

Among the various products (*e.g.*, CO, HCOOH, CH₄, C₂H₄, CH₃OH, C₂H₅OH, etc.), that can be produced from CO₂ reduction reactions, CO and HCOOH are the kinetically most favorable products due to the simple two-proton-coupled electron transfer process. In addition, the reaction of synthetic gas (CO and H₂) can produce methanol and other important chemicals and fuels through the well-established Fischer-Tropsch method.^{188, 189} Therefore, III-nitride semiconductors decorated with cocatalysts have been investigated for the photoelectrochemical reduction of CO₂ gas to CO. The feasibility of Au cocatalyst has been evaluated on p-GaN film for CO₂ conversion to CO.¹⁷⁶ The p-GaN photocathode coated with Au nanoparticles showed an onset potential of about 0.4 V_{RHE}, a cathodic photocurrent density of 1.8 μA/cm² at -0.8 V_{RHE} (Fig. 18a), and CO-to-H₂ ratio of 5:1 at -1.8 V_{RHE} (Fig. 18b), whereas the bare p-GaN photocathode exhibited no photoresponse under visible-light illumination. The drastic improvement of photoresponse can be explained by a greater collection efficiency of hot holes from plasmonic Au nanoparticles to the valence band of p-GaN. Compared to the previous n-type semiconductors with good hot electron collection properties (Fig. 18c), the Au/p-GaN interface can establish a more suitable Schottky barrier for hot hole collection (Fig. 18d). Thus, remaining hot electrons in Au nanoparticles can participate in the CO₂ reduction reaction. This implies the positive effect of downward band bending at the metal cocatalyst/semiconductor photocathode not only for the electron-hole separation but also for the efficient photoelectrochemical CO₂ reduction reaction.

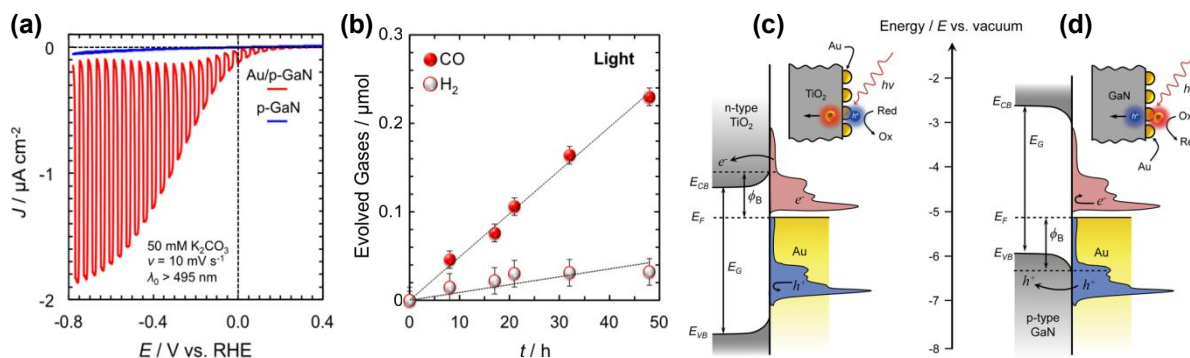


Fig. 18. (a) LSV of plasmonic Au/p-GaN and bare p-GaN photocathodes at 10 mV/s under periodic (0.5 Hz), visible-light irradiation ($\lambda > 495$ nm) at power of 600 mW/cm². (b) CO and H₂ evolution using Au/p-GaN photocathode. (c) Energy band diagrams of Au in physical contact with an n-type semiconductor (*e.g.*, TiO₂) and (b) with p-type semiconductor (*e.g.*, p-GaN) for hot electron and hot hole collection, respectively. Reproduced with permission from Ref. 176. Copyright (2018) American Chemical Society.

As it was mentioned in the previous section, the large band gap of GaN (~ 3.4 eV) cannot afford visible light absorption which limits the photocurrent density. In addition, planar GaN has a small specific surface area capable of holding a cocatalyst. To solve these problems, 1D GaN nanowires were vertically grown on the n⁺-p Si photocathode. Since the GaN nanowires have ~ 10 times larger surface area than the planar structure, a large number of cocatalysts can be loaded and the catalytic activity for the CO₂ reduction reaction can be greatly improved. In this configuration, the photoexcited charge carriers are mainly generated in the n⁺-p Si photocathode and the photogenerated electrons migrate to cocatalysts through n⁺-GaN nanowires. In order to concurrently facilitate electron transport and to promote catalytic performance, Cu-ZnO cocatalyst have been deposited on GaN nanowires (Fig. 19a).¹⁷⁷ The conduction band of ZnO locates below that of GaN, so the photogenerated electrons can migrate to surface Cu catalysts without a significant energy barrier (Fig. 19b). As a result, ZnO-Cu/GaN/n⁺-p Si photocathode attained a high photocurrent density (~ 10 mA/cm²) (Fig. 19c) and demonstrated a higher faradaic efficiency (FE) of CO (20%) at -0.33 V_{RHE} compared to control samples with ZnO (14.3%) and Cu (1.7%) cocatalysts (Fig. 19d). Inspired by this metal-oxide/metal cocatalyst loaded on GaN nanowires for CO production, TiO₂-Pt cocatalyst has been evaluated on GaN nanowires/n⁺-p Si photocathode and revealed a positive onset potential of ~ 0.5 V_{RHE} and ~ 2 times higher photocurrent density compared to photocathodes with TiO₂

or Pt cocatalysts (Fig. 19e).¹⁷⁸ FE of CO was low on pristine GaN/n⁺-p Si, and with individual TiO₂ and Pt cocatalysts (1.7%, 5.6%, and 2%, respectively), while it remarkably increased to 32% by employing TiO₂-Pt binary cocatalysts, indicating the synergetic interaction between Pt and TiO₂ for CO₂ reduction reaction (Fig. 19f). Furthermore, two metal-oxide/metal cocatalysts of ZnO-Pt and TiO₂-Pd exhibited higher CO selectivity compared to metallic Pt and Pd (Fig. 19g). To understand the mechanistic role of metal-oxide/metal interface for the CO₂ reduction to CO, density functional theory calculations were carried out (Fig. 19h). It was found that CO₂ is not activated on Pt cocatalyst but strongly interact with the TiO₂-Pt binary cocatalyst. The carbon atom of the CO₂ molecule at the interface binds to the metallic atom (Pt) and one of oxygen atoms attaches to the Ti atom of TiO₂. This interaction greatly stabilizes the CO₂ adsorption and facilitates the formation of *CO via *COOH intermediate, thereby resulting in a thermodynamically downhill process.

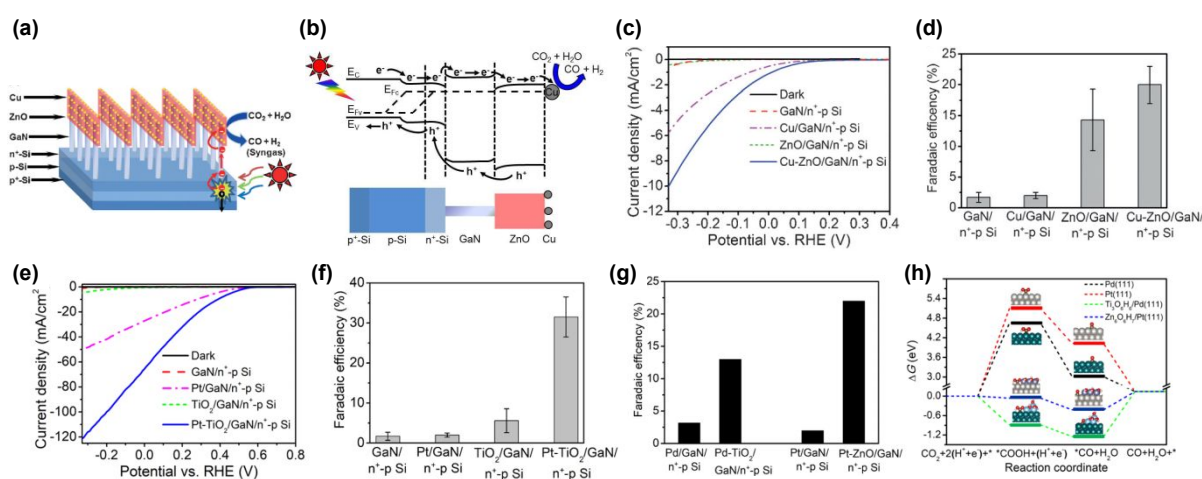


Fig. 19. (a) Schematic and (b) energy band diagram of Cu-ZnO/GaN/n⁺-p Si photocathode under light illumination. (c) LSV curves and (d) FE of CO at $-0.33 V_{RHE}$. Reproduced with permissions from Ref. 177. Copyright (2016) John Wiley and Sons. (e) LSV curves and (f) FE of CO for pristine GaN/Si and GaN/Si with Pt, TiO₂, and Pt-TiO₂ cocatalysts. (g) FE of CO at $0.27 V_{RHE}$ for GaN/Si photocathodes with Pd, Pd-TiO₂, Pt, and Pt-ZnO cocatalysts. (h) Calculated free energy diagrams for CO₂ reduction to CO. pine green, Pt: gray, Ti: blue, Zn: purple, O: red, C: brown and H: white. Reproduced with permissions from Ref. 178. Copyright (2018) American Chemical Society.

Despite the GaN nanowires/n⁺-p Si photocathode can increase the CO selectivity by metal-

oxide/metal cocatalysts, the true reactivity and role of GaN nanowires are largely unknown since the GaN surface covered by cocatalysts was not exposed to the electrolyte during the CO₂ reduction reaction. Therefore, Au and Pt cocatalysts have been directly coated on GaN nanowires without a metal oxide passivation layer.¹⁷⁹ Au nanoparticles were prepared on top of GaN nanowires by electron-beam evaporation method followed by thermal annealing and Pt nanoparticles were coated on the sidewalls of GaN nanowires by photodeposition method (Figs. 20a and 20b). These spatially separated Au and Pt cocatalysts preferentially convert CO₂-to-CO and H⁺-to-H₂, respectively. Control of the product distribution (*i.e.*, CO/H₂ syngas ratio) can be realized by tuning the composition ratio of Au and Pt cocatalysts. As the ratio of Pt increased in AuPt_x/GaN/n⁺-p Si, FE of H₂ gradually increased from ~10% to ~99% with decreased FE for CO from ~90% to nearly zero (Fig. 20c). By adjusting the cocatalyst composition on GaN nanowires, the syngas ratio of CO/H₂ could be varied in a wide range from 1:99 to 10:1. Furthermore, the size effect of Au nanoparticles was studied for syngas production on GaN/n⁺-p Si photocathode.¹⁸⁰ A gradual increase in CO selectivity with decreasing H₂ selectivity was observed with increasing particle size at 0.17 V_{RHE} under solar irradiation (Fig. 20d). As the size of Au nanoparticles with an icosahedral structure increases, the ratio of facet sites increases, and at the same time, the portion of edge and corner sites decreases (Fig. 20e). From the theoretical calculation, it was found that H₂ evolution, the major competitive reaction, becomes much easier on the corner and edge sites than facet sites (Fig. 20f). Therefore, the facet sites of large Au nanoparticles (16 nm) are responsible for the CO₂ reduction reaction into CO while dominant corner and edge sites of small Au nanoparticles (3 nm) are active for the H₂ evolution reaction.

In addition to crystal facet engineering, phase engineering of Ag and Ag halide cocatalysts have been modified on vertically grown GaN nanowires by photoelectrochemical anodization method (Fig. 20g).¹⁸¹ Compared to the metallic Ag nanoparticles, AgCl and AgBr cocatalysts greatly improved the selectivity and productivity of CO compared to H₂ (Fig. 20h). This indicates that fine-control of the material composition of cocatalysts can alter the surface electronic properties and consequent catalytic activity for CO₂ conversion. Moreover, the GaN/n⁺-p Si photocathodes with AgBr cocatalysts showed a very high photocurrent density of ~92 mA/cm² at -1.0 V_{RHE} under concentrated solar light (3 sun) (Fig. 20i). Stable and continuous production of CO could be achieved without losing the catalytic activity for 12 h.

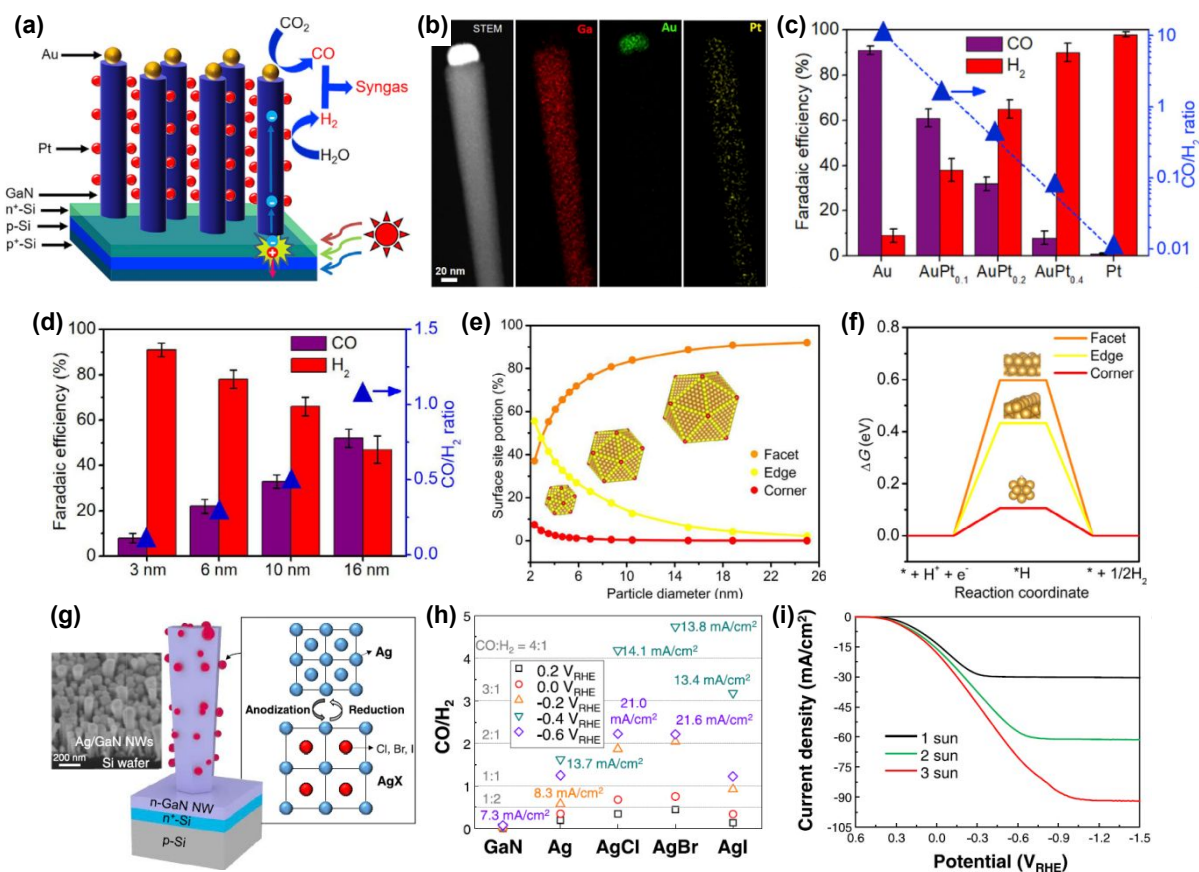


Fig. 20. (a) Schematic of AuPt_x/GaN/n⁺-p Si photocathode under light illumination. (b) STEM-energy dispersive X-ray spectroscopy elemental mapping images. (c) FE of CO and H₂ for AuPt_x/GaN/n⁺-p Si photocathodes at 0.17 V_{RHE}. Reproduced with permissions from Ref. 179. Copyright (2020) Elsevier. (d) Size dependence of photoelectrochemical CO₂ reduction performance on Au nanoparticles at 0.17 V_{RHE}. (e) Portion of surface sites on icosahedron Au nanoparticles vs. particle size. (f) Free energy diagram of proton reduction into H₂ on facet, edge, and corner sites of Au nanoparticles. Reproduced with permissions from Ref. 180. Copyright (2022) Elsevier. (g) SEM image of Ag-decorated GaN nanowires and schematic fabrication processes of Ag halides cocatalysts. (h) Plots of the CO/H₂ ratio for the photocathodes at different potentials from 0.2 to -0.6 V_{RHE}. (i) LSV curves of AgBr/GaN/Si under concentrated solar light. Reproduced with permissions from Ref. 181. Copyright (2022) American Chemical Society.

5.2. HCOOH production

HCOOH is an energy-dense liquid fuel and a building block for modern chemistry. There

have been extensive developments of metallic electrocatalysts such as Pb, Hg, Cd, Pd, In, Sn, and Bi for the selective conversion of CO₂ into HCOOH in aqueous electrolytes.^{190, 191, 192, 193, 194, 195, 196, 197, 198} However, the cost of expensive metals (Pd and In) and the toxicity of the heavy metals (Pb, Cd, Hg) are hindrances to practical application. Hence, environmentally benign metals of Sn, Bi, and their compounds have been spotlighted.^{199, 200, 201} Previously, Sn nanoparticles were electrochemically deposited on GaN nanowires grown on n⁺-p Si for photoelectrochemical CO₂ reduction reaction to HCOOH (Fig. 21a).¹⁸² Compared to the negligible productivity (2.1 μmol/cm²/h) of HCOOH on the Sn/n⁺-p Si photocathode, the productivity (201 μmol/cm²/h) of Sn/GaN/n⁺-p Si was nearly two orders of magnitude higher (Fig. 21b). This indicates that 1D GaN nanowires not only function as the support of cocatalysts and electron-migration channel but also participate in the CO₂ reduction reaction. Density functional theoretical calculation elucidated that CO₂ molecule can be easily activated and readily dissociated into *CO via a covalent-like Ga-C bond and an ionic-like Sn-O bond over the Sn/GaN interface, respectively (Fig. 21c). Then, the reduction of a key intermediate of CO* to HCOOH follows energetically favorable reaction pathway (Fig. 21d). It is of scientific interest to find that III-nitride integrated with cocatalyst results in beneficial synergy for CO₂ activation and HCOOH production.

Metallic Bi can also play a role as an efficient cocatalyst for photoelectrochemical CO₂-to-HCOOH conversion when it is integrated with GaN/n⁺-p Si electrode.¹⁸³ A simple one-step thermal evaporation of Bi cocatalysts on GaN nanowires induces uniformly distributed Bi/Bi₂O₃ nanoparticles (Fig. 21e). Noticeably, Bi/GaN/Si photocathode showed high FE of HCOOH > 95% at -0.3 V_{RHE} whereas Bi/Si exhibited low FE of HCOOH < 70% and relatively small photocurrent density (Fig. 21f). The reasons for the high HCOOH selectivity were the lowered catalytic energy barrier originated from Bi₂O₃/GaN interfacial interaction (Fig. 21g) and efficient transport of photogenerated electrons from GaN to Bi₂O₃ due to conduction band alignment (Fig. 21h). This work showed a promising insight that a strong electronic interaction between cocatalyst and 1D III-nitride can shift the intrinsic catalytic activity and realize a new class of material for efficient photoelectrochemical CO₂ reduction reaction.

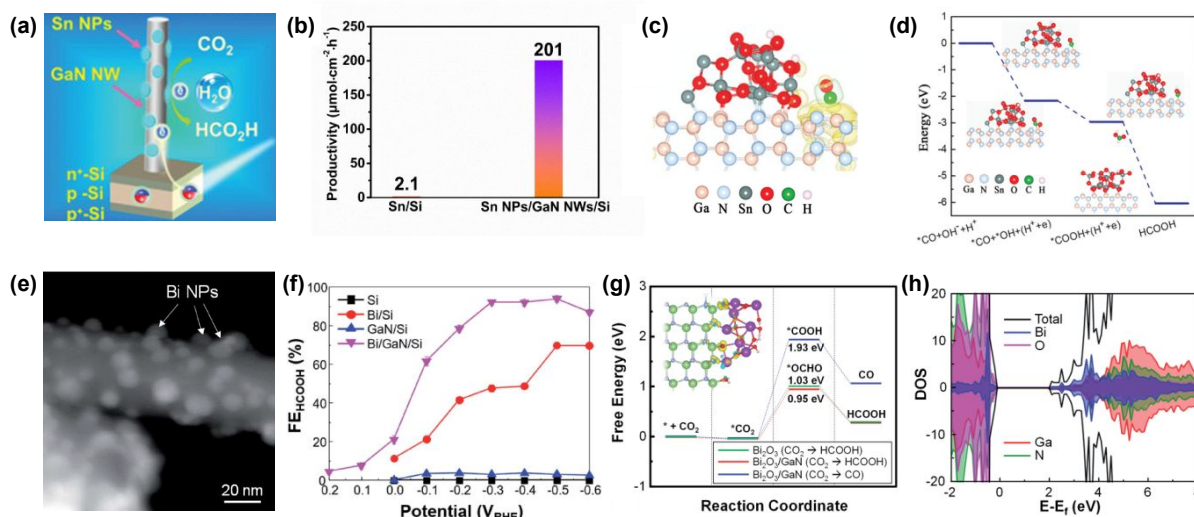


Fig. 21. (a) Schematic of Sn nanoparticles/GaN nanowires/ n^+ - p Si for photoelectrochemical CO_2 reduction with H_2O to HCOOH . (b) Productivity of HCOOH for Sn/Si and Sn/GaN/Si photocathodes. (c) Calculated differential charge density for the $^*\text{CO}/\text{Sn}_{13}\text{O}_{26}/\text{GaN}$. (d) Potential energy diagram of reducing CO_2 to HCOOH at the Sn/GaN interface. Reproduced with permissions from Ref. 182. Copyright (2019) Royal Society of Chemistry. (e) HAADF STEM image of Bi nanoparticles/GaN nanowires. (f) FE of HCOOH for photocathodes. (g) Free-energy profiles for CO_2 reduction reaction to HCOOH and CO on Bi_2O_3 and $\text{Bi}_2\text{O}_3/\text{GaN}$. (h) Density of states of $\text{Bi}_2\text{O}_3/\text{GaN}$ near the band gap. Reproduced with permissions from Ref. 183. Copyright (2022) Royal Society of Chemistry.

5.3. CH_4 production

Electrochemical production of CH_4 from CO_2 faces challenges of sluggish kinetics and competitive proton reduction reaction. Cu and its alloys are known to be state-of-the-art catalysts for converting CO_2 to high-order products.^{202, 203, 204} Therefore, Cu nanoparticles have been decorated on GaN/ n^+ - p Si for photoelectrochemical CO_2 reduction reaction to CH_4 .¹⁸⁴ A little amount of CO was produced on pristine GaN nanowires and CH_4 product was not detected by gas chromatographic measurement (Figs. 22a and 22b). In stark contrast, Cu cocatalysts on both GaN/ n^+ - p Si and n^+ - p Si boosted the photocurrent density, positively shifted onset potential, and increased the FE of CH_4 . More interestingly, the Cu cocatalysts loaded on GaN nanowires showed higher selectivity of CH_4 ($\sim 18\%$) than the ones on the Si photoelectrode ($\sim 4\%$). To enhance the catalytic activity of photocathode, binary Cu-Fe cocatalysts have been developed on GaN/ n^+ - p Si.¹⁸⁵ From the theoretical calculation, it was found that Cu and Fe

binary catalyst activates the inert CO_2 molecule by bending the O-C-O angle from 180° to 126.05° and by elongating the C-O bond length (Figs. 22c and 22d). The thermodynamic energy barrier of the potential-determining step (*i.e.*, $^*\text{CO} \rightarrow ^*\text{CHO}$) for CO_2 -to- CH_4 conversion was reduced from 0.85 to 0.51 eV by incorporating Fe into Cu catalysts (Fig. 22e). The binary Cu-Fe showed better onset potential, higher photocurrent density compared to single Cu or Fe catalysts on GaN/ n^+ -p Si. Moreover, FE of CH_4 increased up to 51%, which is superior to that of Cu cocatalyst ($\sim 19\%$) under the identical measurement conditions (Fig. 22f). Rational design of cocatalysts and 1D nitrides having high catalytic activity for CO_2 -to- CH_4 conversion is found to be essential for the efficient and selective photoelectrochemical synthesis of high-order products such as CH_4 .

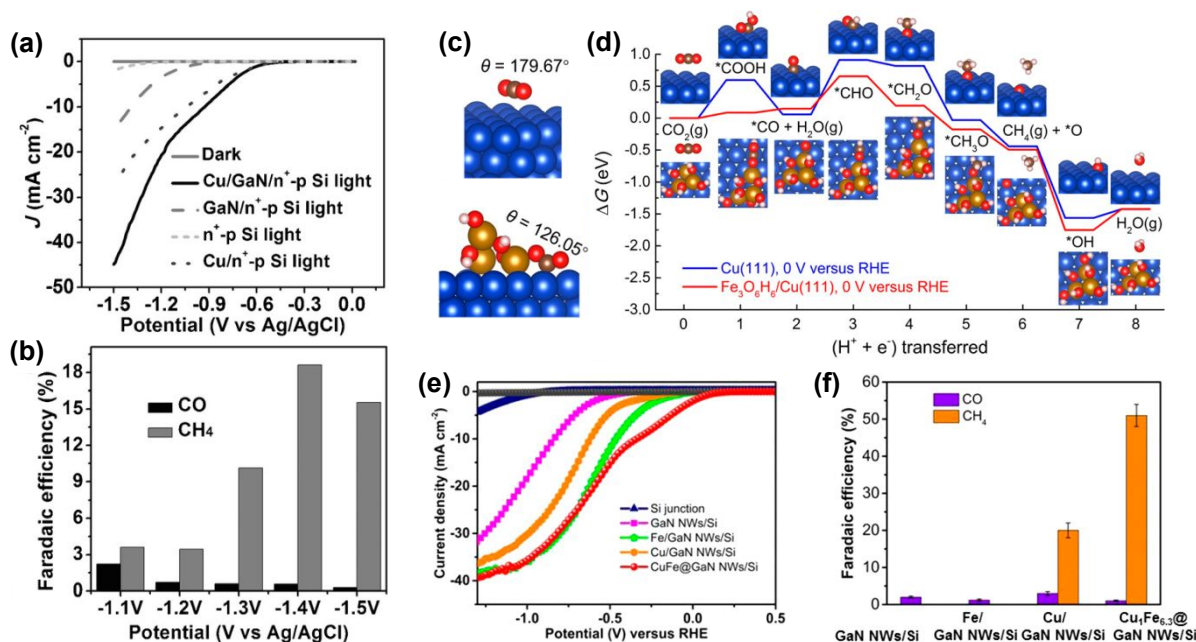


Fig. 22. (a) LSV curves of n^+ -p Si and GaN nanowires/ n^+ -p Si photocathodes with/without Cu cocatalysts. (b) FE of CO and CH_4 produced from Cu/GaN/Si photocathode. Reproduced with permissions from Ref. 184. Copyright (2016) John Wiley and Sons. (c) The optimized configurations of CO_2 molecule on Cu (111) and $\text{Fe}_3\text{O}_6\text{H}_6/\text{Cu}(111)$. Blue, orange, red, brown, and white spheres represent Cu, Fe, O, C, and H atoms, respectively. (d) Free-energy diagrams for CO_2 reduction to CH_4 on Cu and $\text{Fe}_3\text{O}_6\text{H}_6/\text{Cu}$ interface. (e) LSV curves and (f) FE of CO and CH_4 for GaN/Si photocathodes with Fe, Cu, and Cu-Fe cocatalysts. Reproduced with permissions from Ref. 185. Copyright (2020) National Academy of Science.

5.4. Flue gas CO₂ reduction

Until now, most studies have focused on the development of photocathodes using pure CO₂ feedstock. However, for practical application, their compatibility with flue gas CO₂ should be considered. Flue gas CO₂ usually contains many impurities such as H₂, CO, NO_x, SO_x, and H₂S compounds. Hence, it is of great interest to convert impurity-containing flue gas CO₂ into value-added chemicals without a costly purification process.^{205,206,207} Recently, a photocathode consisting of CuS cocatalyst loaded on GaN nanowires/n⁺-p Si has been presented as a promising architecture for efficient and stable conversion of H₂S-containing CO₂ mixture gas to HCOOH.¹⁸⁶ Cu nanoparticles were firstly deposited on GaN nanowires and then spontaneously transformed to CuS nanoparticles by H₂S impurity dissolved in the electrolyte during the CO₂ reduction reaction (Fig. 23a). After the photoelectrochemical CO₂ reduction reaction, CuS compounds can be clearly seen on GaN nanowires (Fig. 23b). In order to evaluate to Cu and CuS cocatalysts on photocathodes, photoelectrochemical CO₂ reduction reaction was conducted in CO₂- or CO₂+H₂S-purged electrolyte, respectively. Cu and CuS cocatalysts integrated with GaN nanowires grown on n⁺-p Si (GaN/Si) showed a substantial improvement in onset potential and photocurrent density compared to those of Cu/Si, and CuS/Si (Fig. 23c). The increase in the selectivity of HCOOH was observed from ~21% to ~32% when Cu cocatalysts were converted to CuS on n⁺-p Si photocathode at -1.0 V_{RHE} (Fig. 23d). Impressively, the transformation of Cu to CuS nanoparticle on GaN nanowires greatly increased the FE of HCOOH from ~20% to ~70% at the same conditions. This demonstrates that H₂S impurity mixed in the CO₂ gas can enhance, rather than degrade, the performance of the photoelectrochemical CO₂ reduction reaction. CuS/GaN/Si revealed constant photocurrent densities of ~4.5 and ~7.8 mA/cm² and consistently produced high FE of ~60% and ~70% at -0.8 and -1.0 V_{RHE}, respectively (Fig. 23e). This outstanding stability is likely due to the chemical stability of unique N-rich GaN surface which can withstand oxidation or sulfurization by impurity in the flue gas CO₂.

The influence of various impurities (0.1% NO_x, 1% SO_x, and 5% O₂) on photoelectrochemical CO₂ reduction performance was also tested using Au nanoparticles deposited on top of GaN nanowire arrays on n⁺-p Si (Fig. 23f).¹⁸⁷ The effects of NO_x and SO_x on CO₂ reduction reaction to CO were negligible (Fig. 23g). In contrast, the presence of O₂ impurity decreased the FE of CO from 90% to 68% due to more favorable O₂ reduction reaction. Although the O₂ impurity led to a temporary decrease of FE of CO, it can be fully recovered

when a pure CO_2 feedstock was purged, indicating a negligible long-term impact of O_2 on the photocathodes (Fig. 23h). From these results, it was found that 1D GaN nanowires are chemically stable against impurity gases mixed in flue gas CO_2 and function as good photocathode platform for the CO_2 reduction reaction.

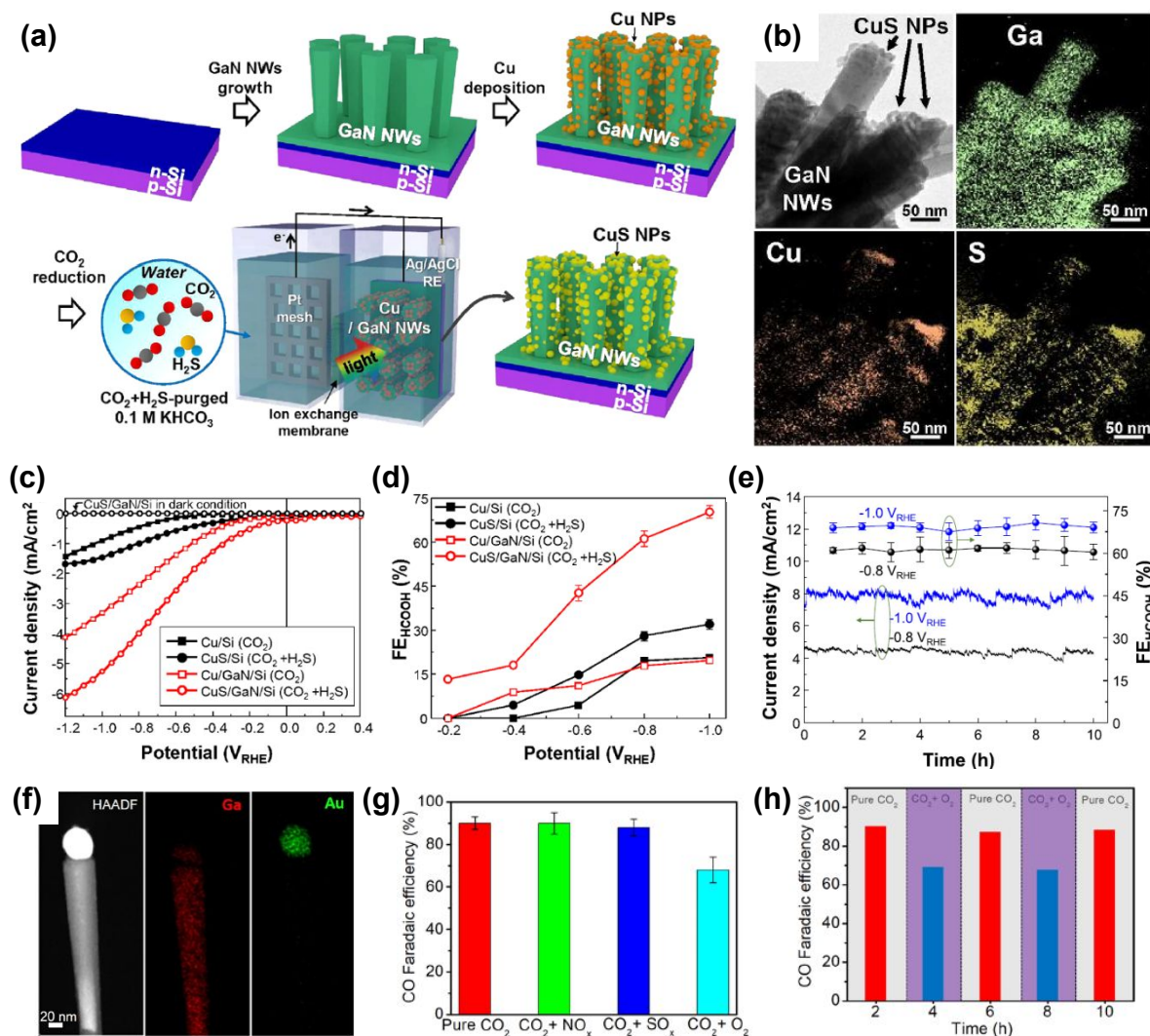


Fig. 23. (a) Schematic fabrication process of CuS/GaN/Si by MBE growth of GaN nanowires on n^+p Si, electron-beam deposition of Cu nanoparticles, and spontaneous transformation of Cu to CuS cocatalysts. (b) TEM analysis of CuS nanoparticles on GaN nanowires. (c) LSV curves and (d) FE of HCOOH for photocathodes measured in CO_2 - or $\text{CO}_2+\text{H}_2\text{S}$ -purged electrolytes. (e) Stability of CuS/GaN/Si photocathode at -0.8 and -1.0 V_{RHE} . Reproduced with permissions from Ref. 186. Copyright (2021) American Chemical Society. (f) Structural characterization of Au/GaN/Si. (g) FE of CO at 0.17 V_{RHE} measured with impurities of NO_x ,

SO_x, and O₂ mixed in CO₂ gas. (h) Time-dependent CO FE with or without O₂ impurity gas. Reproduced with permissions from Ref. 187. Copyright (2022) Elsevier.

6. Photocatalytic CO₂ reduction reaction

1D III-nitrides photocathodes can drive a half-reaction of the CO₂ reduction reaction and the other oxidation reaction takes a place at the counter electrode. In contrast, both CO₂ reduction and oxidation reactions occur at the surface of 1D III-nitrides photocatalysts during photocatalytic reaction. During photocatalytic CO₂ reduction, intermediates on the surface can be reduced or simultaneously oxidized to produce a variety of chemical products that are rarely obtainable with cathodic half-reaction alone. In addition to the requirements of the conventional photocatalysts (*i.e.*, band edge positions, charge carrier separation, and transportation), the kinetic balance between CO₂ reduction and oxidation reaction is mandatory for the selective production of target chemicals. Because GaN nanowires fulfill the requirements of band edge positions (the conduction band positions higher than the reductive potential of CO₂ reduction and the valance band locates lower than the oxidation reaction) (Fig. 24a), 1D III-nitrides are desirable platforms for photocatalytic CO₂ reduction reaction as demonstrated by several experiments (Table 5). In addition, GaN nanowires can readily activate the adsorbed CO₂ by bending the linear O-C-O bonds, thereby resulting in the effective CO₂ reduction reaction toward CO even without a cocatalyst (Fig. 24b).²⁰⁸ However, pristine GaN nanowires cannot efficiently produce CH₄ since the CO₂-to-CH₄ conversion is kinetically and thermodynamically unfavorable because of the high reaction barrier and complicated 8H⁺/8e⁻ process. This limitation can be overcome by employing Rh/Cr₂O₃ cocatalysts on the GaN nanowires. When the CO₂ reduction reaction was carried by vaporized water and CO₂ gas under concentrated solar light, the production rate and selectivity of CH₄ were enormously improved by suppressing competing CO evolution reaction (Fig. 24c). Pt cocatalyst exhibited a further increase in the production rate of CH₄ (Fig. 24d), which is 4.2 times higher than that of Rh/Cr₂O₃, indicating once again that rational design of cocatalysts on 1D nitrides can drastically boost the productivity of target chemicals.

InGaN nanowires with narrower band gap energy can broaden the wavelength of light absorption and enhance the production rate compared to GaN nanowires. Hence, p-InGaN/GaN nanowires were grown on Si substrate with the decoration of Pt nanoparticles cocatalysts for photocatalytic CO₂ conversion reaction (Fig. 24e).²⁰⁹ Photoluminescence spectroscopy

measurement identified that the p-InGaN/GaN nanowires photocatalyst is capable of harvesting visible light (< 533 nm) (Fig. 24f). The photocatalyst achieved a conversion rate of CO_2 into CH_3OH (~ 0.5 mmol/g_{cat}/h) under visible light illumination (> 400 nm). Moreover, the role of dopants in the photocatalytic CO_2 reduction reaction was investigated (Fig. 24g). Mg-doped InGaN nanowires presented much higher CO , CH_4 , and CH_3OH production rates than the undoped and Ge-doped InGaN nanowires (Figs. 24h and 24i) because of the reduced surface potential barriers by downward band bending as well as the activation of CO_2 molecule (Fig. 24j). The mechanistic understanding on the origins for the enhanced photocatalytic activities provides insights on the important function of dopants and surface band bending of III-nitrides.

Table 5. III-nitride photocatalysts for photocatalytic CO_2 conversion reaction.

Photocatalysts	Cocatalysts	Reactant	Light source	Performance	Ref.
GaN NWs	Pt	CO_2 + vaporized H_2O	300 W Xe lamp	$\text{CH}_4 \sim 14.8$ $\mu\text{mol/g}_{\text{cat}}/\text{h}$	208
p-InGaN/GaN NWs	Pt	CO_2 + H_2 + vaporized H_2O	300 W Xe lamp with 400 nm long-pass filter	$\text{CH}_3\text{OH} \sim 0.5$ mmol/g _{cat} /h	209
InGaN/GaN NWs	Au@Cr ₂ O ₃	CO_2 + vaporized H_2O	300 W Xe lamp	Syngas of 1.08 mol/g _{cat} /h	210

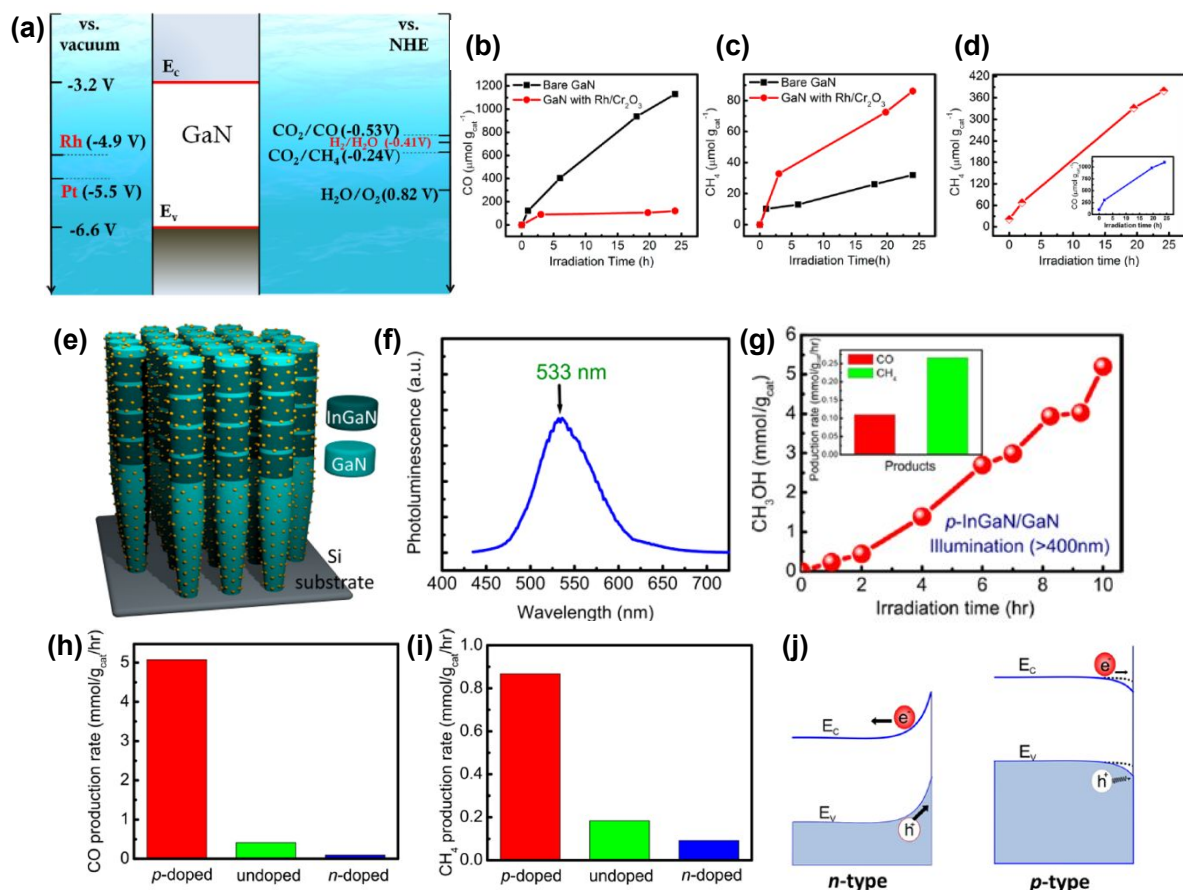


Fig. 24. (a) Band edge positions of GaN in comparison with the work function of Rh and Pt. CO_2/CO and CO_2/CH_4 reduction potentials vs. normal hydrogen electrode for $\text{pH} = 7$ are shown together. Photocatalytic CO_2 reduction reaction to (b) CO and (c) CH_4 by Rh/ Cr_2O_3 cocatalysts. (d) CH_4 evolution over Pt-decorated GaN nanowires and the inset shows CO generation. Reproduced with permissions from Ref. 208. Copyright (2015) American Chemical Society. (e) Schematic of p-InGaN/GaN nanowire photocatalysts decorated with Pt nanoparticles. (f) Photoluminescence spectrum of InGaN/GaN photocatalysts. (g) CH_3OH evolution over Pt-decorated p-InGaN/GaN nanowires under visible light illumination ($> 400 \text{ nm}$). The inset shows production rates of CO and CH_4 . Doping-type-dependent production rate of (h) CO and (i) CH_4 of InGaN/GaN nanowires. (j) Schematic of charge carrier transfer illustrated on n- (p-) doped semiconductors with upward (downward) surface band bending. Reproduced with permissions from Ref. 209. Copyright (2016) American Chemical Society.

Recently, $\text{Au}/\text{Cr}_2\text{O}_3$ core/shell nanoparticles cocatalysts have shown promising photocatalytic CO_2 -to-CO conversion reactivity on 1D InGaN/GaN nanowires (Fig. 25a).²¹⁰

Under the solar irradiation, CO_2 and H_2O reactants were effectively converted to CO and H_2 syngas with a production rate of $1.08 \text{ mol/g}_{\text{cat}}/\text{h}$ and a ratio of 1:1.6 (Fig. 25b). $\text{Au}/\text{Cr}_2\text{O}_3$ cocatalysts significantly outperform the single component cocatalysts of Au and Cr_2O_3 , evidencing the synergistic interaction between Au and Cr_2O_3 for photocatalytic reactions. Density functional calculation revealed that the CO_2 molecule barely interacts with Au and Cr_2O_3 surface while it is easily activated by bending the O-C-O angle to 116.5° on $\text{Au}/\text{Cr}_2\text{O}_3$, thus significantly reducing the reaction energy barrier (Fig. 25c). In addition, the energy barrier for H_2 evolution reaction was also the lowest on the $\text{Au}/\text{Cr}_2\text{O}_3$ interface, exhibiting high catalytic activity for both CO and H_2 evolution reactions and thus syngas synthesis (Figs. 25d and 25e).

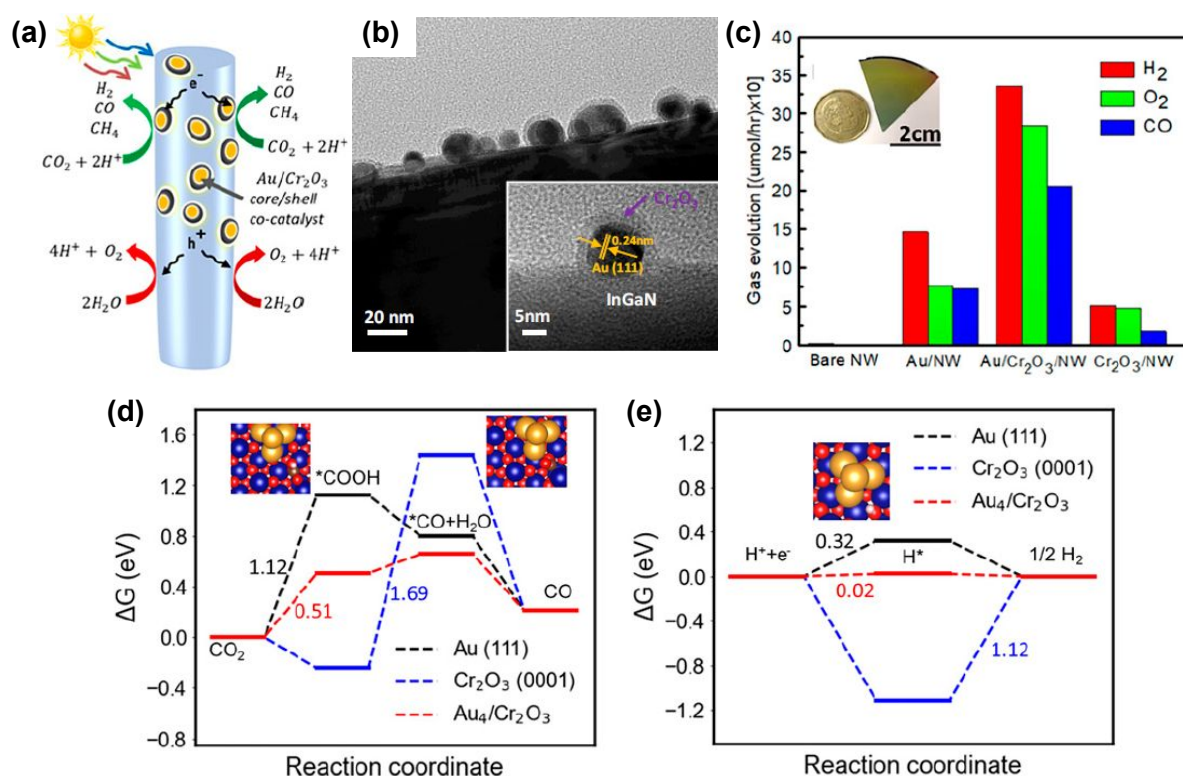


Fig. 25. (a) Schematic illustration of photocatalytic overall CO_2 reduction reaction over $\text{Au}/\text{Cr}_2\text{O}_3$ -decorated InGaN/GaN nanowires. (b) Structural analysis of $\text{Au}/\text{Cr}_2\text{O}_3$ core/shell cocatalysts on InGaN/GaN nanowires. (c) The output gas evolution with various cocatalysts. Calculated free energy diagrams for (d) CO_2 reduction reaction and (e) H_2 evolution reaction on different photocatalysts. Au, gold; Cr, blue; C, brown; and O, red. Reproduced with permission from Ref. 210. Copyright (2022) National Academy of Science.

7. Challenges, Prospects, and Conclusions

III-nitrides, e.g., InGaN, have tunable band gap energy and ideal band edge positions for water splitting and CO₂ reduction. Moreover, the emerging 1D III-nitride nanostructures have greatly improved the performance of photoelectrodes and photocatalysts compared to the planar structure. In this review, we describe the fabrication methods of 1D III-nitrides and their application to photoelectrochemical and photocatalytic water splitting and CO₂ reduction reactions, along with efficiency-enhancement strategies. There have been key challenges of artificial photosynthesis such as 1) low optical absorption, 2) severe electron-hole recombination, 3) poor catalytic activity, and 4) poor stability. Thus, tuning of band gap energy for broadband light absorption is a primary concern to achieve a high yield of target products. In this context, indium incorporation into GaN nanowires and heterogeneous tandem stacking of dual- or triple-band III-nitrides have been demonstrated. Preventing the recombination of photogenerated electrons and holes is another critical issue for the efficient utilization of charge carriers. Therefore, electrical conductivity, surface band bending, and charge carrier transport properties have been finely controlled by n- or p-type doping of III-nitrides. The intrinsic catalytic activity and selectivity of III-nitrides could be enhanced by the decoration of extrinsic cocatalysts, which sometimes show unprecedented synergy at the interface at III-nitride/cocatalyst and realize unique catalytic performance for water splitting and CO₂ reduction reaction. Moreover, N-terminated top and lateral surfaces of GaN nanowires showed record-high stability over 3000 h for photoelectrochemical water splitting under solar light irradiation. Recent studies identified that the partial substitution of nitrogen by oxygen on the nonpolar lateral surface of GaN nanowire not only improves the catalytic activity for the H₂ evolution reaction but also is responsible for the excellent stability against harsh reaction conditions.

Nevertheless, the state-of-the-art growth methods of high crystal-quality III-nitrides are limited to wafer-scale fabrication techniques (e.g., MBE or MOCVD), which may pose limitations on the large-scale application of photocatalysts or photoelectrodes. Recent studies, however, found that the concentrated solar light irradiation on wafer-scale 1D III-nitrides drastically improves the photocatalytic activity, which outperforms the photocatalyst particles dispersed in the solution.¹⁴⁹ Hence, the utilization of thermal energy obtained from phonon vibration or non-radiative recombination under concentrated sunlight has been attracting

attention. The thermal energy generally degrades the optoelectronic properties of semiconductors but promotes the chemical reactions by providing additional energy to overcome the activation barriers. Considering these trade-offs, the rational design of III-nitrides and the careful utilization of the photoexcited charge carriers with photoinduced thermal energy will represent a significant opportunity. In addition, fast reaction kinetics under concentrated solar light will lead to a vigorous generation of products and consumption of reactants near the electrode, which changes the local reaction environment and affects catalytic activity and stability. The local shift in reaction condition near the III-nitrides may oxidize the specific crystal planes, leading to new composites on the surface. The understanding of the material, optoelectronic, and catalytic properties of the reconstructed surface compounds will guide us to design more efficient and stable III-nitrides devices. Gas bubbles generated in the solution have a physical force to remove 1D III-nitrides from the substrate by surface tension. When the reaction rate increases under concentrated sunlight, the physical stability will become a more severe issue, and a strategy to anchor 1D nitride nanostructures on supports will be required. The stability of the photo(electro)catalyst is also largely dependent on the stability of the cocatalyst, and the separation of the cocatalyst from III-nitrides during the reaction has been a major reason for degradation. In general, since metallic nanoclusters or single atom catalysts tend to be stably located in the N-vacancy of the nitride materials,²¹¹ the method of forming the N-vacancy and sub-nanometer cocatalysts on the surface of the III-nitride semiconductors as well as catalytic activity should be studied to hold the cocatalysts on the surface and to maintain high efficiency. To date, the growth of high crystal-quality 1D III-nitrides has been limited to few types of substrates due to lattice mismatch and high-temperature computability of the substrate. Overcoming challenges in the growth method could potentially solve the efficiency bottleneck by integrating 1D III-nitrides with other highly efficient semiconductors (*e.g.*, I I I - V semiconductors).

The fact that 1D III-nitrides are efficient and stable materials for water splitting and CO₂ reduction reactions implies that these nanostructured semiconductors can also be used for various other chemical reactions, including ammonia (NH₃) synthesis, methane (CH₄) oxidation, and urea synthesis. Recently, studies related to the conversion of N₂ or NO₃⁻ into NH₃ in an aqueous solution are attracting great attention in order to replace the conventional energy-intensive and CO₂-emissive synthetic process. However, the initial activation of these

reactants is extremely difficult due to the difficulties of $\text{N}\equiv\text{N}$ bond or $\text{N}=\text{O}$ bond cleavage. This problem could be resolved if 1D III-nitrides with an appropriate amount of N-vacancies, that readily interact with N-containing reactants to activate and promote the catalytic reaction, are realized.²¹² Moreover, unique metal-support interactions, found in the cocatalyst- III-nitride system, will broaden the application of 1D III-nitrides to solar-driven CH_4 oxidation. Several promising results of CH_4 oxidation to CH_3OH ²¹³ and benzene production²¹⁴ via C-C coupling have been reported using 1D III-nitride artificial photosynthetic devices. Therefore, III-nitrides hold great potential for many solar-powered catalytic reactions by enhanced $\text{N}\equiv\text{N}$ and $\text{N}=\text{O}$ bond cleavage, C-H bond activation, C-C and C-N coupling reaction, and aromatization.

In summary, various physical/chemical studies on 1D III-nitride semiconductors have led to the successful demonstration of artificial photosynthetic devices. A deeper understanding of the mechanism at the atomic scale with the assistance of experimental evaluation, catalyst characterization, operando analysis, advanced molecular dynamics and first-principal density functional calculations will further provide fundamental guidelines on the rational design of the device. In the near future, researches on III-nitrides, which can operate in extreme environments (*i.e.*, high temperature, concentrated solar light, etc.), will be required to increase yield as well as efficiency and stability. Finally, since III-nitride is one of the most used semiconductor materials in the industry, commercialization is expected to be easier than other competing materials if the III-nitride artificial photosynthesis device achieves an appropriate level of efficiency and lifetime.

Conflicts of interest

Some IP related to this work was licensed to NS Nanotech, Inc. and NX Fuels, Inc., which were co-founded by Z. Mi. The University of Michigan and Mi have a financial interest in NS Nanotech.

Acknowledgements

This work was supported by United States Army Research Office Award W911NF2110337.

References

1. J. A. Turner, *Science*, 2004, **305**, 972-974.
2. S. Chu and A. Majumdar, *nature*, 2012, **488**, 294-303.

3. O. S. Bushuyev, P. De Luna, C. T. Dinh, L. Tao, G. Saur, J. van de Lagemaat, S. O. Kelley and E. H. Sargent, *Joule*, 2018, **2**, 825-832.
4. I. Sullivan, A. Goryachev, I. A. Digdaya, X. Li, H. A. Atwater, D. A. Vermaas and C. Xiang, *Nature Catalysis*, 2021, **4**, 952-958.
5. M. G. Walter, E. L. Warren, J. R. McKone, S. W. Boettcher, Q. Mi, E. A. Santori and N. S. Lewis, *Chemical reviews*, 2010, **110**, 6446-6473.
6. Y. Tachibana, L. Vayssieres and J. R. Durrant, *Nature Photonics*, 2012, **6**, 511-518.
7. Y. He, T. Hamann and D. Wang, *Chemical Society Reviews*, 2019, **48**, 2182-2215.
8. X. Li, J. Yu, M. Jaroniec and X. Chen, *Chemical reviews*, 2019, **119**, 3962-4179.
9. C. E. Creissen and M. Fontecave, *Advanced Energy Materials*, 2021, **11**, 2002652.
10. Y. Xia, P. Yang, Y. Sun, Y. Wu, B. Mayers, B. Gates, Y. Yin, F. Kim and H. Yan, *Advanced materials*, 2003, **15**, 353-389.
11. S. Barth, F. Hernandez-Ramirez, J. D. Holmes and A. Romano-Rodriguez, *Progress in Materials Science*, 2010, **55**, 563-627.
12. M. Meng, L. Wang, C. Li, K. Xu, Y. Chen, J. Li, Z. Gan, H. Yuan, L. Liu and J. Li, *Applied Catalysis B: Environmental*, 2023, **321**, 122071.
13. W. J. Dong, C. J. Yoo, H. W. Cho, K. B. Kim, M. Kim and J. L. Lee, *Small*, 2015, **11**, 1947-1953.
14. E. Garnett and P. Yang, *Nano letters*, 2010, **10**, 1082-1087.
15. D. A. Wheeler, G. Wang, Y. Ling, Y. Li and J. Z. Zhang, *Energy & Environmental Science*, 2012, **5**, 6682-6702.
16. F. X. Xiao, J. Miao, H. B. Tao, S. F. Hung, H. Y. Wang, H. B. Yang, J. Chen, R. Chen and B. Liu, *Small*, 2015, **11**, 2115-2131.
17. J.-W. Lee, K.-H. Cho, J.-S. Yoon, Y.-M. Kim and Y.-M. Sung, *Journal of Materials Chemistry A*, 2021, **9**, 21576-21606.
18. B. Weng, S. Liu, Z.-R. Tang and Y.-J. Xu, *Rsc Advances*, 2014, **4**, 12685-12700.
19. M. Kibria and Z. Mi, *Journal of Materials Chemistry A*, 2016, **4**, 2801-2820.
20. Y.-K. Kuo, B.-T. Liou, S.-H. Yen and H.-Y. Chu, *Optics Communications*, 2004, **237**, 363-369.
21. Y. Wu, X. Liu, A. Pandey, P. Zhou, W. J. Dong, P. Wang, J. Min, P. Deotare, M. Kira and E. Kioupakis, *Progress in Quantum Electronics*, 2022, 100401.
22. M. G. Kibria, R. Qiao, W. Yang, I. Boukahil, X. Kong, F. A. Chowdhury, M. L.

- Trudeau, W. Ji, H. Guo and F. Himpsel, *Advanced Materials*, 2016, **28**, 8388-8397.
23. Z. H. Lan, C. H. Liang, C. W. Hsu, C. T. Wu, H. M. Lin, S. Dhara, K. H. Chen, L. C. Chen and C.-C. Chen, *Advanced Functional Materials*, 2004, **14**, 233-237.
24. J. Hu, Y. Bando, D. Golberg and Q. Liu, *Angewandte Chemie*, 2003, **115**, 3617-3621.
25. M. Kumar, S. Kumar, N. Chauhan, D. S. Kumar, V. Kumar and R. Singh, *Semiconductor Science and Technology*, 2017, **32**, 085012.
26. W.-S. Jung and B.-K. Min, *Materials Letters*, 2004, **58**, 3058-3062.
27. a. R. Wagner and s. W. Ellis, *Applied physics letters*, 1964, **4**, 89-90.
28. X. Duan and C. M. Lieber, *Journal of the American Chemical Society*, 2000, **122**, 188-189.
29. Y. Tang, Z. Chen, H. Song, C. Lee, H. Cong, H. Cheng, W. Zhang, I. Bello and S. Lee, *Nano letters*, 2008, **8**, 4191-4195.
30. T. Kuykendall, P. J. Pauzauskie, Y. Zhang, J. Goldberger, D. Sirbuly, J. Denlinger and P. Yang, *Nature materials*, 2004, **3**, 524-528.
31. C. B. Maliakkal, N. Hatui, R. D. Bapat, B. A. Chalke, A. A. Rahman and A. Bhattacharya, *Nano Letters*, 2016, **16**, 7632-7638.
32. F. Qian, Y. Li, S. Gradečak, H.-G. Park, Y. Dong, Y. Ding, Z. L. Wang and C. M. Lieber, *Nature materials*, 2008, **7**, 701-706.
33. C. Chèze, L. Geelhaar, B. Jenichen and H. Riechert, *Applied Physics Letters*, 2010, **97**, 153105.
34. T. R. Kuykendall, M. V. P. Altoe, D. F. Ogletree and S. Aloni, *Nano letters*, 2014, **14**, 6767-6773.
35. G. Avit, K. Lekhal, Y. André, C. Bougerol, F. Reveret, J. Leymarie, E. Gil, G. Monier, D. Castelluci and A. Trassoudaine, *Nano letters*, 2014, **14**, 559-562.
36. T. Kuykendall, P. Pauzauskie, S. Lee, Y. Zhang, J. Goldberger and P. Yang, *Nano Letters*, 2003, **3**, 1063-1066.
37. B. Kuppulingam, R. Loganathan, K. Prabakaran and K. Baskar, *Optik*, 2016, **127**, 3762-3765.
38. B. Alloing and J. Zúñiga-Pérez, *Materials Science in Semiconductor Processing*, 2016, **55**, 51-58.
39. S. Zhao, H. P. Nguyen, M. G. Kibria and Z. Mi, *Progress in Quantum Electronics*, 2015, **44**, 14-68.

40. C. Tessarek, S. Fladischer, C. Dieker, G. Sarau, B. Hoffmann, M. Bashouti, M. Göbelt, M. Heilmann, M. Latzel and E. Butzen, *Nano Letters*, 2016, **16**, 3415-3425.
41. M. Knelangen, V. Consonni, A. Trampert and H. Riechert, *Nanotechnology*, 2010, **21**, 245705.
42. K. A. Bertness, A. Roshko, L. Mansfield, T. E. Harvey and N. A. Sanford, *Journal of Crystal Growth*, 2008, **310**, 3154-3158.
43. Z. Xu, S. Zhang, F. Gao, L. Wen, Y. Yu and G. Li, *Nanotechnology*, 2018, **29**, 475603.
44. Y.-L. Chang, F. Li, A. Fatehi and Z. Mi, *Nanotechnology*, 2009, **20**, 345203.
45. V. Consonni, M. Hanke, M. Knelangen, L. Geelhaar, A. Trampert and H. Riechert, *Physical Review B*, 2011, **83**, 035310.
46. J. Shen, Y. Yu, J. Wang, Y. Zheng, Y. Gan and G. Li, *Nanoscale*, 2020, **12**, 4018-4029.
47. R. Debnath, R. Meijers, T. Richter, T. Stoica, R. Calarco and H. Lüth, *Applied physics letters*, 2007, **90**, 123117.
48. T. Stoica, E. Sutter, R. J. Meijers, R. K. Debnath, R. Calarco, H. Lüth and D. Grützmacher, *Small*, 2008, **4**, 751-754.
49. V. Kumaresan, L. Largeau, A. Madouri, F. Glas, H. Zhang, F. Oehler, A. Cavanna, A. Babichev, L. Travers and N. Gogneau, *Nano letters*, 2016, **16**, 4895-4902.
50. A. Prabaswara, H. Kim, J.-W. Min, R. C. Subedi, D. H. Anjum, B. Davaasuren, K. Moore, M. Conroy, S. Mitra and I. S. Roqan, *ACS nano*, 2020, **14**, 2202-2211.
51. G. Calabrese, P. Corfdir, G. Gao, C. Pfüller, A. Trampert, O. Brandt, L. Geelhaar and S. Fernández-Garrido, *Applied Physics Letters*, 2016, **108**, 202101.
52. P. R. Narangari, S. K. Karuturi, M. Lysevych, H. H. Tan and C. Jagadish, *Nanotechnology*, 2017, **28**, 154001.
53. X. Xi, J. Li, Z. Ma, X. Li and L. Zhao, *RSC advances*, 2019, **9**, 14937-14943.
54. Y. Sang, B. Liu, T. Tao, D. Jiang, Y. Wu, X. Chen, W. Luo, J. Ye and R. Zhang, *Semiconductor Science and Technology*, 2020, **35**, 025017.
55. J. Butson, P. R. Narangari, S. K. Karuturi, R. Yew, M. Lysevych, H. H. Tan and C. Jagadish, *Nanotechnology*, 2017, **29**, 045403.
56. J. Y. Park, B. J. Kim, C. J. Yoo, W. J. Dong, I. Lee, S. Kim and J.-L. Lee, *Scientific reports*, 2020, **10**, 1-7.
57. J. H. Son, J. U. Kim, Y. H. Song, B. J. Kim, C. J. Ryu and J. L. Lee, *Advanced Materials*, 2012, **24**, 2259-2262.

58. A. Pandey and Z. Mi, *IEEE Journal of Quantum Electronics*, 2022.
59. K. Wang, G. Yuan, R. Wu, H. Lu, Z. Liu, T. Wei, J. Wang, J. Li and W. Zhang, *Journal of Crystal Growth*, 2016, **440**, 96-101.
60. X. Geng, B. K. Duan, D. A. Grismer, L. Zhao and P. W. Bohn, *Electrochemistry communications*, 2012, **19**, 39-42.
61. J. Benton, J. Bai and T. Wang, *Applied Physics Letters*, 2014, **105**, 223902.
62. Y. Hou, Z. Ahmed Syed, L. Jiu, J. Bai and T. Wang, *Applied Physics Letters*, 2017, **111**, 203901.
63. S.-W. Ryu, Y. Zhang, B. Leung, C. Yerino and J. Han, *Semiconductor science and technology*, 2011, **27**, 015014.
64. J. Benton, J. Bai and T. Wang, *Applied Physics Letters*, 2013, **102**, 173905.
65. J. Benton, J. Bai and T. Wang, *Applied Physics Letters*, 2013, **103**, 133904.
66. M. Reddeppa, C. Thota, D.-J. Nam, H. Woo, S.-G. Kim and M.-D. Kim, *Applied Physics Letters*, 2021, **119**, 023901.
67. M. Ebaid, J.-W. Min, C. Zhao, T. K. Ng, H. Idriss and B. S. Ooi, *Journal of Materials Chemistry A*, 2018, **6**, 6922-6930.
68. A. Abdullah, A. Waseem, I. V. Bagal, M. A. Johar, M. A. Kulkarni, J. K. Lee and S.-W. Ryu, *ACS Applied Energy Materials*, 2021, **4**, 13759-13765.
69. H. Bae, H. Rho, J.-W. Min, Y.-T. Lee, S. H. Lee, K. Fujii, H.-J. Lee and J.-S. Ha, *Applied Surface Science*, 2017, **422**, 354-358.
70. M. Ebaid, J.-H. Kang and S.-W. Ryu, *Semiconductor Science and Technology*, 2016, **32**, 013001.
71. M. Ebaid, J.-H. Kang and S.-W. Ryu, *Journal of The Electrochemical Society*, 2015, **162**, H264.
72. S. Han, S. Noh, J. Shin, Y.-T. Yu, C.-R. Lee and J. S. Kim, *Journal of Materials Chemistry C*, 2021, **9**, 12802-12810.
73. A. Abdullah, I. V. Bagal, A. Waseem, M. A. Kulkarni, H. Thaalbi, J. K. Lee and S.-W. Ryu, *Materials Today Physics*, 2022, **28**, 100846.
74. B. AlOtaibi, M. Harati, S. Fan, S. Zhao, H. Nguyen, M. Kibria and Z. Mi, *Nanotechnology*, 2013, **24**, 175401.
75. H. Chen, P. Wang, H. Ye, H. Yin, L. Rao, D. Luo, X. Hou, G. Zhou and R. Nötzel, *Chemical Engineering Journal*, 2021, **406**, 126757.

76. H. Chen, P. Wang, X. Wang, X. Wang, L. Rao, Y. Qian, H. Yin, X. Hou, H. Ye and G. Zhou, *Nano Energy*, 2021, **83**, 105768.
77. N. Alvi, P. Soto Rodriguez, P. Kumar, V. Gómez, P. Aseev, A. Alvi, M. Alvi, M. Willander and R. Nötzel, *Applied Physics Letters*, 2014, **104**, 223104.
78. H. Zhang, M. Ebaid, J.-W. Min, T. K. Ng and B. S. Ooi, *Journal of Applied Physics*, 2018, **124**, 083105.
79. J. Lin, Y. Yu, Z. Xu, F. Gao, Z. Zhang, F. Zeng, W. Wang and G. Li, *Journal of Power Sources*, 2020, **450**, 227578.
80. S. Chu, S. Vanka, Y. Wang, J. Gim, Y. Wang, Y.-H. Ra, R. Hovden, H. Guo, I. Shih and Z. Mi, *ACS Energy Letters*, 2018, **3**, 307-314.
81. L. Caccamo, J. Hartmann, C. Fàbrega, S. Estrade, G. Lilienkamp, J. D. Prades, M. W. Hoffmann, J. Ledig, A. Wagner and X. Wang, *ACS applied materials & interfaces*, 2014, **6**, 2235-2240.
82. B. AlOtaibi, H. Nguyen, S. Zhao, M. Kibria, S. Fan and Z. Mi, *Nano letters*, 2013, **13**, 4356-4361.
83. M. A. Hassan, J.-H. Kang, M. A. Johar, J.-S. Ha and S.-W. Ryu, *Acta Materialia*, 2018, **146**, 171-175.
84. Z. Xu, S. Zhang, F. Gao, P. Gao, Y. Yu, J. Lin, J. Liang and G. Li, *Electrochimica Acta*, 2019, **324**, 134844.
85. S. Han, S. Noh, Y.-T. Yu, C.-R. Lee, S.-K. Lee and J. S. Kim, *ACS Applied Materials & Interfaces*, 2020, **12**, 58028-58037.
86. J. Lin, Y. Yu, Z. Zhang, F. Gao, S. Liu, W. Wang and G. Li, *Advanced Functional Materials*, 2020, **30**, 1910479.
87. S. Fan, I. Shih and Z. Mi, *Advanced Energy Materials*, 2017, **7**, 1600952.
88. D. Ghosh, P. Devi and P. Kumar, *ACS applied materials & interfaces*, 2020, **12**, 13797-13804.
89. B. Zhou, X. Kong, S. Vanka, S. Chu, P. Ghamari, Y. Wang, N. Pant, I. Shih, H. Guo and Z. Mi, *Nature Communications*, 2018, **9**, 3856.
90. S. Fan, B. AlOtaibi, S. Y. Woo, Y. Wang, G. A. Botton and Z. Mi, *Nano letters*, 2015, **15**, 2721-2726.
91. Y. Wang, Y. Wu, J. Schwartz, S. H. Sung, R. Hovden and Z. Mi, *Joule*, 2019, **3**, 2444-2456.

92. Y. Wang, S. Vanka, J. Gim, Y. Wu, R. Fan, Y. Zhang, J. Shi, M. Shen, R. Hovden and Z. Mi, *Nano Energy*, 2019, **57**, 405-413.
93. I. A. Navid, S. Vanka, R. A. Awni, Y. Xiao, Z. Song, Y. Yan and Z. Mi, *Applied Physics Letters*, 2021, **118**, 243906.
94. S. Vanka, B. Zhou, R. A. Awni, Z. Song, F. A. Chowdhury, X. Liu, H. Hajibabaei, W. Shi, Y. Xiao and I. A. Navid, *ACS Energy Letters*, 2020, **5**, 3741-3751.
95. G. Zeng, T. A. Pham, S. Vanka, G. Liu, C. Song, J. K. Cooper, Z. Mi, T. Ogitsu and F. M. Toma, *Nature Materials*, 2021, **20**, 1130-1135.
96. Y. Xiao, S. Vanka, T. A. Pham, W. J. Dong, Y. Sun, X. Liu, I. A. Navid, J. B. Varley, H. Hajibabaei and T. W. Hamann, *Nano Letters*, 2022, **22**, 2236-2243.
97. S. Vanka, E. Arca, S. Cheng, K. Sun, G. A. Botton, G. Teeter and Z. Mi, *Nano letters*, 2018, **18**, 6530-6537.
98. Y. Wang, J. Schwartz, J. Gim, R. Hovden and Z. Mi, *ACS Energy Letters*, 2019, **4**, 1541-1548.
99. W. J. Dong, Y. Xiao, K. R. Yang, Z. Ye, P. Zhou, I. A. Navid, V. S. Batista and Z. Mi, *Nature Communications*, 2023, **14**, 1-10.
100. H. Zhang, M. Ebaid, J. Tan, G. Liu, J.-W. Min, T. K. Ng and B. S. Ooi, *Optics Express*, 2019, **27**, A81-A91.
101. K. Aryal, B. Pantha, J. Li, J. Lin and H. Jiang, *Applied Physics Letters*, 2010, **96**, 052110.
102. J. Lin, W. Wang and G. Li, *Advanced Functional Materials*, 2020, **30**, 2005677.
103. M. Ebaid, J.-H. Kang, S.-H. Lim, J.-S. Ha, J. K. Lee, Y.-H. Cho and S.-W. Ryu, *Nano Energy*, 2015, **12**, 215-223.
104. Y. J. Hwang, C. H. Wu, C. Hahn, H. E. Jeong and P. Yang, *Nano letters*, 2012, **12**, 1678-1682.
105. M. Ebaid, J.-H. Kang, S.-H. Lim, Y.-H. Cho and S.-W. Ryu, *RSC Advances*, 2015, **5**, 23303-23310.
106. J.-H. Park, A. Mandal, S. Kang, U. Chatterjee, J. S. Kim, B.-G. Park, M.-D. Kim, K.-U. Jeong and C.-R. Lee, *Scientific Reports*, 2016, **6**, 1-10.
107. E. Verlage, S. Hu, R. Liu, R. J. Jones, K. Sun, C. Xiang, N. S. Lewis and H. A. Atwater, *Energy & Environmental Science*, 2015, **8**, 3166-3172.
108. P. Varadhan, H.-C. Fu, Y.-C. Kao, R.-H. Horng and J.-H. He, *Nature communications*,

- 2019, **10**, 1-9.
109. M. M. May, H.-J. Lewerenz, D. Lackner, F. Dimroth and T. Hannappel, *Nature Communications*, 2015, **6**, 1-7.
110. J. L. Young, M. A. Steiner, H. Döscher, R. M. France, J. A. Turner and T. G. Deutsch, *Nature Energy*, 2017, **2**, 1-8.
111. B. AlOtaibi, S. Fan, S. Vanka, M. Kibria and Z. Mi, *Nano letters*, 2015, **15**, 6821-6828.
112. C. W. Kim, S. J. Yeob, H.-M. Cheng and Y. S. Kang, *Energy & Environmental Science*, 2015, **8**, 3646-3653.
113. L. Wang, N. T. Nguyen, Z. Shen, P. Schmuki and Y. Bi, *Nano Energy*, 2018, **50**, 331-338.
114. Z. Zhang, I. Karimata, H. Nagashima, S. Muto, K. Ohara, K. Sugimoto and T. Tachikawa, *Nature communications*, 2019, **10**, 1-12.
115. J. Zhang, P. Zhang, T. Wang and J. Gong, *Nano Energy*, 2015, **11**, 189-195.
116. S. Wang, H. Chen, G. Gao, T. Butburee, M. Lyu, S. Thaweesak, J.-H. Yun, A. Du, G. Liu and L. Wang, *Nano Energy*, 2016, **24**, 94-102.
117. J. Liu, S.-M. Xu, Y. Li, R. Zhang and M. Shao, *Applied Catalysis B: Environmental*, 2020, **264**, 118540.
118. H. S. Han, S. Shin, D. H. Kim, I. J. Park, J. S. Kim, P.-S. Huang, J.-K. Lee, I. S. Cho and X. Zheng, *Energy & Environmental Science*, 2018, **11**, 1299-1306.
119. C. W. Kim, Y. S. Son, M. J. Kang, D. Y. Kim and Y. S. Kang, *Advanced Energy Materials*, 2016, **6**, 1501754.
120. C. Li, Y. Li and J.-J. Delaunay, *ACS applied materials & interfaces*, 2014, **6**, 480-486.
121. S. K. Baek, J. S. Kim, Y. D. Yun, Y. B. Kim and H. K. Cho, *ACS Sustainable Chemistry & Engineering*, 2018, **6**, 10364-10373.
122. H. Lee, W. Yang, J. Tan, Y. Oh, J. Park and J. Moon, *ACS Energy Letters*, 2019, **4**, 995-1003.
123. W. Yang, J. Ahn, Y. Oh, J. Tan, H. Lee, J. Park, H. C. Kwon, J. Kim, W. Jo and J. Kim, *Advanced Energy Materials*, 2018, **8**, 1702888.
124. Z. Shi, J. Feng, H. Shan, X. Wang, Z. Xu, H. Huang, Q. Qian, S. Yan and Z. Zou, *Applied Catalysis B: Environmental*, 2018, **237**, 665-672.
125. Y. Hou, T. Li, S. Yan and Z. Zou, *Applied Catalysis B: Environmental*, 2020, **269**, 118777.

126. J. Luo, L. Steier, M.-K. Son, M. Schreier, M. T. Mayer and M. Grätzel, *Nano letters*, 2016, **16**, 1848-1857.
127. S. Choi, J. Hwang, T. H. Lee, H.-H. Kim, S.-P. Hong, C. Kim, M.-J. Choi, H. K. Park, S. S. Bhat and J. M. Suh, *Chemical Engineering Journal*, 2020, **392**, 123688.
128. G. Wang, H. Wang, Y. Ling, Y. Tang, X. Yang, R. C. Fitzmorris, C. Wang, J. Z. Zhang and Y. Li, *Nano letters*, 2011, **11**, 3026-3033.
129. W.-H. Cheng, M. H. Richter, M. M. May, J. Ohlmann, D. Lackner, F. Dimroth, T. Hannappel, H. A. Atwater and H.-J. Lewerenz, *ACS Energy Letters*, 2018, **3**, 1795-1800.
130. W. J. Dong, Y. J. Song, H. Yoon, G. H. Jung, K. Kim, S. Kim and J. L. Lee, *Advanced Energy Materials*, 2017, **7**, 1700659.
131. S. Chen and L.-W. Wang, *Chemistry of Materials*, 2012, **24**, 3659-3666.
132. D. Bae, B. Seger, P. C. Vesborg, O. Hansen and I. Chorkendorff, *Chemical Society Reviews*, 2017, **46**, 1933-1954.
133. S. Hu, M. R. Shaner, J. A. Beardslee, M. Lichterman, B. S. Brunschwig and N. S. Lewis, *Science*, 2014, **344**, 1005-1009.
134. R. Fan, W. Dong, L. Fang, F. Zheng, X. Su, S. Zou, J. Huang, X. Wang and M. Shen, *Applied Physics Letters*, 2015, **106**, 013902.
135. S. Vanka, K. Sun, G. Zeng, T. A. Pham, F. M. Toma, T. Ogitsu and Z. Mi, *Journal of Materials Chemistry A*, 2019, **7**, 27612-27619.
136. P. Varadhan, H.-C. Fu, D. Priante, J. R. D. Retamal, C. Zhao, M. Ebaid, T. K. Ng, I. Ajia, S. Mitra and I. S. Roqan, *Nano letters*, 2017, **17**, 1520-1528.
137. T. Takata, J. Jiang, Y. Sakata, M. Nakabayashi, N. Shibata, V. Nandal, K. Seki, T. Hisatomi and K. Domen, *Nature*, 2020, **581**, 411-414.
138. M. Ni, M. K. Leung, D. Y. Leung and K. Sumathy, *Renewable and Sustainable Energy Reviews*, 2007, **11**, 401-425.
139. X. Guan, F. A. Chowdhury, N. Pant, L. Guo, L. Vayssieres and Z. Mi, *The Journal of Physical Chemistry C*, 2018, **122**, 13797-13802.
140. X. Guan, F. A. Chowdhury, Y. Wang, N. Pant, S. Vanka, M. L. Trudeau, L. Guo, L. Vayssieres and Z. Mi, *ACS Energy Letters*, 2018, **3**, 2230-2231.
141. Q. Luo, R. Yuan, Y.-L. Hu and D. Wang, *Applied Surface Science*, 2021, **537**, 147930.
142. M. G. Kibria, H. P. Nguyen, K. Cui, S. Zhao, D. Liu, H. Guo, M. L. Trudeau, S. Paradis,

- A.-R. Hakima and Z. Mi, *ACS nano*, 2013, **7**, 7886-7893.
143. Y. Wang, Y. Wu, K. Sun and Z. Mi, *Materials Horizons*, 2019, **6**, 1454-1462.
144. M. Kibria, F. Chowdhury, S. Zhao, M. Trudeau, H. Guo and Z. Mi, *Applied Physics Letters*, 2015, **106**, 113105.
145. M. Kibria, S. Zhao, F. Chowdhury, Q. Wang, H. Nguyen, M. Trudeau, H. Guo and Z. Mi, *Nature communications*, 2014, **5**, 1-6.
146. M. Kibria, F. Chowdhury, S. Zhao, B. AlOtaibi, M. Trudeau, H. Guo and Z. Mi, *Nature communications*, 2015, **6**, 1-8.
147. F. A. Chowdhury, M. L. Trudeau, H. Guo and Z. Mi, *Nature communications*, 2018, **9**, 1-9.
148. Z. Li, L. Zhang, Y. Liu, C. Shao, Y. Gao, F. Fan, J. Wang, J. Li, J. Yan and R. Li, *Angewandte Chemie International Edition*, 2020, **59**, 935-942.
149. P. Zhou, I. A. Navid, Y. Ma, Y. Xiao, P. Wang, Z. Ye, B. Zhou, K. Sun and Z. Mi, *Nature*, 2023, **613**, 66-70.
150. D. Wang, A. Pierre, M. G. Kibria, K. Cui, X. Han, K. H. Bevan, H. Guo, S. Paradis, A.-R. Hakima and Z. Mi, *Nano letters*, 2011, **11**, 2353-2357.
151. S. Barbet, R. Aubry, M.-A. di Forte-Poisson, J.-C. Jacquet, D. Deresmes, T. Melin and D. Théron, *Applied Physics Letters*, 2008, **93**, 212107.
152. H. Sezen, E. Ozbay, O. Aktas and S. Suzer, *Applied Physics Letters*, 2011, **98**, 111901.
153. M. Seelmann-Eggebert, J. Weyher, H. Obloh, H. Zimmermann, A. Rar and S. Porowski, *Applied Physics Letters*, 1997, **71**, 2635-2637.
154. G. Liu, F. Zheng, J. Li, G. Zeng, Y. Ye, D. M. Larson, J. Yano, E. J. Crumlin, J. W. Ager and L.-w. Wang, *Nature Energy*, 2021, **6**, 1124-1132.
155. B. Tang and F.-X. Xiao, *ACS Catalysis*, 2022, **12**, 9023-9057.
156. D. Li, K. Yang, J. Lian, J. Yan and S. Liu, *Advanced Energy Materials*, 2022, **12**, 2201070.
157. L. K. Putri, B. J. Ng, W. J. Ong, S. P. Chai and A. R. Mohamed, *Advanced Energy Materials*, 2022, **12**, 2201093.
158. X. Chang, T. Wang, P. Yang, G. Zhang and J. Gong, *Advanced Materials*, 2019, **31**, 1804710.
159. P. Ding, T. Jiang, N. Han and Y. Li, *Materials Today Nano*, 2020, **10**, 100077.
160. J. T. Song, H. Ryoo, M. Cho, J. Kim, J. G. Kim, S. Y. Chung and J. Oh, *Advanced*

- Energy Materials*, 2017, **7**, 1601103.
161. C. Li, T. Wang, B. Liu, M. Chen, A. Li, G. Zhang, M. Du, H. Wang, S. F. Liu and J. Gong, *Energy & Environmental Science*, 2019, **12**, 923-928.
162. N. Sagara, S. Kamimura, T. Tsubota and T. Ohno, *Applied Catalysis B: Environmental*, 2016, **192**, 193-198.
163. S. Zhou, K. Sun, J. Huang, X. Lu, B. Xie, D. Zhang, J. N. Hart, C. Y. Toe, X. Hao and R. Amal, *Small*, 2021, **17**, 2100496.
164. W. J. Dong, J. W. Lim, D. M. Hong, J. Kim, J. Y. Park, W. S. Cho, S. Baek and J.-L. Lee, *ACS Applied Materials & Interfaces*, 2021, **13**, 18905-18913.
165. G. Zeng, J. Qiu, B. Hou, H. Shi, Y. Lin, M. Hettick, A. Javey and S. B. Cronin, *Chemistry—A European Journal*, 2015, **21**, 13502-13507.
166. M. Kan, C. Yang, Q. Wang, Q. Zhang, Y. Yan, K. Liu, A. Guan and G. Zheng, *Advanced Energy Materials*, 2022, 2201134.
167. S. Roy, M. Miller, J. Warnan, J. J. Leung, C. D. Sahm and E. Reisner, *ACS Catalysis*, 2021, **11**, 1868-1876.
168. P. A. Kempler, M. H. Richter, W.-H. Cheng, B. S. Brunschwig and N. S. Lewis, *ACS Energy Letters*, 2020, **5**, 2528-2534.
169. G. Liu, P. R. Narangari, Q. T. Trinh, W. Tu, M. Kraft, H. H. Tan, C. Jagadish, T. S. Choksi, J. W. Ager and S. Karuturi, *ACS Catalysis*, 2021, **11**, 11416-11428.
170. J. Qiu, G. Zeng, M.-A. Ha, M. Ge, Y. Lin, M. Hettick, B. Hou, A. N. Alexandrova, A. Javey and S. B. Cronin, *Nano letters*, 2015, **15**, 6177-6181.
171. Y. Zhang, D. Pan, Y. Tao, H. Shang, D. Zhang, G. Li and H. Li, *Advanced Functional Materials*, 2022, **32**, 2109600.
172. K. Lee, S. Lee, H. Cho, S. Jeong, W. D. Kim, S. Lee and D. C. Lee, *Journal of energy chemistry*, 2018, **27**, 264-270.
173. H.-Y. Kang, D.-H. Nam, K. D. Yang, W. Joo, H. Kwak, H.-H. Kim, S.-H. Hong, K. T. Nam and Y.-C. Joo, *ACS nano*, 2018, **12**, 8187-8196.
174. X. Deng, R. Li, S. Wu, L. Wang, J. Hu, J. Ma, W. Jiang, N. Zhang, X. Zheng and C. Gao, *Journal of the American Chemical Society*, 2019, **141**, 10924-10929.
175. Y. J. Jang, J.-W. Jang, J. Lee, J. H. Kim, H. Kumagai, J. Lee, T. Minegishi, J. Kubota, K. Domen and J. S. Lee, *Energy & Environmental Science*, 2015, **8**, 3597-3604.
176. J. S. DuChene, G. Tagliabue, A. J. Welch, W.-H. Cheng and H. A. Atwater, *Nano*

- letters, 2018, **18**, 2545-2550.
177. S. Chu, S. Fan, Y. Wang, D. Rossouw, Y. Wang, G. A. Botton and Z. Mi, *Angewandte Chemie International Edition*, 2016, **55**, 14262-14266.
178. S. Chu, P. Ou, P. Ghamari, S. Vanka, B. Zhou, I. Shih, J. Song and Z. Mi, *Journal of the American Chemical Society*, 2018, **140**, 7869-7877.
179. S. Chu, P. Ou, R. T. Rashid, P. Ghamari, R. Wang, H. N. Tran, S. Zhao, H. Zhang, J. Song and Z. Mi, *iscience*, 2020, **23**, 101390.
180. S. Chu, P. Ou, R. T. Rashid, Y. Pan, D. Liang, H. Zhang, J. Song and Z. Mi, *Green Energy & Environment*, 2022, **7**, 545-553.
181. W. J. Dong, P. Zhou, Y. Xiao, I. A. Navid, J.-L. Lee and Z. Mi, *ACS Catalysis*, 2022, **12**, 2671-2680.
182. B. Zhou, X. Kong, S. Vanka, S. Cheng, N. Pant, S. Chu, P. Ghamari, Y. Wang, G. Botton and H. Cuo, *Energy & Environmental Science*, 2019, **12**, 2842-2848.
183. W. J. Dong, I. A. Navid, Y. Xiao, T. H. Lee, J. W. Lim, D. Lee, H. W. Jang, J.-L. Lee and Z. Mi, *Journal of Materials Chemistry A*, 2022, **10**, 7869-7877.
184. Y. Wang, S. Fan, B. AlOtaibi, Y. Wang, L. Li and Z. Mi, *Chemistry—A European Journal*, 2016, **22**, 8809-8813.
185. B. Zhou, P. Ou, N. Pant, S. Cheng, S. Vanka, S. Chu, R. T. Rashid, G. Botton, J. Song and Z. Mi, *Proceedings of the National Academy of Sciences*, 2020, **117**, 1330-1338.
186. W. J. Dong, I. A. Navid, Y. Xiao, J. W. Lim, J.-L. Lee and Z. Mi, *Journal of the American Chemical Society*, 2021, **143**, 10099-10107.
187. S. Chu, R. T. Rashid, Y. Pan, X. Wang, H. Zhang and R. Xiao, *Journal of CO2 Utilization*, 2022, **60**, 101993.
188. M. E. Dry, *Catalysis today*, 2002, **71**, 227-241.
189. H. Schulz, *Applied Catalysis A: General*, 1999, **186**, 3-12.
190. M. Azuma, K. Hashimoto, M. Hiramoto, M. Watanabe and T. Sakata, *Journal of the Electrochemical Society*, 1990, **137**, 1772.
191. M. Jitaru, D. Lowy, M. Toma, B. Toma and L. Oniciu, *Journal of Applied Electrochemistry*, 1997, **27**, 875-889.
192. H. Li and C. Oloman, *Journal of Applied Electrochemistry*, 2006, **36**, 1105-1115.
193. Y. Hori, H. Wakebe, T. Tsukamoto and O. Koga, *Electrochimica Acta*, 1994, **39**, 1833-1839.

194. R. Kortlever, I. Peters, S. Koper and M. T. Koper, *Acs Catalysis*, 2015, **5**, 3916-3923.
195. W. J. Dong, C. J. Yoo and J.-L. Lee, *ACS applied materials & interfaces*, 2017, **9**, 43575-43582.
196. C. J. Yoo, W. J. Dong, J. Y. Park, J. W. Lim, S. Kim, K. S. Choi, F. O. Odongo Ngome, S.-Y. Choi and J.-L. Lee, *ACS Applied Energy Materials*, 2020, **3**, 4466-4473.
197. W. J. Dong, J. W. Lim, D. M. Hong, J. Y. Park, W. S. Cho, S. Baek, C. J. Yoo, W. Kim and J.-L. Lee, *ACS Applied Energy Materials*, 2020, **3**, 10568-10577.
198. W. J. Dong, D. M. Hong, J. Y. Park, S. Kim, C. J. Yoo and J.-L. Lee, *Journal of The Electrochemical Society*, 2021, **168**, 016514.
199. J. Kim, J. Y. Park, W. S. Cho, W. J. Dong, J. W. Lim, K. Kim, P. Fernández and J.-L. Lee, *ACS Applied Energy Materials*, 2022, **5**, 11042-11051.
200. W. J. Dong, J. W. Lim, J. Y. Park, C. J. Yoo, S. Baek, W. S. Cho, W. Kim and J.-L. Lee, *Applied Surface Science*, 2021, **565**, 150460.
201. W. S. Cho, D. M. Hong, W. J. Dong, T. H. Lee, C. J. Yoo, D. Lee, H. W. Jang and J. L. Lee, *Energy & Environmental Materials*, e12490.
202. C. Xiao and J. Zhang, *ACS nano*, 2021, **15**, 7975-8000.
203. A. Loiudice, P. Lobaccaro, E. A. Kamali, T. Thao, B. H. Huang, J. W. Ager and R. Buonsanti, *Angewandte Chemie International Edition*, 2016, **55**, 5789-5792.
204. W. J. Dong, C. J. Yoo, J. W. Lim, J. Y. Park, K. Kim, S. Kim, D. Lee and J.-L. Lee, *Nano Energy*, 2020, **78**, 105168.
205. J. W. Lim, W. J. Dong, W. S. Cho, C. J. Yoo and J.-L. Lee, *ACS Catalysis*, 2022, **12**, 13174-13185.
206. J. W. Lim, W. J. Dong, J. Y. Park, D. M. Hong and J.-L. Lee, *ACS applied materials & interfaces*, 2020, **12**, 22891-22900.
207. P. Hou, W. Song, X. Wang, Z. Hu and P. Kang, *Small*, 2020, **16**, 2001896.
208. B. AlOtaibi, S. Fan, D. Wang, J. Ye and Z. Mi, *ACS Catalysis*, 2015, **5**, 5342-5348.
209. B. AlOtaibi, X. Kong, S. Vanka, S. Woo, A. Pofelski, F. Oudjedi, S. Fan, M. Kibria, G. Botton and W. Ji, *ACS Energy Letters*, 2016, **1**, 246-252.
210. R. T. Rashid, Y. Chen, X. Liu, F. A. Chowdhury, M. Liu, J. Song, Z. Mi and B. Zhou, *Proceedings of the National Academy of Sciences*, 2022, **119**, e2121174119.
211. W. H. Lai, Z. Miao, Y. X. Wang, J. Z. Wang and S. L. Chou, *Advanced Energy Materials*, 2019, **9**, 1900722.

212. M. Liu, Y. Wang, X. Kong, L. Tan, L. Li, S. Cheng, G. Botton, H. Guo, Z. Mi and C.-J. Li, *Isience*, 2019, **17**, 208-216.
213. P. Zhou, I. A. Navid, Y. Xiao, Z. Ye, W. J. Dong, P. Wang, K. Sun and Z. Mi, *The Journal of Physical Chemistry Letters*, 2022, **13**, 8122-8129.
214. L. Li, S. Fan, X. Mu, Z. Mi and C.-J. Li, *Journal of the American Chemical Society*, 2014, **136**, 7793-7796.